

**THE MECHANICS OF THE GASTROCNEMII-  
ACHILLES TENDON COMPLEX DURING HUMAN  
CYCLING: EXPERIMENTAL AND MODELLING  
APPROACHES TO PREDICT *IN VIVO* FORCES**

**by**

**Taylor J.M. Dick**

B.Sc. (Hons), Simon Fraser University, 2012

Thesis Submitted in Partial Fulfillment of the  
Requirements for the Degree of  
Doctor of Philosophy

in the

Department of Biomedical Physiology and Kinesiology  
Faculty of Science

**© Taylor J.M. Dick 2016**

**SIMON FRASER UNIVERSITY**

**Fall 2016**

All rights reserved.

However, in accordance with the *Copyright Act of Canada*, this work may be reproduced, without authorization, under the conditions for "Fair Dealing." Therefore, limited reproduction of this work for the purposes of private study, research, criticism, review and news reporting is likely to be in accordance with the law, particularly if cited appropriately.

# Approval

**Name:** Taylor Dick  
**Degree:** Doctor of Philosophy (Biomedical Physiology & Kinesiology)  
**Title:** *Mechanics of the Gastrocnemii-Achilles Tendon Complex During Human Cycling: Experimental and Modelling Approaches to Estimate in vivo Forces*

**Examining Committee:** Chair: Will Cupples, Professor

**James Wakeling**  
Senior Supervisor  
Professor

---

**Dawn Mackey**  
Supervisor  
Assistant Professor

---

**Allison Arnold**  
Supervisor  
Research Associate  
Harvard University

---

**Max Donelan**  
Internal Examiner  
Professor  
Department of Biomedical  
Physiology and Kinesiology

---

**Marc Klimstra**  
External Examiner  
Assistant Professor  
School of Exercise Science, Physical  
and Health Education  
University of Victoria

---

**Date Defended/Approved:** August 30, 2016

## Ethics Statement



The author, whose name appears on the title page of this work, has obtained, for the research described in this work, either:

- a. human research ethics approval from the Simon Fraser University Office of Research Ethics

or

- b. advance approval of the animal care protocol from the University Animal Care Committee of Simon Fraser University

or has conducted the research

- c. as a co-investigator, collaborator, or research assistant in a research project approved in advance.

A copy of the approval letter has been filed with the Theses Office of the University Library at the time of submission of this thesis or project.

The original application for approval and letter of approval are filed with the relevant offices. Inquiries may be directed to those authorities.

Simon Fraser University Library  
Burnaby, British Columbia, Canada

Update Spring 2016

## Abstract

Skeletal muscle is the engine that produces force to power movement in humans and animals alike. To date the invasive nature of obtaining muscle-tendon forces in humans has limited our understanding of muscle function during coordinated locomotor tasks. Phenomenological, Hill-type models of skeletal muscle are often used, providing estimates of a muscle's force as a function of its activation state, force-length, and force-velocity properties. However, few studies have examined the accuracy of whole muscle-tendon forces obtained from such models during *in vivo* motor tasks. The goal of my thesis was to develop, test, and refine methods to better quantify muscle mechanical output in humans, using ultrasound and electromyographic recordings, together with advanced Hill-type models. My first study developed techniques to non-invasively estimate *in vivo* Achilles tendon forces. I used ultrasound-based measures of tendon length and tendon mechanical properties to determine forces during cycling. In my second study, I compared gastrocnemii forces, predicted from a traditional Hill-type model with one contractile element, to force estimates derived from ultrasound-based tendon length changes. Because the traditional Hill-type model fails to account for variable activation states of different fibre types, I additionally tested a two-element model that includes both slow and fast contractile elements. I found that Hill-type models predicted 31-85% of the cyclists' gastrocnemii forces across a range of conditions elicited, producing results comparable to those reported in animal models. Further, at higher cadences, the two-element model better estimated forces because it accounted for the increased recruitment of fast fibres. Traditional Hill-type models also neglect dynamic shape changes in contracting muscles, which may be important in modulating the velocities at which fascicles operate. My third study compared predictions of muscle architecture (fascicle lengths and pennation angles) generated from a 1D Hill-type model and additionally from 2D and 3D geometric models that allowed dynamic shape changes to occur. I found that the 1D model provided predictions of muscle architecture that were similar to the predictions of 2D and 3D models and that muscle shape changes and fascicle velocities were more closely linked to force than activation. Taken together, this research provides a non-invasive approach for studying *in vivo* muscle-tendon mechanics and testing the predictions of Hill-type models.

**Keywords:** B-mode ultrasound, electromyography, Hill-type models, muscle force, tendon stiffness, musculoskeletal simulations

## Acknowledgements

I must first thank my supervisor James, for his guidance, encouragement, and patience over these years. You have ignited a passion for science in me, and for that I will forever be grateful. I feel fortunate to have had a supervisor that allowed and encouraged me to pursue a variety of scientific opportunities across the world, and who strives to make sure his students are successful not only in their academic endeavours, but also in their endeavours outside the lab. It has been a pleasure working under such an inspirational researcher and I especially thank you for the numerous paddling adventures.

I thank my committee members for their thoughtful comments and encouraging words. Allison, thank you for sharing your knowledge, and for your unwavering support and patience; I am grateful to have had such a brilliant and knowledgeable advisor. Dawn, thank you for your guidance and advice along the way. I must also thank Andrew Biewener for welcoming me into his lab on numerous occasions and sharing his wealth of biomechanics wisdom with me. I am thankful for this experience.

Thank you to my current and former lab mates and colleagues who have shared their knowledge, helped with my data collection, and made the lab such a positive and fun environment. In particular, I must thank Dr. Emma Hodson-Tole, Dr. Sabrina Lee, Dr. Oliver Blake, Dr. Adrian Lai, Dr. Courtney Pollock, Dr. Hadi Rahemi, Avleen Randhawa, David Ryan, Sidney Morrison, Kate Olszewski, Carolyn Eng, and Talia Moore.

Most importantly I would like to thank my parents (Brian and Maria) and my siblings (Matthew and Miranda) for their continuous support and patience over the last few years. As well, to my friends, I thank you for listening to my 'practice talks' and always offering some encouraging and positive words. To Christofer, I thank you for your support, your contagious excitement for science, and for being the most wonderful adventure partner I could have ever imagined.

It has been one incredible journey.

# Table of Contents

Approval.....	ii
Ethics Statement.....	iii
Abstract.....	iv
Acknowledgements.....	v
Table of Contents.....	vi
List of Tables.....	viii
List of Figures.....	viii
List of Symbols.....	x
<b>Chapter 1. Introduction .....</b>	<b>1</b>
1.1. Functional design and structural properties of the muscle-tendon unit.....	2
1.2. Physiological properties of skeletal muscle.....	5
1.3. <i>In vivo</i> measures of muscle-tendon behaviour.....	10
1.4. Models of skeletal muscle.....	14
1.5. Outline and specific aims of this thesis .....	18
<b>Chapter 2. Quantifying Achilles tendon force <i>in vivo</i> from ultrasound images.....</b>	<b>24</b>
2.1. Introduction.....	24
2.2. Methods .....	25
2.2.1. Acquisition of experimental data .....	30
2.2.2. Determination of muscle moment arms, muscle-tendon lengths and net ankle moments .....	37
2.2.3. Characterization of subject-specific Achilles tendon force-length properties .....	39
2.2.4. Estimation of Achilles tendon lengths and forces during cycling .....	42
2.2.5. Evaluation of the ultrasound-based method.....	43
2.3. Results .....	46
2.4. Discussion .....	53
<b>Chapter 3. Comparison of gastrocnemius forces predicted by Hill-type muscle models and estimated from ultrasound images during human cycling .....</b>	<b>60</b>
3.1. Introduction.....	60
3.2. Methods .....	62
3.2.1. Muscle models for estimating LG and MG forces.....	63
3.2.2. Acquisition of experimental data .....	68
3.2.3. Analysis of experimental data for driving models: muscle fascicle lengths and pennation angles.....	68
3.2.4. Analysis of experimental data for driving models: muscle activation patterns .....	69
3.2.5. Analysis of experimental data for evaluating models: <i>in vivo</i> forces.....	73
3.2.6. Comparison of predicted and estimated forces .....	74

3.3. Results .....	74
3.4. Discussion .....	83
3.4.1. Comparison to Hill-type models in the literature.....	83
3.4.2. Differences between muscles and pedalling conditions .....	85
3.4.3. Comparison of one- and two-element models.....	86
3.4.4. Sensitivity of models to assumed intrinsic properties .....	88
3.4.5. Limitations .....	88
3.5. Conclusions.....	90
<b>Chapter 4. Shifting gears: muscle shape changes and force-velocity behaviour in the human gastrocnemius during cycling .....</b>	<b>91</b>
4.1. Introduction.....	91
4.2. Methods .....	95
4.2.1. Acquisition of experimental data .....	95
4.2.2. Analysis of experimental data .....	96
4.2.3. Multidimensional muscle models .....	98
4.2.4. Model comparisons .....	102
4.2.5. Statistics .....	103
4.3. Results .....	104
4.4. Discussion .....	116
4.4.1. Dynamic muscle shape changes .....	117
4.4.2. Gearing .....	119
4.4.3. Activation and force effects.....	120
4.4.4. Multidimensional Hill-type models.....	121
4.4.5. Limitations .....	124
4.5. Conclusions.....	125
<b>Chapter 5. Discussion .....</b>	<b>126</b>
5.1. Summary of thesis.....	126
5.2. Using <i>in vivo</i> experimental data to inform muscle models.....	129
5.3. Application to clinical research.....	132
5.4. Modelling human muscle force: where are we now, where are we going? .....	133
<b>References .....</b>	<b>136</b>

## List of Tables

Table 2-1.	Characteristics of the ten competitive female cyclists tested. ....	27
Table 2-2.	Characteristics of the ten competitive male cyclists tested. ....	29
Table 2-3.	Comparison of gastrocnemii moment arms in this chapter to Achilles tendon moment arms published in the literature. ....	38
Table 3-1.	Subject characteristics. ....	66
Table 3-2.	Centre frequencies and scale factors of optimized wavelets. ....	71
Table 3-3.	Constants for the excitation-activation transfer functions. ....	72
Table 3-4.	Average LG and MG coefficient of determination $r^2$ and RMSE between model predictions and ultrasound-based estimates of force, using the one-element and the two-element models across pedalling conditions. ....	80
Table 3-5.	Chi-square test results for comparison of $r^2$ and RMSE between one-element and two-element Hill-type muscle models. ....	81
Table 4-1.	Physiological representation of fascicle shape factor $n$ . ....	103

## List of Figures

Figure 1-1.	Hierarchical structure of skeletal muscle. ....	3
Figure 1-2.	Anatomy of the human triceps surae-Achilles tendon complex. ....	5
Figure 1-3.	Force-length and force-velocity relationships of skeletal muscle. ....	6
Figure 1-4.	Representation of a Hill-type muscle model. ....	15
Figure 1-5.	Overview of thesis. ....	19
Figure 2-1.	Approach for estimating and evaluating <i>in vivo</i> Achilles tendon forces during cycling from tracked ultrasound images. ....	32
Figure 2-2.	Experimental data from a representative subject pedalling at low load and high load conditions. ....	34
Figure 2-3.	Procedure for measuring Achilles tendon stiffness in individual subjects. ....	36
Figure 2-4.	Plantarflexion moment arms during cycling. ....	39
Figure 2-5.	Comparison of maximum isometric plantarflexion moments generated by all plantarflexors versus the triceps surae muscles. ....	41
Figure 2-6.	Achilles tendon (AT) force-length curve derived from inverse dynamics estimated AT forces and ultrasound measured AT length changes for one subject. ....	45

Figure 2-7.	Achilles tendon strains during cycling at 80 r.p.m. ....	47
Figure 2-8.	Kinematics and associated muscle-tendon unit strains during cycling at 80 r.p.m. ....	48
Figure 2-9.	Increase in AT force with crank load.....	49
Figure 2-10.	Electromyographic signals during cycling at 80 r.p.m. ....	50
Figure 2-11.	Comparison of time-varying <i>in vivo</i> Achilles tendon moment and inverse dynamics net ankle moment. ....	51
Figure 2-12.	Comparison of ultrasound-based moments to inverse dynamics moments across cycling loads.....	51
Figure 2-13.	Effects of two methodological refinements on estimated Achilles tendon ankle moments. ....	52
Figure 2-14.	Sensitivity analysis of Achilles tendon forces.....	55
Figure 2-15.	Increase in net ankle moment with crank load at 80 r.p.m. ....	59
Figure 3-1.	Schematic of muscle models tested. ....	64
Figure 3-2.	Representative inputs and outputs from muscle models.....	65
Figure 3-3.	B-mode ultrasound images of the lateral and medial gastrocnemii muscle bellies. ....	69
Figure 3-4.	Optimized wavelets for lateral and medial gastrocnemii. ....	71
Figure 3-5.	Force profiles for the LG and MG during four different pedalling conditions for one representative subject. ....	76
Figure 3-6.	Comparison of the one- and two-element Hill-type models predicted forces to ultrasound-based estimates of force.....	77
Figure 3-7.	Differential recruitment of slow and fast muscle fibres with pedalling condition. ....	78
Figure 3-8.	Results of sensitivity analysis to force-velocity parameters. ....	82
Figure 4-1.	Approach for testing 1D, 2D, and 3D muscle models using experimental data collected during human cycling. ....	96
Figure 4-2.	Representation of 1D, 2D, and 3D muscle models. ....	99
Figure 4-3.	Experimental pedalling data. ....	106
Figure 4-4.	Changes in muscle belly and fascicle behaviour with varying pedalling conditions.....	107
Figure 4-5.	Changes in muscle activation (A), muscle belly gearing (B), tendon strain (C), and tendon force (D) at each pedalling condition.....	109
Figure 4-6.	Correlation between muscle activation and tendon force during pedalling.....	110
Figure 4-7.	Comparison of experimentally measured and model predicted time-varying pennation angles and fascicle lengths.....	112

Figure 4-8.	$r^2$ and RMSE comparing the measured and predicted pennation angle, fascicle length, and muscle gearing. ....	113
Figure 4-9.	Contour plots comparing the measured and predicted pennation angle, fascicle length, and muscle gearing. ....	116

## List of Symbols

Symbol	Definition
$a$	Hill's equation empirical constant 1
$\hat{A}_{\text{PCSA}}$	Fractional physiological cross-sectional area
$a(t)$	Activation
$\hat{a}(t)$	Normalized activation
$\hat{a}_{\text{fast}}(t)$	Normalized activation, fast motor units
$\hat{a}_{\text{slow}}(t)$	Normalized activation, slow motor units
AT	Achilles tendon
$b$	Hill's equation empirical constant 2
$C_{\text{apo}}$	Aponeurosis compliance
$c_e$	Tendon force scaling factor
$c_1$	Scale factor, represents the lower EMG excitations that would be expected from action potentials with higher spectral frequencies
$d_{\text{COP}}$	Distance between fulcrum and the foot's centre of pressure
$d_f$	Distance between the foot's centre of pressure and the ankle axis
$d_G$	Distance between the strain gauge and the fulcrum of the foot plate
$e(t)$	Excitation
$\hat{e}(t)$	Normalized excitation
$F_{\text{AT}}$	Achilles tendon force
$\hat{F}_a(l_f)$	Normalized active force-length relationship of muscle fibre
$\hat{F}_a(v)$	Normalized active force-velocity relationship of muscle fibre
$\hat{F}_{a,\text{fast}}(v)$	Normalized active force-velocity relationship of fast muscle fibre
$\hat{F}_{a,\text{slow}}(v)$	Normalized active force-velocity relationship of slow muscle fibre
$F_f$	Fibre force

$F_{LG}$	Lateral gastrocnemius force
$F_{MG}$	Medial gastrocnemius force
$F_m$	Muscle force
$F_{max}$	Maximum isometric force
$\hat{F}_p(l_f)$	Normalized passive force-length relationship of muscle fibre
$F_t$	Tendon force
$f$	Frequency of the EMG signal
$f_c$	Central frequency of a wavelet
$K$	Hill's equation empirical constant 3
$k_{AT}$	Achilles tendon stiffness
$k_{SEE,T}$	Series elastic element stiffness for the toe region
$k_{SEE}$	Series elastic element stiffness for the linear region of Achilles tendon force-length curve (equivalent to $k_{AT}$ )
$\bar{k}_{SEE}$	Group average series elastic element stiffness
$k_{SEE-LG}$	Series elastic element stiffness of the LG
$k_{SEE-MG}$	Series elastic element stiffness of the MG
$l_{apo}$	Aponeurosis length
$l_{apo,i}$	Aponeurosis length, initial
$l_{apo,c}$	Aponeurosis length, current
$l_{AT}$	Achilles tendon length
$l_{AT-LG}$	Achilles tendon length measured at the LG muscle-tendon junction
$l_{AT-MG}$	Achilles tendon length measured at the MG muscle-tendon junction
$l_{0,AT}$	Achilles tendon slack length
$l_{0,AT-LG}$	Achilles tendon slack length measured at the LG muscle-tendon junction
$l_{0,AT-MG}$	Achilles tendon slack length measured at the MG muscle-tendon junction
$l_b$	Muscle belly length
$l_f$	Fascicle length
$l_{0,f}$	Fascicle slack length
$l_{f,i}$	Fascicle length, initial
$l_{f,c}$	Fascicle length, current
$l_{f,opt}$	Optimal muscle fibre length
$l_{ft}$	Fascicle thickness

$l_{fw}$	Fascicle width
LG	Lateral gastrocnemius
MG	Medial gastrocnemius
MTJ	Muscle-tendon junction
MTU	Muscle-tendon unit
$n$	Fascicle shape factor
PCSA	Physiological cross-sectional area
PEE	Parallel elastic element
$s$	Wavelet scaling factor
SEE	Series elastic element
SOL	Soleus
$t$	Muscle thickness
$T$	time
TA	Tibialis anterior
TDC	Pedal top-dead-centre
$\hat{v}$	Normalized fascicle velocity
$v_0$	Maximum intrinsic speed
$V_m$	Muscle volume
$w$	Muscle width
$x$	Distance that fascicle cross-sections occupy along the muscles line of action
$\sigma$	Stress
$\sigma_0$	Maximum isometric stress
$\varepsilon$	Strain
$\dot{\varepsilon}$	Strain rate
$\alpha$	Curvature of force-velocity relationship
$\beta$	Pennation angle
$\beta_i$	Pennation angle, initial
$\beta_c$	Pennation angle, current
$\beta_{act}$	Ratio of the activation to deactivation time constants
$\tau_{act}$	Activation time constant
$\psi(f)$	Wavelet function

---

# Chapter 1.

## Introduction

Skeletal muscle is the engine that powers what is arguably the most essential and defining feature of animal life—locomotion (Vogel, 2003). In particular, muscles function to change length and produce force to allow for movement (Biewener, 2003), posture (e.g., Smith et al., 1977), and balance (e.g., Winter et al., 2003). Despite this seemingly simple role, skeletal muscle displays a variety of phenomena that remain poorly understood. These phenomena are complex—the result of interactions between active and passive machinery, as well as chemical, electrical, and mechanical processes (Epstein and Herzog, 1998). In an effort to understand muscle mechanical behaviour and ultimately its functional role in locomotion, scientists often experimentally measure properties of muscle such as lengths, forces, and activation patterns (e.g., Roberts et al., 1997; Biewener, 1998a; Biewener, 1998b; Biewener et al., 1998a; Biewener et al., 1998b; Shadwick et al., 1999). Scientists also develop elegant mathematical arguments to explain how muscle works; existing muscle models (e.g.: Zajac, 1989; Winters, 1990; Alexander, 1992; Delp et al., 2007) have provided valuable insight into parameters that we cannot easily measure, elucidated mechanistic explanations for observed phenomena, and allowed ‘what-if’ questions to be asked. However, few studies have examined the accuracy and validity of such models applied to *in vivo* motor tasks. Integrating *in vivo* muscle properties, determined experimentally, together with muscle models, which is the central theme of this thesis, likely provides the most promising approach to better understand how skeletal muscle produces force to power locomotion in animals and humans.

In this chapter I will review the functional design of the muscle-tendon unit (MTU) as well as the mechanical and physiological properties that govern the performance of skeletal muscle. I will also discuss the suite of tools presently available—and studies that have used these tools—to measure muscle and tendon behaviour during movement in

non-human animals and humans. Finally, I will review Hill-type muscle models and their ability to predict muscle force as well as provide a mechanistic framework to test hypotheses about muscle-tendon behaviour during dynamic tasks.

## **1.1. Functional design and structural properties of the muscle-tendon unit**

Skeletal muscles are the engines that convert chemical energy (i.e., food) into mechanical work (i.e., length change and force) whereas tendons transmit force to the skeleton for effective movement (Roberts, 2002). Together, a muscle and its associated tendon(s) make up a MTU. It is the interactions between these active contractile components (muscle) and passive elastic machinery (tendon) that largely dictate the mechanical behaviour of the whole MTU. The integrated nature of muscle and tendons allows the mechanical output of a MTU to far exceed the capabilities of muscle contractile elements alone (Roberts, 2002). Active contractile structures such as the actin-myosin cross bridges are under the control of motor signals sent from the brain (Winter, 2009) whereas passive elastic tissues such as tendons and aponeurosis are not under conscious control yet play a critical role in efficient and economical locomotion by storing and releasing elastic energy and enabling muscle fibres to operate under more favorable contractile conditions (Purslow, 2002; Roberts, 2002).

Skeletal muscles are organized in a hierarchical structure (Figure 1-1). Sarcomeres are the basic force-generating functional unit of muscle. They are arranged in series, along with connective tissue, to make up a muscle fibre. Muscle fibres are bundled in parallel and series to form muscle fascicles that together make up a whole muscle. Pennate muscles are characterized by fibres that lie at an angle (i.e., the pennation angle) relative to the force-generating axis of the muscle. This angular arrangement allows for more sarcomeres to be packed in parallel within a given volume, increasing the physiological cross-sectional area (PCSA) and force-generating capacity of the muscle. In contrast, long parallel fibred muscles have a greater number of sarcomeres arranged in series, which allows the muscle to undergo greater absolute length changes and velocities in comparison with short-fibred pennate muscles (Lieber and Ward, 2011; Biewener and Roberts, 2000). Note that to compare the lengths and

velocities of muscles across animals of different sizes, we typically convert absolute lengths and velocities to strains and strain rates, respectively. Strain can be calculated as:

$$\varepsilon = \frac{l-l_0}{l} \quad (\text{Eq. 1-1})$$

where  $l$  is length and  $l_0$  is optimal or resting length, which is defined as muscle length at the plateau of the muscle's force-length relationship.

Strain rate can be calculated as:

$$\dot{\varepsilon} = \frac{d}{dT}(\varepsilon) \quad (\text{Eq. 1-2})$$

where  $T$  is time. Using these formulations, negative values for strains and strain rates represent shortening whereas positive values represent lengthening.

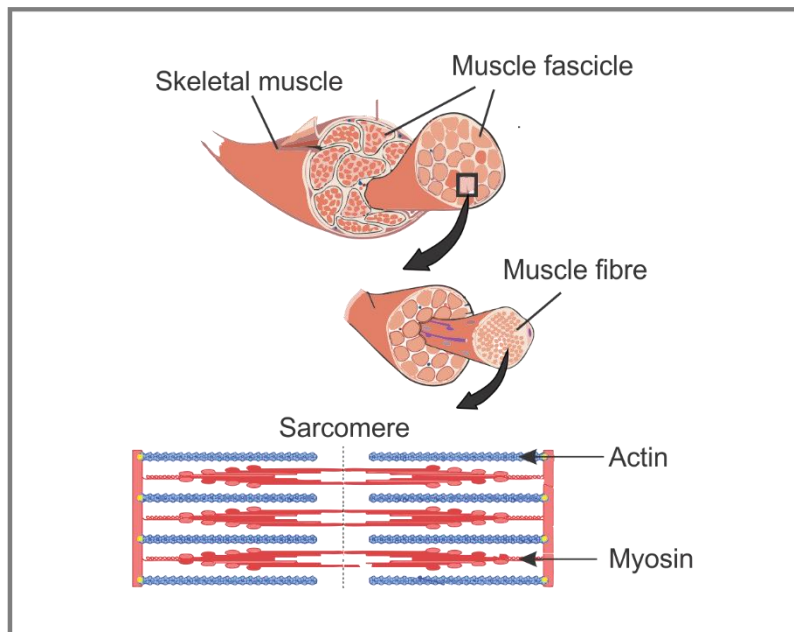


**Figure 1-1. Hierarchical structure of skeletal muscle.**

Skeletal muscle is organized in a hierarchical structure from sarcomeres to muscle fibres to muscle fascicles to whole muscle.

Muscle architecture is tightly linked to the design of the whole MTU. The arrangement of active and passive structures highly influences the functional behaviour of

a MTU. For example, muscles with short pennate fibres connected to long compliant tendons are often located in the distal limb to favour economical force production, where economy is the ratio of force produced to energy expended (Biewener, 1998a, Biewener, 1998b). In contrast, muscles with long fibres, arranged at very low pennation angles, are often attached to short stiff tendons and located more proximally to favour range of motion, joint position control, and power generation (Biewener, 1998a).

The human triceps surae-Achilles tendon (AT) complex is an important and practical system to investigate muscle mechanical behaviour and test muscle-tendon models. The triceps surae muscle group is comprised of the medial gastrocnemius (MG), lateral gastrocnemius (LG), and soleus (SOL) (Figure 1-2). All three muscles generate an ankle plantarflexion moment, whilst the MG and LG are biarticular and also generate a knee flexion moment. These muscles play an important role in force generation during legged locomotion. In fact, the ankle plantarflexor muscles across a wide range of animals, including wallabies, kangaroos, turkeys, guinea fowl, horses, and humans (Ker et al., 1987; Roberts et al., 1997; Biewener, 1998b; Biewener et al., 1998d; Daley and Biewener, 2003; Fukunaga et al., 2001; Lichtwark et al., 2007), appear to have been selected for economical locomotion. Characterized by short pennate fascicles, these three muscles have large PCSAs for their volumes, and their fascicles have the ability to shorten as well as rotate during contraction (e.g., Fukunaga et al., 1997; Kawakami et al., 1998; Azizi et al., 2008; Randhawa et al., 2013). The MG, LG, and SOL share a common insertion onto the calcaneus via the long, compliant Achilles tendon that stores and returns elastic energy during the gait cycle (Alexander, 1988), stretching up to 10 % in humans (Finni et al., 2003; Maganaris and Paul, 2002). Computer simulations of human walking and running have shown that the human plantarflexors contribute the majority of the force necessary for vertical body weight support and forward propulsion during the second half of the stance phase (Neptune et al., 2001; Anderson and Pandy, 2003; Dorn et al., 2012; Hamner and Delp, 2013). Also relevant to the investigations performed here, the superficial location of the structures within the muscle-tendon complex make them amenable to imaging and recording surface signals with high fidelity.

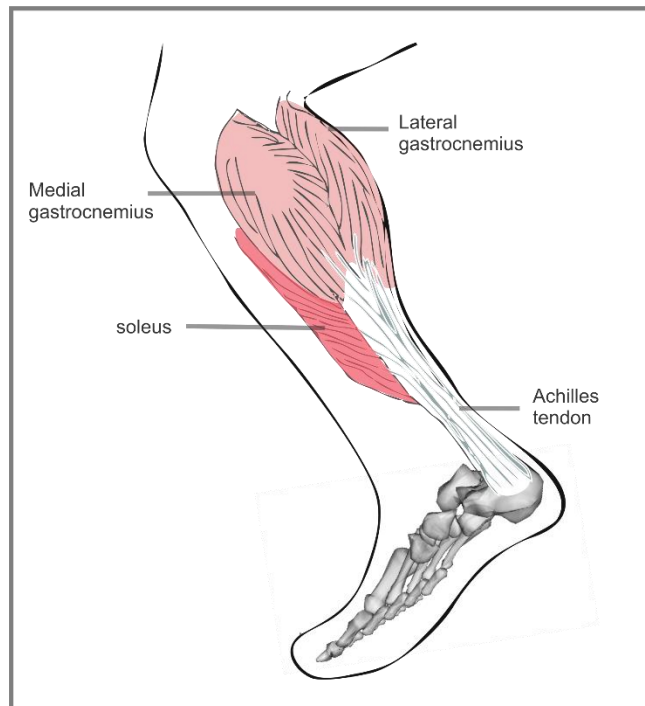


**Figure 1-2. Anatomy of the human triceps surae-Achilles tendon complex.** The triceps surae muscle group consists of the soleus, medial gastrocnemius and lateral gastrocnemius, which share a common insertion on the calcaneus via the Achilles tendon (illustration shown for the right leg).

## 1.2. Physiological properties of skeletal muscle

While the force generated by whole muscle depends on the muscle's architecture and size, the ability of individual muscle fibres to generate force depends on three fundamental properties: activation, length, and velocity. Activation is governed by the electrical signals sent from the brain to the relevant motor neurons, which we can estimate from a muscle's excitation, determined using electromyography (EMG). The force developed by muscle fibres is also dependent on two other physiological properties: (i) the force-length relationship and (ii) the force-velocity relationship (Figure 1-3). These two relationships determine the force that a fibre can produce as a function of its normalized length and contraction velocity.

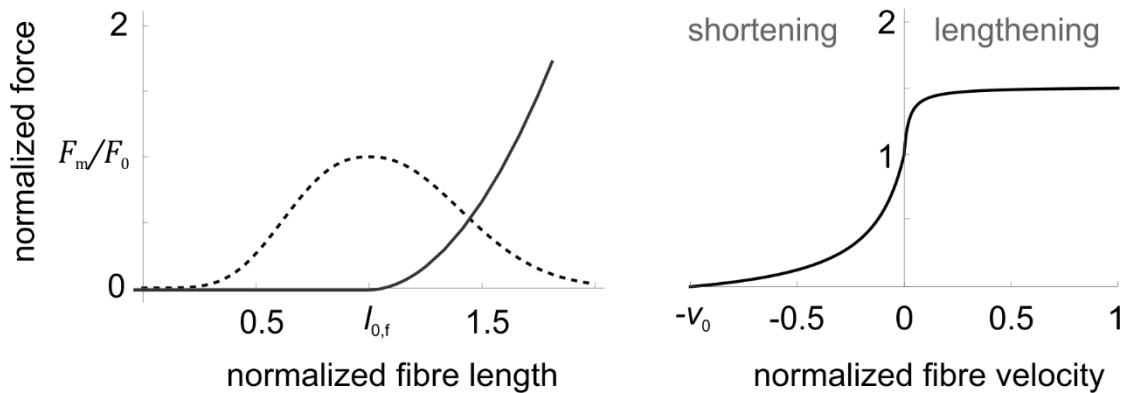


**Figure 1-3. Force-length and force-velocity relationships of skeletal muscle.** Typical active (dashed) and passive (solid) force-length curves of muscle (left) relative to the optimal muscle fibre length,  $l_{0,f}$  and the maximum isometric force,  $F_0$ . A typical force-velocity curve of muscle (right) relative to maximum intrinsic speed,  $-v_0$  and the maximum normalized isometric force,  $F_m/F_0$  separated into shortening (negative) and lengthening (positive) regions.  $F_m$  represents muscle force.

Over a century ago, Blix was first to show that the force developed by a muscle depends on its operating length (Blix, 1894) and later Gordon and colleagues (1966) presented similar results within single fibres. These force-length properties can be separated into active and passive components. The active forces are a result of bound cross bridges that form between the molecular motor proteins actin and myosin within sarcomeres that act in parallel as independent force generators (Gordon et al., 1966). The greater the number of cross bridges bound, the greater the force developed. For example, on the region of peak force of the force-length curve (Figure 1-3), sarcomeres and thus muscle fibres operate at lengths optimal for cross bridge binding and effective force development (Gordon et al., 1966). At lengths shorter or longer than optimal, defined as  $l_{0,f}$ , there is a reduction in the number of available cross-bridge binding sites due to either excessive actin-myosin overlap (ascending limb) or excessive stretch (descending limb) (Figure 1-3). Muscle also develops passive forces when stretched beyond optimal length. The passive force-length properties result from the connective tissue components within and surrounding muscle fibres (Williams and Goldspink, 1984) as well as the intra-sarcomeric protein titin (Prado et al., 2005). Passive forces are important to resist excessive muscle stretch and prevent muscle damage that occurs when skeletal muscles are stretched to long lengths (Proske and Morgan, 2001). As well, the passive properties contributed by titin lead to a phenomenon known as “passive force enhancement” by which higher than isometric forces can be reached when a contracting muscle is actively

stretched (Joumaa et al., 2008). Some studies suggest that the passive force-length relationship differs across muscles and animals (McMahon, 1984; Gareis et al., 1992; Brown et al., 1996; Azizi and Roberts, 2010). For example, it has been suggested that pennate muscles may have different passive force-length properties than parallel fibred muscles owing to a greater proportion of connective tissue (McMahon, 1984), yet to my knowledge, this remains to be experimentally tested.

The force developed within a muscle fibre depends not only on its length, but also on its instantaneous rate of length change or velocity (Hill, 1938). The force-velocity relationship demonstrates that a muscle develops highest forces during lengthening (eccentric) contractions; however when shortening, force decreases as muscle shortening velocity increases (Figure 1-3). A muscle is unable to develop active forces when shortening at velocities equal to or greater than its maximum intrinsic speed, or maximum unloaded shortening velocity,  $-v_0$ . This decay in a muscle's ability to develop force results from the inability of unbound myosin cross bridges to successfully bind with actin, which increases with velocity (Huxley, 1974).

Early experiments on the behaviour of skeletal muscle have provided a great deal of information about the force that a muscle can generate while contracting at a given length and velocity (Hill, 1938; Gordon et al., 1966). However, these experiments were performed under conditions of constant length or load at maximum activation. During everyday movements, it is unlikely that muscles are maximally activated at constant lengths or forces. To date, much of what we know about the mechanical and physiological properties of skeletal muscle have come from experiments, similar to those of Hill and Gordon, where single fibres or bundles of fibres were removed from a single muscle of an animal and maximally stimulated under a constant speed or load (e.g., Hill, 1938; Gordon et al., 1966). We still have much to learn about the relationships between functional characteristics of single fibres measured under controlled steady-state laboratory conditions and whole muscle behaviour within intact animals during real life dynamic tasks.

The force developed by a muscle also depends on its activation state (Ashley and Ridgeway, 1968). Muscles are excited when the nervous system sends an electrical signal

through a motor neuron to its associated muscle fibres (Sandlow, 1952). If above a certain threshold, these electrical signals, defined as action potentials, result in the depolarization of a muscle cell. This depolarization initiates the release of calcium ions from their storage site in the sarcoplasmic reticulum. Once released, calcium triggers a cascade of events that eventually allow myosin heads to bind to nearby actin filaments so that cross bridges can form and generate force (Ebashi and Endo, 1968). Thus the actin-myosin interaction, and ultimately a muscle's ability to shorten and produce force, is regulated by the intracellular calcium concentration (Morris et al., 2001). We can think of muscle activation as a measure of the calcium ion concentration within the muscle cell—the higher the concentration of calcium, the increased ability of a muscle fibre to generate force (Ashley and Ridgeway, 1968).

For any given motor task, the nervous system must decide which fibres within a muscle to activate. Skeletal muscle contains different types of muscle fibres that can be broadly classified into two groups based on their mechanical and energetic properties: slow and fast twitch fibres (Burke et al., 1973). The fatigability, mechanical power output, and force-velocity properties vary greatly between fibre types (Faulkner et al., 1986; Epstein and Herzog, 1998; Bottinelli et al., 1999). For example, fast muscle fibres fatigue more rapidly than slow fibres (Schiaffino and Reggiani, 2011) but are characterized by a higher maximum intrinsic speed and faster activation-deactivation rates in comparison to slow fibres (Burke et al., 1973; Epstein and Herzog, 1998). The contractile properties of muscle fibres are related to the maximum intrinsic speed at which they can shorten. The shortening velocity at which the maximum mechanical power is generated (25-36 % of maximum intrinsic speed; Kushermick and Davies, 1969; Swoap et al., 1997; He et al., 2000) and the velocity at which the maximum mechanical efficiency is achieved (15-29 % of maximum intrinsic speed; Hill, 1938; He et al., 2000) are both functions of maximum intrinsic speed. Therefore, generating high mechanical power is best achieved using faster muscle fibres for contractions that involve high strain rates and rapid activation–deactivation rates (Rome et al., 1988).

Despite what is known about the contractile properties of different muscle fibre types, questions about motor unit recruitment remain unanswered. For example, strategies that favor the recruitment of faster fibres for tasks that involve high strain rates

are not entirely consistent with Henneman's size principle—a keystone theory in motor unit recruitment (Henneman 1957; 1965a; 1965b). Henneman's theory suggests that motor units, defined as a motor neuron and the skeletal muscle fibres it innervates (Buchtal and Schmalbruch, 1980), are recruited in an orderly fashion from smallest motor neurons, which innervate slow muscle fibres, to largest motor neurons, which innervate fast muscle fibres. Whilst the size principle appears consistent with recruitment patterns observed in many studies, particularly those at low velocities (Stotz and Bawa, 2001) including isometric contractions (Milner-Brown et al., 1973), it predicts that slow muscle fibres will be used for fast contractions, a situation that seems at odds with the contractile mechanics of the different muscle fibre types.

Numerous studies suggest that alternative recruitment strategies exist. For example, the cat paw shake illustrates why fast fibres are better suited for high-frequency tasks (Smith et al., 1980). Whilst not at the level of an individual muscle, this classical example demonstrates the mechanical argument of why fast fibres are better suited for certain tasks. During the high-frequency paw shake, the slow-fibred soleus was inactive while the fast-fibred lateral gastrocnemius was active. Preferential recruitment of fast fibres without slow fibres within a single muscle has been displayed in the vastus lateralis of the bushbaby during jumping (Gillespie et al., 1974), in the medial gastrocnemius of rats during running (Hodson-Tole and Wakeling, 2007), and in the gastrocnemii (Wakeling et al., 2006) and quadriceps (Citterio and Agostoni, 1984) of humans during high speed cycling.

These studies provide evidence that muscle fibres may be recruited so that fibre-type properties are matched with the mechanical demands of the locomotor task. Recent evidence from our lab further suggests that incorporating information about the different mechanical properties and recruitment patterns of slow and fast fibres into muscle models improves the models' predictions of whole muscle force (Wakeling et al., 2012; Lee et al., 2013). These experimental and modelling results indicate that it may be important to consider the independent contributions of slow and fast fibres on the mechanical output of a mixed fibre muscle; however, to date this remains unexplored when modelling human muscle force.

In summary, the force generated by a muscle depends on its architecture and size, as well as its activation state, force-length, and force-velocity properties. Slow and fast muscle fibres differ in their mechanical and energetic properties and evidence suggests that fibre recruitment can be matched with the mechanical and energetic demands of the movement task. With information about these fundamental properties, we can estimate the force, work, and power generated by a muscle during *in vivo* movements.

### **1.3. *In vivo* measures of muscle-tendon behaviour**

Only a few research laboratories worldwide have evaluated the mechanical behaviour of muscles in animals during *in vivo* motor behaviours by recording fascicle lengths, forces, and excitations using a combination of implanted sensors that include sonomicrometry, tendon buckles, and intramuscular EMG. These measurements have been made for a wide range of locomotor tasks such as flying (Biewener et al., 1998c), swimming (Shadwick et al., 1999), hopping (Biewener et al., 1998d), and running (Roberts et al., 1997) and have provided valuable insight into how the mechanical and physiological properties of skeletal muscle determine the energetics, mechanics and overall mechanical performance of selected skeletal muscles during movement. Not surprisingly, fewer studies have directly measured *in vivo* forces in humans using tendon buckles and optic-fibre techniques during dynamic tasks such as walking (Finni et al., 1998), running (Komi et al., 1996), jumping (Fukashiro et al., 1995), and cycling (Gregor et al., 1987). Obtaining direct measurements of *in vivo* muscle length and force in humans is associated with a suite of ethical and technical issues due to the highly invasive nature of the surgical procedures and thus are not commonly used.

But rather, human movement has traditionally been analyzed using tools such as motion capture, force plates, and EMG (For Review: Winters, 2009). These methods provide quantitative measurements of kinematics, kinetics, and muscle coordination patterns during human motor tasks and allow us to make inferences about muscle and tendon function. However, the strains and strain rates of muscle fibres are difficult to predict from joint motions alone for two main reasons. First, muscle forces are transmitted to bones via elastic tendons, and this tendon elasticity uncouples the strains and strain rates of muscle fibres from those of the whole MTU, as estimated from motion capture

(Roberts, 2002). This is especially apparent in the triceps surae muscles, where the tendon ( $\approx 150$  mm) is much longer than muscle fibres ( $\approx 44$ -59 mm) (Ward et al., 2009). As such, the Achilles tendon acts as a buffer to allow muscle fibres to contract at lower (or even higher) shortening velocities than the muscle belly and MTU (e.g., Wakeling et al., 2011; Arnold et al., 2013; Lai et al., 2015). Second, pennate muscles such as the MG, LG, and SOL can rotate during contraction (Fukunaga et al., 1997; Kawakami et al., 1998; Maganaris et al., 1998a; Wakeling et al., 2011; Zuurbier and Huijing, 1993). This allows muscle fibre velocities to be uncoupled from the shortening velocity of the MTU in a process known as gearing (e.g., Azizi et al., 2008; Wakeling et al., 2011). Therefore, estimates of MTU length from kinematics provide limited insight into the mechanical behaviour of the active (muscle fibres) and passive (tendon) structures and their ability to produce and transmit force during movement.

An alternative approach for estimating the behaviour of skeletal muscle during human movement is inverse dynamics. Traditional inverse dynamics uses measurements of joint motions together with the experimental ground reaction forces to solve for the net reaction forces and net moments at each of the joints (e.g., Gregor et al., 1991; Smak et al., 1999; Litchwark and Wilson, 2005a). However, determining the amount of force that each muscle contributes to the net joint moment remains difficult and often requires optimization approaches (e.g., Crowninshield and Brand, 1981; Anderson and Pandy, 1999; Hamner et al., 2010).

In recent years B-mode ultrasound has emerged as a valuable tool to study *in vivo* properties of muscle and tendon non-invasively during a range of movement tasks. Some of the earliest ultrasound studies of the human gastrocnemii and AT showed that pennation angle changes as a function of both joint angle and joint torque (Narici et al., 1996) and that the tendon and aponeurosis undergo different strains during isometric contractions (Fukashiro et al., 1995). In more recent years, ultrasound has been coupled with motion capture to enable 2D ultrasound images to be projected into 3D space. This has been shown to be a valuable technique to measure muscle volume (Barber et al., 2009), fascicle length (Malaiya et al., 2007), and muscle fascicle architecture (Rana and Wakeling, 2011). Additionally, ultrasound has been used to examine the mechanical properties of the Achilles tendon (Maganaris and Paul, 2002; Muraoka et al., 2005;

Lichtwark and Wilson, 2005a; Zhao et al., 2009; Morrison et al., 2015) illustrating that tendon stiffness varies between individuals.

B-mode ultrasound has also been used to determine the *in vivo* behaviour of muscle and tendon together during human movement. Fukunaga and colleagues (2001) demonstrated that during walking, MG length changes were uncoupled from joint motion and the associated MTU lengths due to the series elasticity of the Achilles tendon. Since then, ultrasound has been used to measure fascicle or tendon behaviour in the triceps surae and Achilles tendon during walking (Lichtwark and Wilson, 2006), running (Lai et al., 2014), jumping (Lichtwark and Wilson, 2005a), and cycling (Wakeling et al., 2006). But few studies have measured both the behaviour of the muscle fascicle and the tendon together during dynamic tasks.

When combined with other experimental techniques, ultrasound imaging may provide even more information than past researchers have identified. B-mode ultrasound can measure tendon stretch (e.g., Lichtwark and Wilson, 2005a; Kongsgaard et al., 2011). Given that tendons are elastic structures that transmit force relative to the amount of stretch they undergo (Ker, 1981; Matson et al., 2012), we can combine ultrasound measurements of tendon stretch together with the tendon's mechanical properties (e.g., stiffness and slack length) (Morrison et al., 2015) to estimate subject-specific *in vivo* tendon forces during dynamic tasks. To my knowledge, this has not yet been done.

Another technique often used by researchers to infer the mechanical behaviour of skeletal muscle is EMG. EMG measures the electrical signals that occur when action potentials depolarize muscle cells, known as muscle excitations, and can be used to determine the timing and level of muscle excitation during a particular motor task (e.g., De Luca, 1997; Wakeling, 2009). However, the EMG signal contains much more information than most researchers use, and advanced EMG processing techniques such as wavelet analysis (Von Tscharner, 2000) take us one step further by enabling us to identify information about the recruitment of different fibre types within an individual muscle.

Slow and fast motor units possess action potentials that differ in shape and conduction velocity; this results in the different fibre types producing characteristic spectra within the EMG signal (Olson et al., 1968; Buchthal et al., 1980; Kupa et al., 1995; Von

Tscharner and Barandun, 2010). We can use time-frequency analysis techniques, such as wavelet analysis, to discriminate the recruitment of slow and fast motor units within a single muscle by these characteristic spectra (Wakeling and Rozitis, 2004). When recording EMG signals, an action potential travelling faster will travel past the electrode in less time; given that frequency is inversely related to time (Lindström and Magnusson, 1977), the fast fibres will be characterized by higher frequencies within the EMG signal. This has important implications for characterizing how muscle fibres are recruited in both healthy individuals and those with recruitment deficits such as post-stroke (Hafer-Macko et al., 2008) and in cerebral palsy (Wakeling et al., 2007). However, the ability to detect recruitment patterns from different muscle fibre types remains a controversial topic (e.g., Farina, 2008; von Tscharner and Nigg, 2008). This is predominantly because EMG spectra are additionally influenced by muscle fibre length, temperature, and fatigue status, and the spectral properties change as the electrical signals propagate through the soft tissues (Roeleveld et al., 1997; Blok et al., 2002; Wakeling, 2009). However, when these factors can be accounted for, it is then possible to use the EMG frequency information to understand motor unit recruitment (Wakeling and Lee, 2011).

In summary, the *in vivo* behaviour of human muscle and tendon can be measured using a variety of techniques that include ultrasound, EMG, motion capture, and force plates. Specifically, this thesis uses novel ultrasound-based methods to estimate time-varying forces and advanced EMG processing techniques to determine fibre-specific recruitment patterns. These biomechanical techniques have been developed, in part, and refined, within our laboratory. To date, there is no study that combines *in vivo* estimates of force with time-varying fascicle lengths, velocities, and pennation angles during human movement to understand the integrated behaviour of the tightly linked contractile and elastic machinery within a MTU. In this thesis, I combine ultrasound, motion capture, pedal reaction forces, and EMG techniques to predict muscle forces, lengths, and architecture during submaximal dynamic tasks. This provides a meaningful framework for testing the predictions of Hill-type muscle models and dynamic musculoskeletal simulations of human movement.

## 1.4. Models of skeletal muscle

Muscle models are ubiquitous in the field of biomechanics. They have become increasingly important tools in recent years, enabling more quantitative explanations of how the neural, muscular, and skeletal systems interact to produce movement (Zajac et al., 2002). Modelling provides a useful approach to probe parameters that we cannot directly measure in humans, determine cause-and-effect relationships, and ask 'what-if' questions. The increasing performance of computers continues to fuel scientists interest to develop and analyze musculoskeletal simulations that rely on these muscle models to uncover important insights into the biomechanical factors that contribute to healthy and pathological gait (e.g., Anderson and Pandy, 2003; Hamner et al., 2010; Peterson et al., 2010; Arnold et al., 2013).

The most common muscle model used in biomechanics is the Hill-type model. In 1938 A.V. Hill performed a very influential set of cleverly designed experiments and presented a phenomenological state equation that related the stress developed by a muscle to its contraction velocity (Hill, 1938):

$$(\sigma + a)(\dot{\epsilon} + b) = (K) \quad (\text{Eq. 1-3})$$

where  $\sigma$  is muscle stress,  $\dot{\epsilon}$  is strain rate, and  $a$ ,  $b$ , and  $K$  are constants. Hill's equation (Eq. 1-3) describes the force-velocity effect of muscle. However, a muscle's force also depends on its activation (Ashley and Ridgeway, 1968) and length (Gordon et al., 1966). The most commonly utilized Hill-type model has the form:

$$F_m = F_{\max} [\hat{a}(t) \hat{F}_a(l_f) \hat{F}_a(v) + \hat{F}_p(l_f)] \cos \beta \quad (\text{Eq. 1-4})$$

where the force generated by a muscle  $F_m$  is function of its activation state  $\hat{a}(t)$ , active force-length properties  $\hat{F}_a(l_f)$ , passive force-length properties  $\hat{F}_p(l_f)$ , and force-velocity properties  $\hat{F}_a(v)$ .  $F_{\max}$  is the maximum isometric force of the muscle and scales the muscle fibre force to whole muscle force. Pennation angle  $\beta$  allows the component of muscle force along the muscle's line of action to be estimated. One limitation of these models is that the active force-length properties and the force-velocity properties are typically based on steady-state laboratory experiments where muscles were fully activated, and these

properties may not be representative of muscles during submaximal *in vivo* behaviours (e.g., Rack and Westbury, 1969; Josephson and Edman 1988; Rassier et al., 1999; Holt et al., 2014).

The Hill-type model, not to be confused with ‘Hill’s equation’ (Eq. 1-3) that describes only the force-velocity relationship, can be formulated in different ways (e.g., Zajac, 1989; Winters, 1990). One of the most common formulations (Figure 1-4) is comprised of a contractile element (CE) and two non-linear spring elements: one in series, the series elastic element (SEE), and another in parallel, the parallel elastic element (PEE). The active force of the contractile element comes from the force generated by the actin and myosin cross-bridges within the sarcomeres. The PEE represents the passive force of the connective tissues (epimysium, perimysium, and endomysium) that surround the contractile element as well as the protein titin, and is responsible for the muscle’s passive behaviour when it is stretched actively or passively beyond optimal length. The SEE represents the tendon and aponeurosis.

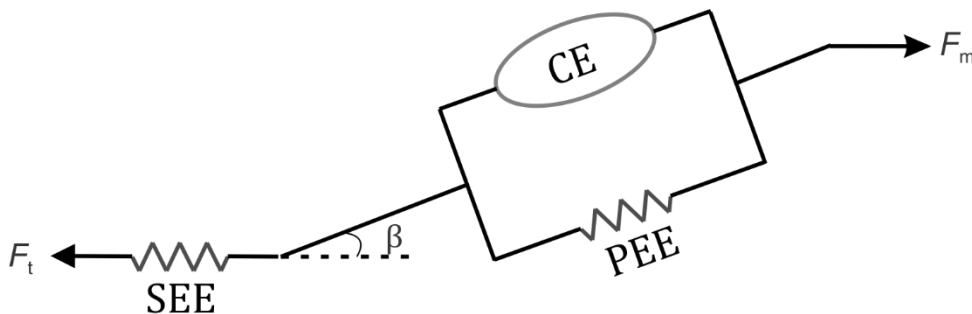


**Figure 1-4. Representation of a Hill-type muscle model.**

The contractile element (CE) represents the active forces generated by the actin-myosin cross bridges. The parallel elastic element (PEE) represents the passive force of the connective tissues (epimysium, perimysium and endomysium) that surround the contractile element as well as titin. The series elastic element (SEE) represents properties of the tendon.  $\beta$  represents pennation angle—the angle at which the fibres are arranged relative to the force-generating axis of the muscle.

Hill-type muscle models are key components of muscle-driven dynamic simulations that have been developed to estimate the forces produced by muscles during walking (Anderson and Pandy, 2003), running (Hamner et al., 2010), cycling (Kautz and Neptune, 2002) and jumping (Anderson and Pandy, 1999), as well as to establish a scientific basis for planning surgery and therapy in clinical populations (Fregly et al., 2012).

However, such studies are not yet being widely incorporated into clinical practice due, in large part, to the paucity of validation experiments. Though some effort has been made to verify scaled length-tension relationships for whole muscles (e.g., Winters et al., 2011), and some studies have been done to qualitatively confirm the actions of a few muscles predicted by models (e.g., Hernandez et al., 2010; Arnold et al., 2013), the accuracy with which Hill-type models estimate *in vivo* muscle forces within simulations of walking, cycling, or other dynamic movements remains unknown. Without validation or quantitative comparisons with *in vivo* experimental data, the ability of models to predict muscle forces and guide surgery or treatment planning in persons with movement abnormalities remains limited.

A handful of studies have examined the accuracy with which these types of Hill-type models predict time-varying *in situ* and *in vivo* forces measured directly in animals (Sandercock and Heckman, 1997; Perreault et al., 2003; Wakeling et al., 2012; Lee et al., 2013; Kim et al., 2015). The results from these studies have revealed substantial variation in model accuracy, with models predicting between 40 % and 90 % of the measured force depending on whether experiments were performed *in situ* or *in vivo*. Thus, traditional formulations of Hill-type models remain unable to consistently reproduce the forces generated by skeletal muscle during contraction. This thesis aims to address some of the limitations (or assumptions) of traditional Hill-type models that may diminish their accuracy, particularly when assessing *in vivo* motor tasks that involve time-varying submaximal muscle contractions.

One limitation of traditional Hill-type models is their inability to account for the activation state of different types of muscle fibres. Though there have been one or two attempts to accommodate fibre-type specific model parameters (e.g., Umberger et al., 2003; Lee et al., 2013), these models have yet to be widely adopted within the biomechanics community. Most models assume a single contractile element with force-length and force-velocity properties estimated from *in vitro* or *in situ* data collected under maximally-activated conditions. However, most skeletal muscles are a composite of slow and fast motor units with different physiological and biomechanical properties (Bottinelli et al., 1999; Epstein and Herzog, 1998; Faulkner et al., 1986). The parameters that drive a Hill-type model, such as the force-velocity properties, depend on the type of motor unit

recruited yet such factors are neglected in traditional Hill-type models (e.g., Zajac, 1989; Winters, 1990; Delp et al., 2007; Millard et al., 2013). Given the growing body of evidence that suggests the recruitment of slow and fast motor units is altered with the mechanical demands of the locomotor task (Gillespie et al., 1974; Citterio and Agostoni 1984; Wakeling et al., 2006; Hodson-Tole and Wakeling, 2007). Yet it remains unclear whether accounting for independent recruitment patterns of slow and fast motor units and their associated physiological properties is important when modelling whole muscle force during submaximal contractions in humans. In this thesis, I aim to test this question.

Another limitation is that traditional Hill-type models are one-dimensional (1D) and greatly simplify the effects of dynamic changes in muscle shape that determine the velocity of the muscle fibres in relation to the whole MTU. Traditional muscle models allow pennation angle to vary but do not allow muscle thickness to change during contraction (Zajac, 1989; van den Bogert et al., 2011; Millard et al., 2013). This assumption offers a convenient 1D approach for enforcing a constant volume constraint (Alexander and Vernon, 1975); however, recent imaging studies have confirmed that a muscle's thickness, as well as its pennation, can change dramatically *in vivo* (Zuurbier and Huijing, 1993; Fukunaga et al., 1997; Kawakami et al., 1998; Maganaris et al., 1998a; Wakeling et al., 2011). These shape changes may be important in modulating the velocity at which a muscle fibre contracts. During contraction, muscle fibres rotate; this allows muscle fibre velocity to be uncoupled from the velocity of the muscle belly or MTU in a process known as gearing (Azizi and Brainerd, 2007; Azizi et al., 2008; Wakeling et al., 2011). Studies have shown that gearing is not fixed, but rather changes depending on the speed and force of the contraction, with higher gearing values associated with high-speed low-force contractions (Azizi et al., 2008; Wakeling et al., 2011). Traditional muscle models are unable to predict this 'variable' gearing mechanism and may therefore underestimate *in vivo* force under certain mechanical conditions. Some studies question the validity of the 1D modelling approach (Herbert and Gandevia, 1995) while others suggest that assuming constant thickness is an appropriate modelling assumption under relatively constrained single-joint movements (Randhawa and Wakeling, 2015). At present, a mechanistic framework that tests the functional consequences of muscle shape changes and gearing — formulated for Hill-type models of varying dimensions and tested against *in vivo* recordings — does not exist. My thesis aims to fill this gap.

## 1.5. Outline and specific aims of this thesis

This thesis is part of a large multi-centre project between Simon Fraser University and Harvard University. An overarching goal of this project is test and refine methods for assessing muscle function using advanced Hill-type models and dynamic musculoskeletal simulations, together with non-invasive ultrasound and EMG measures, which can better predict muscle mechanical output under *in vivo*, time-varying conditions.

To address this goal, I collected a large set of biomechanical data from twenty elite cyclists. These data sets included an isometric protocol in which I measured the mechanical properties of each subject's Achilles tendon (AT) and a cycling protocol in which I simultaneously recorded muscle fascicle and tendon lengths using B-mode ultrasound, muscle excitation patterns using surface EMG, pedal reaction forces, and lower limb kinematics. I acquired these data for the LG and MG muscles at 11 different combinations of cadence and crank load to determine how the muscles' mechanical properties (muscle and tendon length, architecture, and muscle-tendon forces and recruitment patterns) vary with speed and load. I have developed an innovative ultrasound and EMG based approach to estimate the time-varying muscle-tendon forces during cycling. Using this information, I have tested the accuracy with which traditional Hill-type models as well as refined Hill-type models that incorporate information about motor unit recruitment (2-element models) and muscle shape changes (2D and 3D models) predict time-varying *in vivo* muscle forces (Figure 1-5). These studies are significant, as they are the first to directly compare time-varying muscle forces determined from subject-specific, Hill-type models, tested in a variety of formulations, to the muscle-tendon forces estimated *in vivo* from tracked ultrasound images. Specifically, these thesis chapters are my contributions to the project.

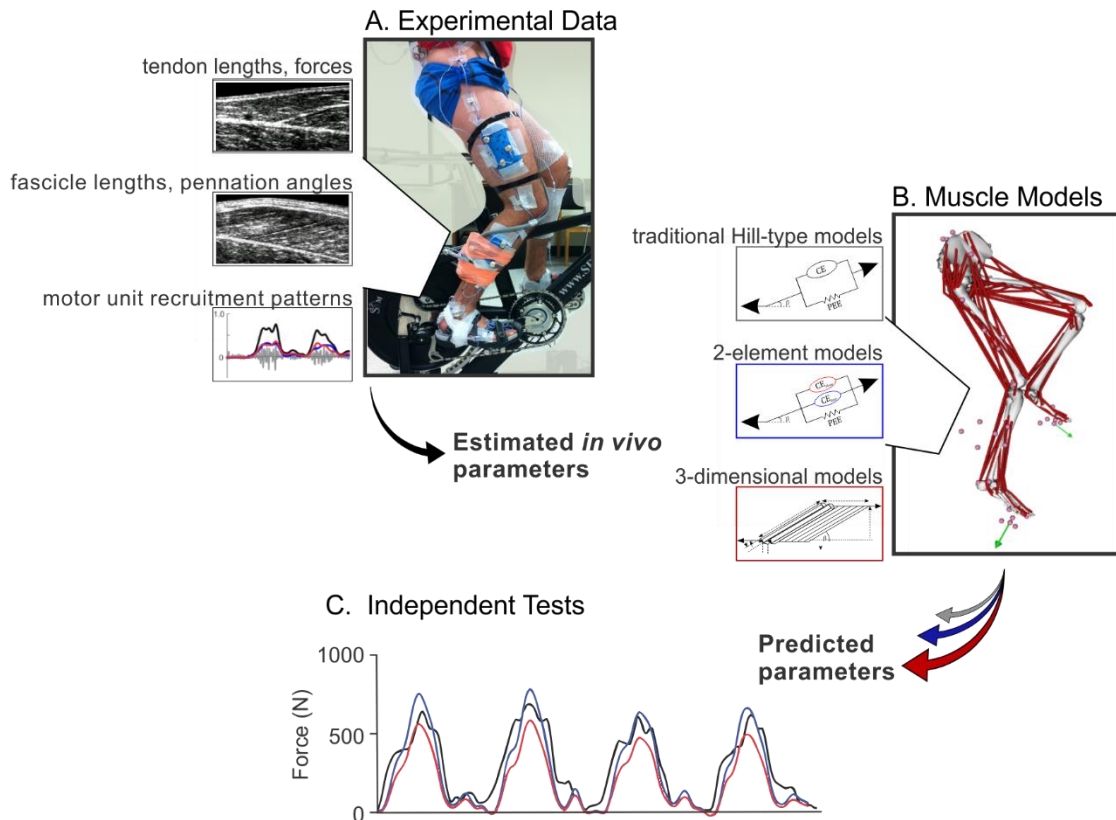


**Figure 1-5. Overview of thesis.**

This thesis integrates *in vivo* experimental data with novel Hill-type muscle models. From (A) I obtained estimates of time-varying *in vivo* length changes, forces, and muscle activations determined experimentally. From (B), I obtained predictions of the same parameters from muscle models. I tested traditional Hill-type models as well as novel models that incorporate information about motor unit recruitment and muscle shape changes. By comparing the ultrasound-based estimates with model predictions (C), I am refining assessments of muscle mechanical output under submaximal dynamic conditions.

Cycling provides an ideal paradigm for these studies because the kinematics are constrained and highly repeatable, facilitating simultaneous ultrasound and EMG recordings, and because unlike weight-bearing tasks such as walking and running, cadence and load can be varied independently to elicit a range of motor unit recruitment patterns.

The specific aims of this thesis were:

**Aim (1)** In chapter two I aimed to develop and evaluate a procedure for estimating time-varying *in vivo* AT forces from ultrasound-based measurements of AT length during cycling.

**Aim (2)** In chapter three I aimed to compare the time-varying gastrocnemii forces predicted by a traditional Hill-type model to ultrasound-based estimates of force. Because the traditional Hill-type model fails to account for variable activation states of slow and fast muscle fibres, I additionally aimed to test a two-element Hill-type model that includes both slow and fast contractile elements.

**Aim (3)** In chapter four I aimed to establish a comprehensive understanding of how activation and force affect dynamic muscle shape change, to include fascicle shortening velocity, pennation, thickness and gearing, across a wide range of mechanical demands.

**Aim (4)** In chapter four, I also aimed to compare predictions of muscle architecture (fascicle lengths and pennation angles) generated from a 1D Hill-type model and additionally from 2D and 3D geometric models that allowed for dynamic shape changes to occur.

Despite the abundance of muscle models and whole body dynamic musculoskeletal simulations within the biomechanics community, their clinical application, particularly on a subject-specific basis, remains limited due to the lack of validation studies that compare model predictions against *in vivo* data. To date, our ability to measure human muscle force, non-invasively, during dynamic tasks has been limited. However, ultrasound-based measures of tendon length changes, combined with information about the tendons' mechanical properties, can be used to estimate time-varying forces during dynamic tasks. In **chapter two**, I developed and evaluated a procedure for estimating time-varying *in vivo* AT forces from ultrasound-based measurements of AT length changes. In particular, I used ultrasound-based measures of AT length changes, combined with information about the tendon's stiffness and slack length, to estimate subject-specific AT forces during human pedalling. To evaluate this procedure, I compared each subject's AT plantarflexion moments, calculated from the subject's estimated AT forces and moment arms during cycling, to the same subject's net ankle moments determined from traditional inverse dynamics. I showed that plantarflexion moments, derived from the ultrasound-based estimates of AT force, reproduced the temporal patterns of each subject's net ankle moments calculated from inverse dynamics—but only when the relative EMG intensities of the three muscles (MG, LG, and SOL) that insert into

the composite AT were considered. The proposed methods and results provided in Chapter 2 offer a non-invasive approach for studying *in vivo* muscle-tendon mechanics and estimating time-varying forces for which we can compare against the predictions of muscle models and muscle-driven simulations.

Hill-type models are ubiquitous in the field of biomechanics, providing estimates of a muscle's force as a function of its activation state and its assumed force-length and force-velocity properties. However, despite their routine use, the accuracy with which Hill-type models predict the forces generated by muscles during submaximal, dynamic tasks remains largely unknown. In **chapter 3** I compared gastrocnemii forces predicted by a traditional Hill-type model to ultrasound-based estimates of force determined in Chapter 2. Data collected in our lab has shown that the recruitment patterns of different muscle fibre types within the gastrocnemii of cyclists varies with cadence (Wakeling et al., 2006; Wakeling and Horn, 2009). However traditional Hill-type models are unable to account for the different recruitment patterns and activation states of slow and fast fibres when predicting whole muscle force during submaximal dynamic contractions. To address this, I also tested a differential model in **Chapter 3**, with two contractile elements that accounted for the independent contributions of slow and fast muscle fibres. Both the traditional one-element model and the differential two-element models were driven by subject-specific, ultrasound-based measures of fascicle lengths, velocities, and pennation angles and by activation patterns of slow and fast muscle fibres derived from surface EMG recordings.

My results in Chapter 3 showed that peak gastrocnemii forces predicted by the models were generally within 10 % of the peak forces estimated from the ultrasound-based methods provided within Chapter 2. However, the time-varying patterns of the predicted and estimated forces differed more, with  $r^2$  values ranging from 0.85 to 0.31 across subjects and pedalling conditions. Compared to the traditional one-element model, I hypothesized that the two-element model would better reproduce the estimated forces at the higher cadences, because it comprised slow and fast contractile elements with different force-velocity properties and accounted for increased recruitment of fast fibres at the higher cadences. This hypothesis was confirmed, though improvements in the predicted forces were small. To my knowledge, this is the first study to evaluate the predictions of Hill-type models based on estimates of *in vivo* forces derived from

ultrasound-based measures of tendon length changes and stiffness. Here, we provide evidence that Hill-type models of human muscle can be as accurate as Hill-type models of animal muscle. This is notable given that the models tested in this thesis were driven with non-invasive inputs, measured using B-mode ultrasound and surface EMG, and the equations that described the muscle models (e.g., active and passive force-length relationships, force-velocity relationship, excitation-activation transfer functions) were determined from literature values. Whereas previous animal models (e.g., Lee et al., 2013) obtained direct invasive model inputs, measured using sonomicrometry and fine-wire EMG, and derived the equations that described their muscle model (e.g., active and passive force-length relationships, excitation-activation transfer functions, fibre proportions for force-velocity curvature) from directly measured *in situ* animal experiments.

Traditional Hill-type models also simplify the dynamic muscle shape changes that occur during contraction (e.g., Fukunaga et al., 1997; Kawakami et al., 1998). In **Chapter 4** I used measurements of tendon length, fascicle length, and pennation angle, determined using B-mode ultrasound, and muscle activation, determined using surface electromyography, to establish a comprehensive understanding of how activation and force affect dynamic muscle shape change, to include fascicle shortening velocity, pennation, thickness and gearing, across a wide range of mechanical demands. I found that the dynamic muscle shape changes and shortening velocities of contracting muscle fibres were tightly linked to muscle activation and force during pedalling. I found a greater effect of force, rather than activation, underlying the observed changes in internal muscle geometry and gearing during submaximal dynamic contractions. In **Chapter 4** I also compared time-varying estimates of fascicle length and pennation angle predicted from a traditional Hill-type model which assumes 1D muscle geometry (constant thickness), to the predictions of 2D and 3D geometrical models that allowed for aponeurosis stretch and dynamic muscle fascicle shape changes, respectively. However, the predictions of pennation angles and fascicle lengths from the 2D and 3D models were similar to predictions from the 1D model which suggests that the traditional 1D Hill-type model may be sufficient to explain force-dependent alterations in internal muscle geometry under submaximal dynamic tasks. To my knowledge, this is the first study to (i) explore the influence of both activation and force on the dynamic muscle shape changes and mechanical behaviour of human skeletal muscle and to (ii) test predictions of the

multidimensional Hill-type muscle models, driven with *in vivo* muscle lengths and activations, during submaximal dynamic conditions.

Portions of this thesis have been published, or are in the process of being published elsewhere. Portions of Chapter 2 have been accepted in the *Journal of Biomechanics* (Morrison, Dick and Wakeling, 2015; Dick et al., 2016). The contents of Chapter 3 and Chapter 4 are being prepared to be submitted for publication.

## Chapter 2.

# Quantifying Achilles tendon force *in vivo* from ultrasound images

## 2.1. Introduction

Biomechanical simulations that enable accurate assessment of *in vivo* muscle-tendon forces have broad application to human health and life-long mobility. However, simulations have yet to be adopted widely in clinical practice, in large part due to gaps in validating the predicted forces to ensure their accuracy (Hicks et al., 2015). A critical step in this process requires the acquisition of independent data.

B-mode ultrasound has emerged as a useful tool for quantifying *in vivo* muscle-tendon parameters during movement. For example, ultrasound images of muscle fascicles have been recorded during walking, running (Lichtwark and Wilson 2006; Farris and Sawicki, 2012), and jumping (Kurokawa et al., 2001) and have been used to quantify fascicle strains. Ultrasound has also been used, with motion capture, to measure mechanical properties of the Achilles tendon (AT) under isometric conditions (Kongsgaard et al., 2011) and during walking (Lichtwark and Wilson, 2006) and hopping (Lichtwark and Wilson, 2005a). These and other studies (e.g., Maganaris, 2003) have shown that ultrasound-based approaches can provide measures of muscle-tendon mechanics that cannot be obtained from traditional motion capture. Ultrasound-based estimates of tendon force, obtained non-invasively, could provide some of the independent measures needed to test muscle models and muscle driven simulations.

Ultrasound-based measures of AT length changes, combined with information about the tendon's stiffness and slack length, could be used to estimate subject-specific AT forces during dynamic tasks. However, accurately determining the *in vivo* forces transmitted by a complex, composite tendon such as the AT remains challenging for several reasons. First, AT stiffness has been shown to vary across subjects (Magnusson et al., 2001; Kubo et al., 2003; Lichtwark and Wilson, 2005a; Morrison et al., 2015), and whether an average stiffness is sufficient to estimate force, or whether stiffness must be

measured on a per subject or per muscle basis, remains unknown. Second, three large muscles insert into the AT, and the relative contributions of the medial and lateral gastrocnemius (MG, LG) and soleus (SOL) to AT force may change, depending on the task (e.g., Wakeling and Horn, 2009; Wakeling et al., 2010). Thus, strains measured at a single muscle-tendon junction (MTJ) may not be representative of strains throughout the tendon (Franz et al., 2015). Third, AT strains that are calculated from measured length changes depend, in part, on the assumed slack length of the tendon; however, determining the AT's *in vivo* length at the start of force transmission is often not straightforward.

The purpose of this chapter was to evaluate a procedure for estimating *in vivo* AT force from ultrasound-based measurements of AT length changes. Two aspects of my procedure are novel: it characterizes AT stiffness on a subject-specific basis, and it accounts for changes in the relative EMG intensities of the MG, LG, and SOL. To evaluate the procedure, I asked competitive cyclists to pedal at a steady 80 r.p.m. cadence at 4 different crank loads while I collected a comprehensive set of kinematic, kinetic, EMG, and ultrasound data. Cycling offers a unique paradigm for characterizing AT mechanics and testing new methodology because loads can be varied to impose changes in the required joint moments without also imposing large changes in the excursions of muscle-tendon units (MTUs). From these data, I estimated the forces and moments transmitted by the AT during cycling. I compared these estimates to subjects' net ankle moments calculated from inverse dynamics, and I assessed the sensitivity of these estimates to measured values of AT stiffness, AT slack length, and relative EMG intensities of MG, LG, and SOL. These results provide new guidelines for estimating AT forces from ultrasound images.

## **2.2. Methods**

For this thesis I collected a large set of biomechanical data from twenty elite cyclists recruited from local cycling clubs (10 female and 10 male; Table 2-1; Table 2-2). These data sets include ultrasound images of the muscle belly and MTJ for both the MG and LG, the 3D trajectories of 32 motion capture markers, reaction forces at both pedals, and surface EMG patterns from 10 muscles. I acquired these data for 11 different combinations of cadence and crank load while subjects pedalled on a cycle ergometer,

and recorded additional data while subjects performed isometric plantarflexion contractions. Data analyses (unless otherwise specified) were performed in Mathematica (V10, Wolfram Research, Inc., Champaign, USA) using custom-written code.

**Table 2-1. Characteristics of the ten competitive female cyclists tested.**

Subject	Age (y)	Height (cm)	Mass (kg)	Max Isometric Force* (N)	AT Stiffness† (N mm <sup>-1</sup> )	AT Stiffness ID‡ (N mm <sup>-1</sup> )	Toe Region Stiffness § (N mm <sup>-1</sup> )	Toe Region Stiffness ID    (N mm <sup>-1</sup> )	AT Slack Length ¶ (mm)	AT Length (linear) ** (mm)	AT Slack Length ID †† (mm)	AT Length ID (linear) ‡‡ (mm)
1	30	167	65.8	3650	203.0	208	-	55.2	180.0	181.9	179.6	181.4
2	43	174	64.4	3450	170.1	165	-	26.8	218.5	220.8	217.8	220.1
3	24	171	65.8	3569	163.8	160.5	52.1	49.7	172.9	174.7	173.4	175.0
4	32	168	63.5	3355	153.3	155.7	-	38.5	196.9	198.9	196.4	198.6
5	26	167	58.0	3123	130.2	133.4	30.3	31.9	217.3	219.5	215.5	219.9
6	22	160	51.3	2965	149.1	148.1	-	25.3	181.3	183.2	182.4	184.0
7	26	173	80.7	4170	173.3	170.3	42.1	44.4	225.3	227.6	223.9	228.7
8	23	168	68.0	3803	121.2	127.2	37.4	36.4	201.1	203.2	200.6	202.2
9	20	165	67.3	3889	158.4	167.3	-	38.4	193.0	195.0	193.9	196.2
10	32	167	59.4	3384	224.8	216.6	-	48.7	164.6	166.3	165.8	167.0
Mean ± SD:	28±7	168±4	64.4±8	3536±361	164.7±31	165.2±24	40.4±7.9	39.5±9.0	195.1±21	197.1±19.8	194.9±18.8	197.3±19.7

\* Combined force-generating capacity of MG, LG, and SOL estimated from the muscles' scaled volumes (Handsfield et al., 2014) and optimal fibre lengths (Arnold et al., 2010) assuming a specific tension of 225 kPa (Spector et al., 1980; Roy et al., 1982).

† AT stiffness for the linear region of the force-length relationship measured in the isometric protocol.

‡ AT stiffness for the linear region of the force-length relationship determined using inverse dynamics estimated AT forces during pedalling, averaged across crank loads.

§ Stiffness for the toe region of the AT force-length relationship measured in the isometric protocol (was only able to resolve for 4 of the 10 subjects).

|| Stiffness for the toe region of the force-length relationship determined using inverse dynamics estimated AT forces during pedalling, averaged across crank loads.

¶ Slack length of the AT ( $l_{0,AT}$ ) (AT length at start of the toe region) estimated as the distance from the MG MTJ to the calcaneus at 310 ° of the crank cycle, averaged over all crank cycles.

\*\* AT length (linear) at the end of the toe region (where AT stiffness of the linear region starts) based on slack lengths calculated at 310 ° of the crank cycle.

†† Slack length of the AT ( $l_{0,AT}$ ) (AT length at start of the toe region) estimated as the distance from the MG MTJ to the calcaneus based on inverse dynamics estimated AT forces during pedalling, averaged across crank loads.

‡‡ AT length (linear) at the end of the toe region (where AT stiffness of the linear region starts) based on inverse dynamics estimated AT forces during pedalling, averaged across crank loads.

**Table 2-2. Characteristics of the ten competitive male cyclists tested.**

Subject	Age (y)	Height (cm)	Mass (kg)	Max Isometric Force* (N)	AT Stiffness ( N mm <sup>-1</sup> )†	AT Slack Length‡ (mm)
1	29	186	90.9	4211	202.7	238.8
2	28	167	68.0	3673	129.7	250.8
3	33	175	68.0	3414	212.7	197.5
4	32	183	63.0	3051	132.3	247.6
5	37	173	71.8	3741	230.8	215.7
6	30	179	70.3	3470	144.1	219.5
7	47	183	86.3	4244	251.3	213.2
8	43	183	86.5	4131	143.1	227.6
9	31	183	82.8	4228	154.6	232.7
10	24	178	78.9	3853	174.9	173.5
Mean ± SD:	33.4±7	179±6	76.6±9	3801±387	177.6±41	221.7±22

\* Combined force-generating capacity of MG, LG, and SOL estimated from the muscles' scaled volumes (Handsfield et al., 2014) and optimal fibre lengths (Arnold et al., 2010) assuming a specific tension of 225 kPa. (Spector et al., 1980; Roy et al., 1982).

†AT stiffness for the linear region of the force-length relationship measured in the isometric protocol.

‡ Slack length of the AT ( $l_{0,AT}$ ) (AT length at start of the toe region) estimated as the distance from the MG MTJ to the calcaneus at 310 ° of the crank cycle, averaged over all crank cycles.

Chapters 2, 3, and 4 analyze select portions of the data from these experiments; however, the data acquisition and analysis methodologies are largely presented in Chapter 2. All subjects gave informed consent, and protocols were approved by Institutional Review Boards at Simon Fraser University and Harvard University.

### **2.2.1. Acquisition of experimental data**

This chapter utilizes data from ten competitive female cyclists (age  $28 \pm 6$  years; Table 2-1). Each test session included a cycling protocol, during which subjects pedalled on a stationary bicycle (Indoor Trainer, SRM, Julich, Germany), and an isometric protocol, during which subjects generated ankle plantarflexion moments while secured in a custom frame. The average duration of each testing session was 3.5 hours.

During the cycling protocol, I recorded ultrasound images of the LG and MG MTJ, the 3D trajectories of 32 LED markers, reaction forces effective and ineffective (normal and radial) to the crank, and surface EMG patterns from 10 muscles (Figure 2-1; Figure 2-2). A B-mode ultrasound probe (7 MHz, 60 mm field-of-view; Echoblaster, Telemed, Vilnius, Lithuania) was secured over either the distal LG or MG MTJ on the right limb. An ultrasound gel pad (Parker Laboratories, NJ, USA) was placed at the probe-skin interface to enhance image quality and allow muscle bulging. I tracked the MTJs of both gastrocnemii in these experiments, but in this chapter I have used the MG MTJ experimental data. The position of the distal MTJ was identified as the intersection between the most distal part of the muscle and the external tendon. Markers were placed bilaterally over the greater trochanter, lateral epicondyle, lateral malleolus, calcaneus, and fifth metatarsal. Five markers were positioned on the pelvis, two were fixed on each pedal, and rigid marker triads were secured to the right thigh, shank, and ultrasound probe. Six “virtual” markers were defined based on the measured marker motions, segment lengths, and known bike dimensions; these markers located the subjects’ hip centres (Siston and Delp, 2006), lateral epicondyles, and pedal centres of pressure. Markers were tracked at 100 Hz using an optical motion capture system (Certus Optotrak, NDI, Waterloo, Canada). Ultrasound images were recorded at 40 Hz, and prior calibration (Prager et al., 1998) determined the position and orientation of the ultrasound scanning plane relative to marker triad on the probe. While pedalling, subjects wore sport sandals secured to clipless

instrumented pedals (Powerforce, Radlabor, Freiburg, Germany); the sandals had a stiff sole and allowed markers to be placed directly over bony landmarks at the calcaneus and the 5<sup>th</sup> metatarsophalangeal joint. Reaction forces at the crank were recorded bilaterally at 2000 Hz. On the left limb, bipolar Ag/AgCl surface EMG electrodes (10 mm diameter, 21 mm spacing; Norotrode; Myotronics, Kent, USA) were placed over the mid-bellies of the MG, LG, SOL, tibialis anterior (TA), and six other muscles (not reported in this thesis). I secured electrodes with stretchable adhesive bandages and tubular net bandages to reduce movement artefacts during pedalling. EMG signals were amplified (gain 1000), band-pass filtered (bandwidth 10–500 Hz; Biovision, Wehrheim, Germany), and sampled at 2000 Hz through a 16-bit data acquisition card (USB 6210, National Instruments Corp., Austin, TX).

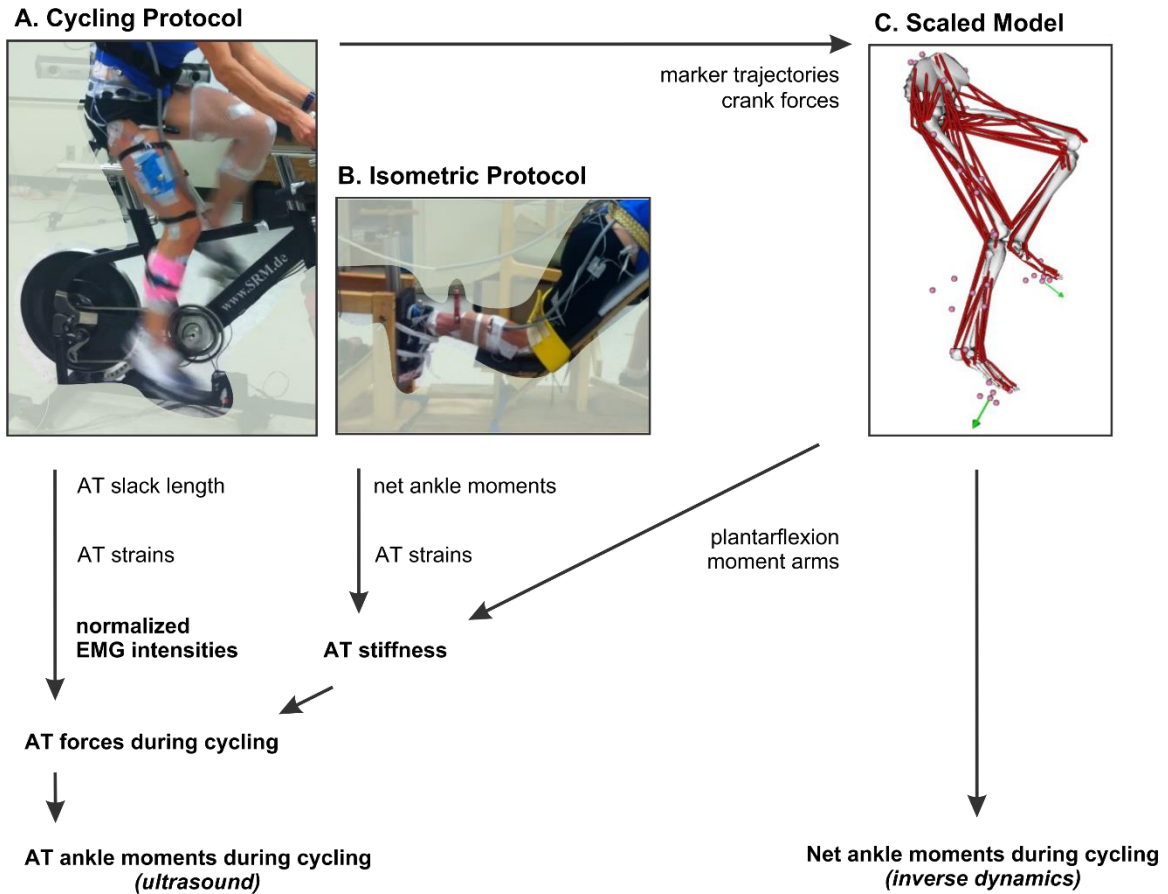


**Figure 2-1. Approach for estimating and evaluating *in vivo* Achilles tendon forces during cycling from tracked ultrasound images.**

During the cycling protocol (A), subjects pedaled on a stationary bike while I measured AT length changes, 3D marker trajectories, crank reaction forces, and surface EMG. A 3.5 V trigger from the ultrasound system was used to synchronize all data. During the isometric protocol (B), subjects generated ramped isometric plantarflexion contractions while I measured AT length changes and plantarflexion torques; these data were used to estimate AT stiffness. A musculoskeletal model (C) was scaled to each subject and was used to calculate the muscles' plantarflexion moment arms and net ankle moments during cycling. For each subject, I compared ankle moments derived from the AT forces (left) to the net ankle moments calculated via inverse dynamics (right). I examined whether the AT moments changed when I used an average stiffness, rather than the measured stiffness, or when I neglected to account for relative differences in the EMG excitations of the triceps surae muscles.

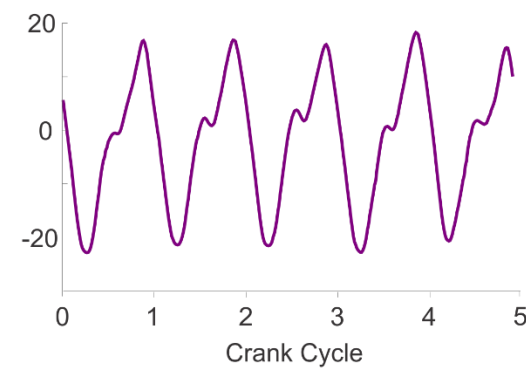
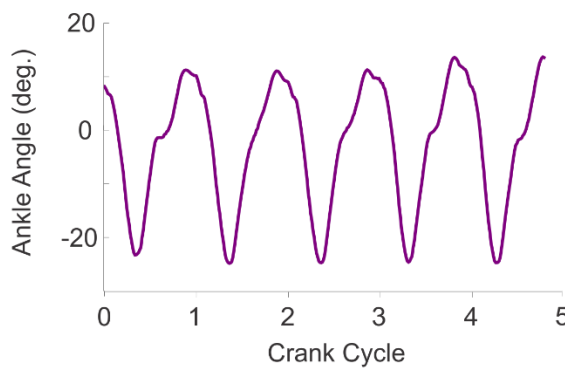
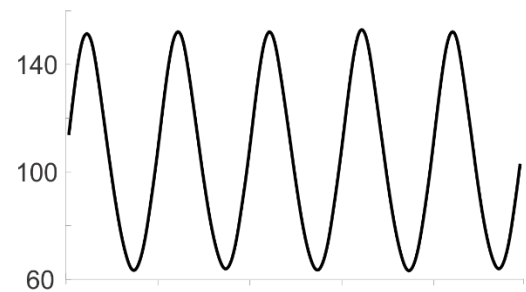
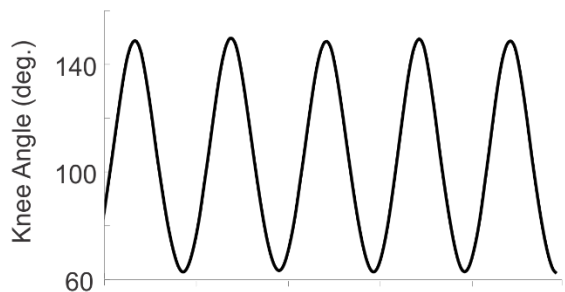
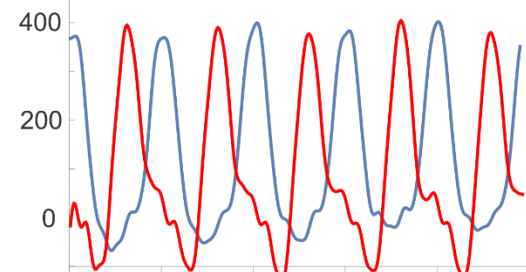
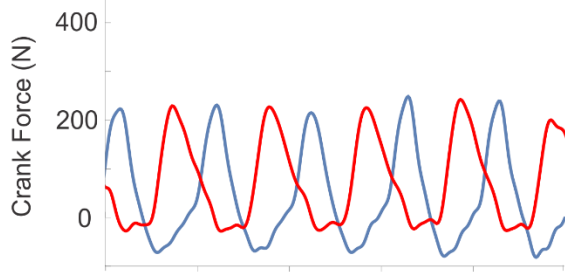
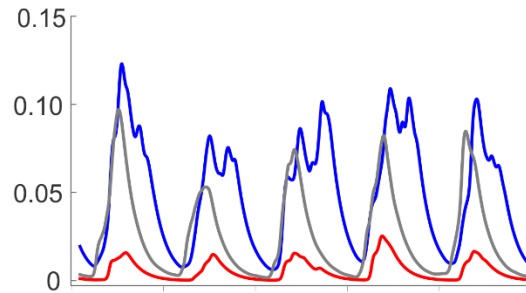
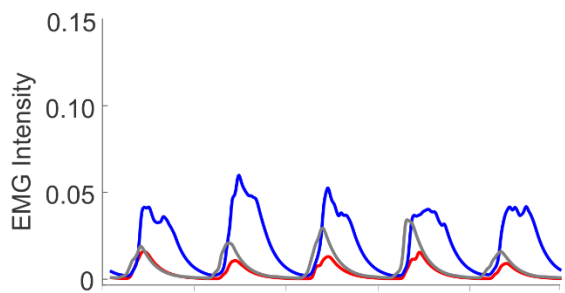
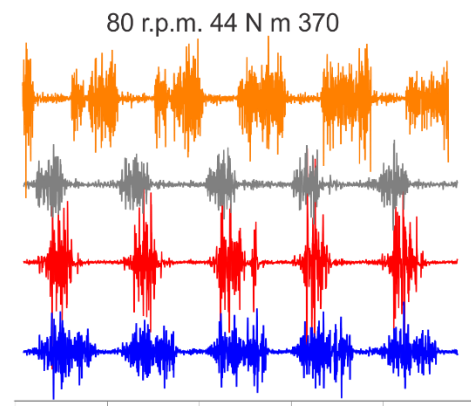
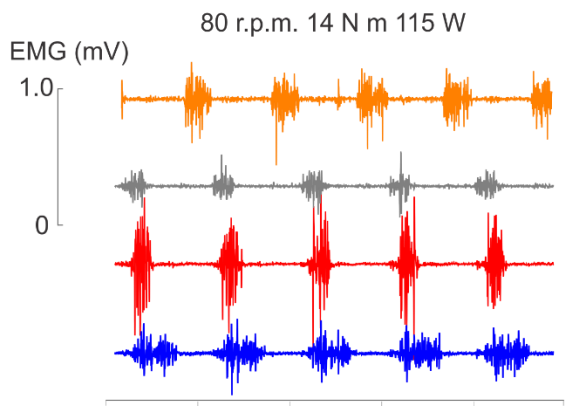


**Figure 2-2. Experimental data from a representative subject pedalling at low load and high load conditions.**

Plots show raw EMG recordings from the TA (orange), SOL (grey), MG (red), and LG (blue); normalized EMG intensities for the MG, LG, and SOL; reaction forces effective (normal, red) and ineffective (radial, blue) to the crank; knee angles (black), and ankle angles (purple) over five crank cycles at the low load (14 N m, 115 W; left) and high load (44 N m, 370 W; right) conditions. Positive angles represent knee extension and ankle dorsiflexion.

For this chapter, I analyzed trials in which subjects pedalled at 80 r.p.m. at crank loads of 14 (easy), 26, 35, and 44 N m (equivalent to a steep hill), corresponding to crank powers of 115, 220, 290, and 370 W. Sets of trials, each 15 s in duration, were repeated in random order following a 5 min warm-up. “Maximum effort” sprint trials (high power and cadence) were collected at the beginning and end of each session in an effort to elicit maximum muscle activity; I used these data as a reference when normalizing the muscles’ EMG intensities (e.g., Rouffet and Hautier, 2008). Between trials, subjects were encouraged to rest up to 30 s. I confirmed that fatigue was not a factor by comparing EMG intensities collected at the beginning and end of each session in maximum effort sprint trials, and these were within 5 % of each other. Static calibration trials were collected in cycling posture to scale a musculoskeletal model to each subject (Figure 2-1 (C)), and dynamic hip range-of-motion trials were collected to help locate subjects’ hip centres.

During the isometric protocol, subjects generated ramped plantarflexion contractions while I imaged the MG MTJ and tracked markers on the calcaneus and ultrasound probe. Each subject’s right limb was secured in a custom frame. The frame comprised a steel foot plate that secured the ankle at one of four angles (5 ° dorsiflexion, 0 °, 10 ° plantarflexion, 20 ° plantarflexion) and a support for the leg that fixed the knee at 130 ° flexion, which approximates the knee angle at 90 ° of the crank cycle when the AT transmits maximum force during cycling. The foot plate was instrumented with a strain gauge (Biovision, Wehrheim, Germany), and strain signals were recorded at 2000 Hz. Strains were converted to torque about the ankle plantarflexion axis based on measured distances between the gauge and fulcrum of the foot plate, between the fulcrum and the foot’s centre of pressure (COP), and between the COP and ankle axis ( $d_G$ ,  $d_{COP}$ , and  $d_f$  respectively, Figure 2-3). The COP was estimated from a marker at the fifth metatarsophalangeal joint, and the ankle axis was determined from each subject’s scaled

model. Subjects generated three “maximal-effort” 3 s ramped contractions at each ankle angle.

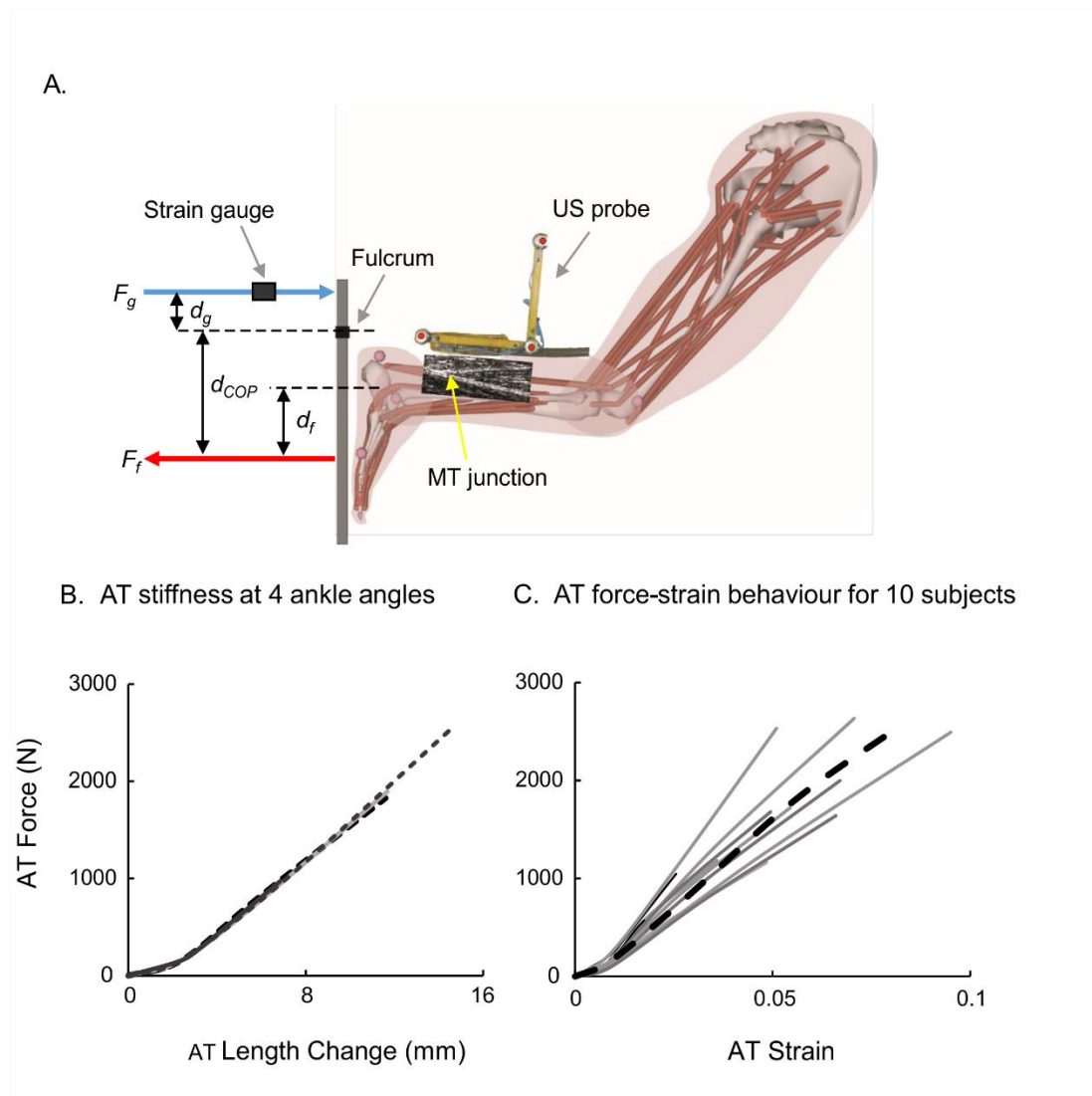


**Figure 2-3. Procedure for measuring Achilles tendon stiffness in individual subjects.**

Forces transmitted by the AT during ramped isometric contractions were estimated based on measurements of plantarflexion torque, obtained from an instrumented foot plate with known geometry (Morrison et al., 2015), and plantarflexion moment arms, calculated from a scaled musculoskeletal model (A); because other plantarflexor muscles contribute to the total plantarflexion moment, I determined the fraction of the total moment generated by the triceps surae muscles and transmitted to the AT to be 91 % based on the muscles' relative scaled volumes (Handsfield et al., 2014) and optimal fibre lengths (Arnold et al., 2010) assuming a specific tension of 225 kPa. (Spector et al., 1980; Roy et al., 1982). The corresponding AT length changes were measured from tracked ultrasound images. For each ankle angle tested, a line was fit to the linear region of the force versus length change data, and these slopes were averaged (e.g., thin dotted line) to obtain AT stiffness (B). Subjects' AT forces during cycling were determined two ways: using the measured AT stiffness, and using the group's average stiffness (thick dotted line, C). To visually make comparisons across subjects, AT length changes were converted to AT strains (shown here) by dividing by the AT slack lengths reported in Morrison et al. (2015). AT stiffness values for all subjects are provided in Table 2-1.

### **2.2.2. Determination of muscle moment arms, muscle-tendon lengths and net ankle moments**

I estimated the plantarflexion moment arms of the MG, LG, and SOL by scaling a musculoskeletal model to each subject (*OpenSim v3.3*, Delp et al., 2007). The model I used is based on existing models (Delp et al., 1990; Anderson and Pandy 1999; Arnold et al., 2010) and characterizes the geometry of the bones, the kinematics of the hip, knee, ankle, subtalar, and metatarsophalangeal joints, and the paths of the muscles (Figure 2-1 (C)). I constrained the paths of MG and LG to “wrap” over the posterior femoral condyles (Arnold et al., 2010), and I verified that the scaled models have plantarflexion moment arms that are similar to the moment arms (of other females) published in the literature (e.g., Sheehan, 2012 and Table 2-3). I used the scaled models to estimate each subject’s time-varying moment arms and MTU lengths during cycling (e.g., Figure 2-4) and during the isometric tests. I also used the models, together with the measured crank reaction forces, to calculate subjects’ net ankle moments via inverse dynamics (*OpenSim v3.3*, Delp et al., 2007). Within each model, I adjusted the mass and inertial properties of the right tibia, hind foot, and forefoot segments of the models to account for the ultrasound probe, sandals, cleats, and pedals.

**Table 2-3. Comparison of gastrocnemii moment arms in this chapter to Achilles tendon moment arms published in the literature.**

Study	Method	# Subjects	Max PF MA (cm)
Rugg et al., 1990	2D moving COR from MRI	10 M	5.0
Maganaris et al., 1998b	2D moving COR from MRI	6 M	5.5
Lee and Piazza, 2009	tendon excursion from ultrasound images	12 M	4.2
Hashizume et al., 2012	3D COR from MRI	15 M	4.1
Sheehan et al., 2012	3D COR from cine-PC MRI	14 M	5.5 (M)
		6 F	4.7 (F)
Current Study†	scaled model	10 F	4.6±0.12 (MG)
			4.8±0.12 (LG)

†Maximum plantarflexion moment arms of MG and LG during cycling estimated from each subject's scaled musculoskeletal model (Arnold et. al., 2010) and averaged across the 10 female subjects; moment arms of SOL were greater than those of MG and less than those of LG.

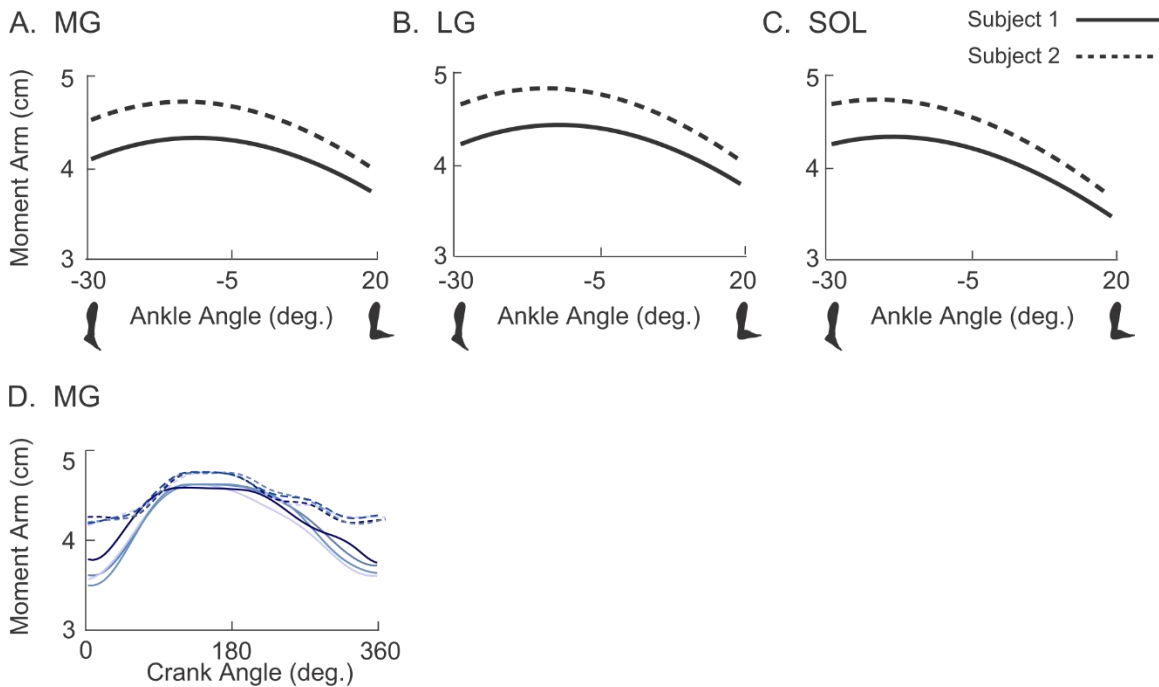


**Figure 2-4. Plantarflexion moment arms during cycling.**

Plantarflexion moment arms of the MG plotted versus ankle angle (A) and crank angle (D), as estimated from scaled musculoskeletal models of the subjects with the shortest (Subject 1) and longest (Subject 2) moment arms in this study. Moment arms of the LG (B) and SOL (C) versus ankle angle are also shown. Moment arms during cycling are averaged for 2 subjects across 10 crank cycles at 4 crank loads and do not vary with load (D). The muscles' peak moment arms during cycling, averaged across all subjects and loads, were  $4.6 \pm 0.12$  cm for MG,  $4.8 \pm 0.12$  cm for LG, and  $4.7 \pm 0.13$  cm for SOL.

### 2.2.3. Characterization of subject-specific Achilles tendon force-length properties

I used AT forces and length changes from the isometric tests to generate a tendon force-length curve for each subject (Figure 2-3). I assumed that a fraction of the plantarflexion torques measured during the isometric tests were generated by MG, LG, and SOL. To estimate this fraction, I determined the relative volumes of all the plantarflexors (MG, LG, SOL, flexor digitorum longus, flexor hallucis longus, peroneus brevis, peroneus longus, tibialis posterior) from regression equations (Handsfield et al., 2014), and I used each muscle's volume, together with its optimal fibre length (from each scaled musculoskeletal model), to estimate the maximum isometric moment-generating capacity of all plantarflexors at joint angles corresponding to the isometric tests. The combined moment-generating capacity of MG, LG, and SOL was 91 % of the total moment and was generally consistent across joint angles and subjects (Figure 2-5). At each ankle

angle tested, I calculated an “effective” plantarflexion moment arm of the AT (e.g., Biewener, 1989) by averaging the moment arms of MG, LG, and SOL weighted by their physiological cross-sectional areas (PCSAs) as determined from regression equations (Handsfield et al., 2014) and optimal fibre lengths from a scaled musculoskeletal model (Arnold et al., 2010). To generate each subject’s AT force-length curve, I estimated each subject’s AT forces from the moment arms and from 91 % of the measured plantarflexion torques, and I determined the corresponding AT lengths from the ultrasound data. Ultrasound images from the distal MTJ were used together with the position of the calcaneus marker to determine AT lengths. I corrected for marker height and skin thickness to estimate the AT insertion point on the calcaneus. AT length was determined as the Euclidean distance from the AT insertion to the digitized distal MG MTJ. AT length changes and strains were determined relative to the tendon’s assumed slack length. The AT slack length  $l_{0,AT}$  was estimated from cycling data, for each subject, as the AT length measured at 310 ° of the crank cycle, averaged over all crank cycles. This choice was motivated by *in vivo* tendon buckle data (Gregor et al., 1987) that showed AT force beginning to rise near 310 ° across pedalling conditions. These slack lengths are different than those reported previously (Morrison et al., 2015) and I believe this is related to differences in the assumed centre of pressure of the foot (where the force was applied in the isometric frame) between the two studies. The peak AT strains measured during the maximal effort isometric contractions (Figure 2-3 (C)) are within the range reported for isometric contractions in previous studies (5–10 %; Muramatsu et al., 2001; Maganaris and Paul, 2002; Lichtwark and Wilson, 2005a)

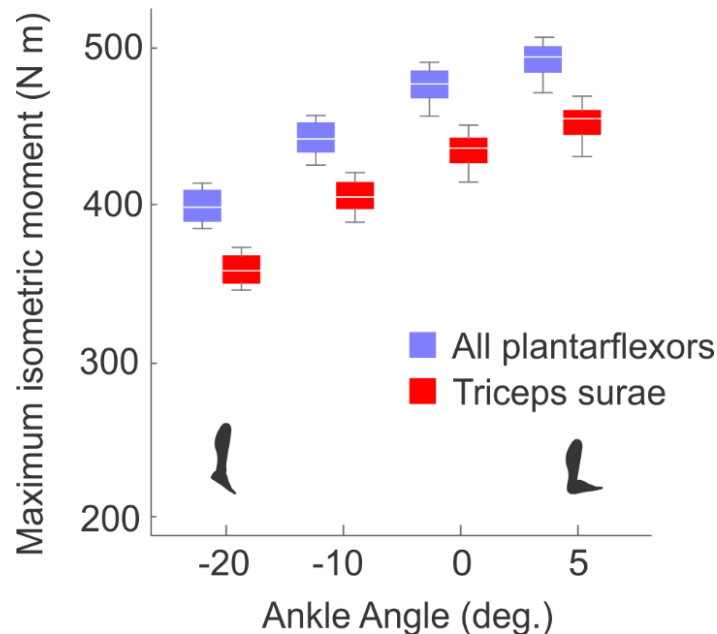


**Figure 2-5. Comparison of maximum isometric plantarflexion moments generated by all plantarflexors versus the triceps surae muscles.**

Maximum isometric plantarflexion moments generated by all plantarflexors crossing the ankle (blue) and by the three triceps surae muscles (red) at the knee and ankle angles corresponding to the isometric tests. Moments are shown as box and whisker plots (median, interquartile range, range) for 10 subjects. Each muscle's moment-generating capacity was estimated based on its volume, as calculated from regression equations published by Handsfield et al. (2014), and on its optimal fibre length and moment arms, as estimated from scaling the lower extremity model published by Arnold et al. (2010), assuming a specific tension of 225 kPa (Spector et al., 1980; Roy et al., 1982). The combined, maximum isometric force-generating capacity of the MG, LG, and SOL relative to all plantarflexors was approximately 91 % and was consistent across joint angles and subjects.

The measured AT force-length curves included a linear region and a toe region (Figure 2-4 (B/C)). I characterized the linear stiffness of each subject's AT by fitting a line to the linear region as force was rising (Figure 2-3 (B)). The linear stiffness did not vary with ankle angle, so I averaged values from the four angles to obtain an AT stiffness ( $k_{SEE}$ ) for each subject. Across subjects, AT stiffness differed significantly (ANCOVA,  $p < 0.05$ , Figure 2-3 (C)) consistent with previous findings (Kubo et al., 2003; Lichtwark and Wilson, 2005a; Muraoka et al., 2005; Morrison et al., 2015). Within the toe region, the subjects' force-length properties could not always be resolved due to the rapid rise in force during the ramped isometric contractions and the relatively low rate of ultrasound image acquisition. However, the toe region stiffness was generally consistent across the four subjects for whom I could resolve these data (Table 2-1). For this reason, and because

strains within the toe region were small (on average 1.01 %) compared to peak strains during cycling (3-6 %), I averaged the force-length data within the toe region from four subjects to obtain an average toe region stiffness of 40 N mm<sup>-1</sup> ( $k_{SEE,T}$ ) that I used for all subjects.

#### 2.2.4. Estimation of Achilles tendon lengths and forces during cycling

Ultrasound images from the distal MTJ were used together with the position of the calcaneus marker to estimate time-varying AT lengths. To characterize the AT insertion on the calcaneus as accurately as possible, I corrected the 3D coordinates of the calcaneus marker for marker height by determining the vector distance (height of LED marker measured using calipers) and direction (using the angle of the foot relative to the shank). AT length  $l_{AT}$  was determined as the Euclidean distance from the 3D coordinates of the AT insertion to the digitized distal MG MTJ.

AT forces ( $F_{AT}$ ) during cycling were estimated from ultrasound-based measures of AT length ( $l_{AT}$ ) using the values of AT stiffness in the toe ( $k_{SEE,T}$ ) and linear regions ( $k_{SEE}$ ) and slack length ( $l_{0,AT}$ ) obtained for each subject:

$$F_{AT} = \begin{cases} 0, & l_{AT} \leq l_{0,AT} \\ k_{SEE,T}(l_{AT} - l_{0,AT}), & l_{0,AT} < l_{AT} \leq (l_{0,AT})1.0103 \\ k_{SEE}(l_{AT} - (l_{0,AT})1.0103) + k_{SEE,T}(l_{0,AT}(0.0103)), & (l_{0,AT})1.0103 < l_{AT} \end{cases} \quad (\text{Eq. 2-1})$$

AT stiffness was characterized based on length changes measured at the MG MTJ during ramped isometric contractions (Table 2-1). The slack length ( $l_{0,AT}$ ) at the start of the toe region was estimated from the cycling data as the AT length measured at 310 ° of the crank cycle, averaged over all crank cycles (Gregor et al., 1987). The AT length at the start of the linear region ( $(l_{0,AT})1.0103$ ) was determined based on the average AT strain measured for the 4 subjects for whom I could resolve a toe region during the isometric tests.

During the maximum-effort isometric tests, from which we determined the AT mechanical properties, the MG, LG, and SOL were likely fully active (although we did not record EMG to confirm this). However during cycling, the relative EMG intensities of MG,

LG, and SOL – and thus the muscles’ relative contributions to AT force – vary with load (Wakeling and Horn, 2009). To obtain a more representative estimate of the total force transmitted by the AT during cycling, I scaled the estimated forces by a scale factor,  $c_e$ . This factor essentially divides the measured tendon length change by the relative EMG excitation of the MG,  $\hat{e}_{MG}$ , weighted by the fractional PCSAs,  $\hat{A}_{PCSA}$ , of the MG, LG, and SOL:

$$c_e = \frac{((\hat{e}_{MG}\hat{A}_{PCSA,MG})+(\hat{e}_{LG}\hat{A}_{PCSA,LG})+(\hat{e}_{SOL}\hat{A}_{PCSA,SOL}))}{\hat{e}_{MG}} \quad (\text{Eq. 2-2})$$

The fractional PCSA of each muscle was calculated as the ratio of its PCSA to the summed PCSAs of the MG, LG, and SOL, which I determined from regression equations (Handsfield et al., 2014) and optimal fibre lengths (Arnold et al., 2010) assuming a specific tension of 225 kPa (Spector et al., 1980; Roy et al., 1982).

For the purposes of this chapter, the EMG signals were quantified by their intensities across a 10 to 450 Hz frequency band using an EMG-specific wavelet analysis (von Tscherner, 2000). My techniques for processing the EMG signals are described in more detail within Chapters 3 and 4. EMG intensities were normalized, for each muscle, by the maximum intensity detected during the reference cycling trials. Because intensity is a close approximation to the power of the signal (von Tscherner, 2000) and because muscle force is linearly related to the EMG signal’s amplitude, not its power (Milner-Brown and Stein, 1975), I calculated the square root of the mean EMG intensity as a measure of excitation for each muscle ( $\hat{e}_{MG}$ ,  $\hat{e}_{LG}$ ,  $\hat{e}_{SOL}$ ) within each trial (Eq. 2-2). I assumed that the relative EMG intensities of the muscles during these “maximal effort” trials were similar to their intensities during the “maximal effort” isometric tests, and I assumed that EMG excitation recorded on the left limb was representative of excitation on the right limb shifted by 180 ° of the crank cycle.

### 2.2.5. Evaluation of the ultrasound-based method

I evaluated this procedure for estimating AT force in four ways. First, I examined whether subjects’ AT forces increased with crank load as reported by Gregor et al. (1987), who analyzed *in vivo* tendon force buckle data from one subject (Gregor et al., 1987). I

used a general linear model ANOVA (*JMP* Software, SAS, Cary, USA), and I tested for the effects of load (covariate) and subject (random factor) on peak AT strain and force.

Second, I compared each subject's AT plantarflexion moments, calculated from the estimated AT forces and moment arms during cycling, to the same subject's net ankle moments calculated using traditional inverse dynamics (Figure 2-1). In particular, I tested whether differences in these moments increased when I used the group's average AT stiffness,  $\bar{k}_{SEE}$  (165 N mm<sup>-1</sup> in the linear region) in Eq. 2-1, rather than the subject's measured AT stiffness,  $k_{SEE}$ , or when I did not account for measured changes in the muscles' relative EMG intensities with load. To formalize these comparisons, I classified the subjects in 2 x 2 contingency tables and used Fisher's Exact Test. Subjects were classified based on whether their peak AT moments from ultrasound were (or were not) within 91±10 % of their peak moments from inverse dynamics; this criterion assumes that the MG, LG, and SOL generated about 91 % of the plantarflexion moment, and the dorsiflexors were inactive (as evidenced by EMG recordings, Figure 2-2), during the downstroke.

Third, I varied each subject's AT slack length by ±1 % and AT stiffness by ±20 % and re-calculated AT force for all cycling trials. This sensitivity analysis quantified how the onset and magnitude of the estimated AT forces might have been affected by errors in my subject-specific, ultrasound-based values.

Fourth, to test the implications of my chosen toe region properties and to check the values of slack length for the linear region of the AT force-length curve (Table 2-1) I compared AT slack lengths estimated at 310 ° of the crank cycle to AT slack lengths estimated, alternatively, by plotting AT forces derived from each subject's net ankle moments (from inverse dynamics) versus the subject's AT lengths measured using ultrasound during cycling. Specifically I plotted the ultrasound-derived AT length (x-axis) *versus* the AT force derived from inverse dynamics net ankle moment (y-axis) (calculated using 91 % of inverse dynamics plantarflexion moment and the time-varying AT moment arm determined from the scaled models) averaged across 10 pedal cycles. I created these AT force-length plots for the portion of the pedal cycle when the AT was lengthening for each subject at the 4 pedalling conditions separately, similar to the methods used to

determine AT stiffness at the 4 ankle angles in the isometric protocol. With these data, I fit a piece-wise function with two linear portions, one to define the toe region and the other to define the linear region of the force-length curve for each trial (Figure 2-6). I determined the transition point from the toe region to the linear region using the following criterion: if AT force was  $\leq 120$  N, the data point was included in the toe region, if AT force was  $>120$  N, the data point was included in the linear region. This value was based on the average peak AT force estimated in the toe region during the isometric protocol for the 4 subjects for whom toe-region properties were reported.

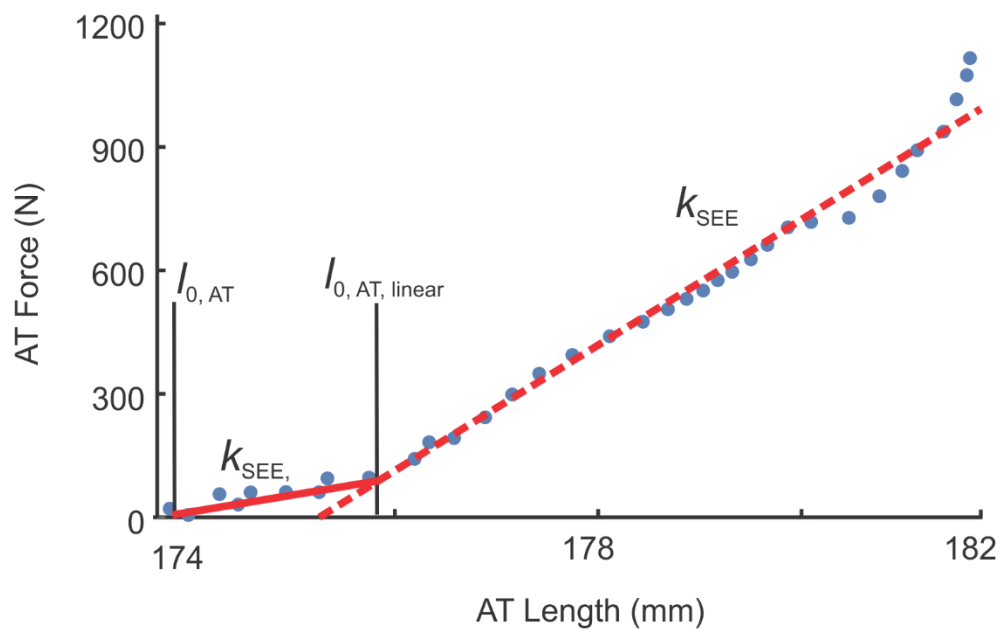


**Figure 2-6. Achilles tendon (AT) force-length curve derived from inverse dynamics estimated AT forces and ultrasound measured AT length changes for one subject.**

Forces transmitted by the AT, while lengthening during cycling, were estimated from each subject's inverse dynamics ankle moments and time-varying AT moment arm, assuming the fraction of the net moment transmitted by the AT to be 91 %. AT lengths were measured as the distance between the MG muscle-tendon junction, determined using B-mode ultrasound, and a calcaneus marker. For each condition and subject, a piece-wise function with two linear portions was fit, one defining the toe region (red solid line) and the other defining the linear region (red dashed line) of the force-length curve. The slopes of each line were determined to be toe region stiffness ( $k_{SEE,T}$ ) and linear region stiffness ( $k_{SEE}$ ). AT lengths at the beginning of the toe region ( $l_{0,AT,toe}$ ) and the linear region ( $l_{0,AT,linear}$ ) were determined.

This method provided an inverse dynamics estimated AT length at the beginning of the toe region ( $l_{0,AT,toe}$ ) and the linear region ( $l_{0,AT,linear}$ ), which I compared to the values

estimated using  $310^\circ$  as the position, corresponding to AT slack length  $l_{0,AT}$  (reported in Table 2-1).

Note that throughout my thesis, AT slack length refers to the AT length estimated at  $310^\circ$  of the crank cycle, which corresponds to the beginning of the toe region. A general linear model ANOVA was conducted to determine if there were differences in the estimated AT slack lengths at (i) the beginning of the toe region and (ii) at the beginning of the linear region (dependent variable) between the two methodologies. These values are reported in Table 2-1 and results are provided within the Discussion.

## 2.3. Results

Ultrasound images of the MG MTJ during cycling confirmed that the AT starts stretching during the upstroke (Figure 2-7 (A)). In the subjects tested here, the AT transmitted force between  $315^\circ \pm 5^\circ$  and  $260^\circ \pm 10^\circ$  of the crank cycle, reaching maximum force at  $100^\circ \pm 15^\circ$  of the crank cycle. The start of force transmission was identified as the crank angle where AT force  $> 0$  N. Peak AT strains occurred during the downstroke and increased with load in all subjects ( $p < 0.05$ ). On average, peak strains were 3 % (range: 2-4.7 %) at the lowest load and more than 5 % (range: 4-7.3 %) at the highest load (Figure 2-7 (B)). By contrast, subjects' knee and ankle angles and associated MTU lengths were highly constrained across loads (Figure 2-8).

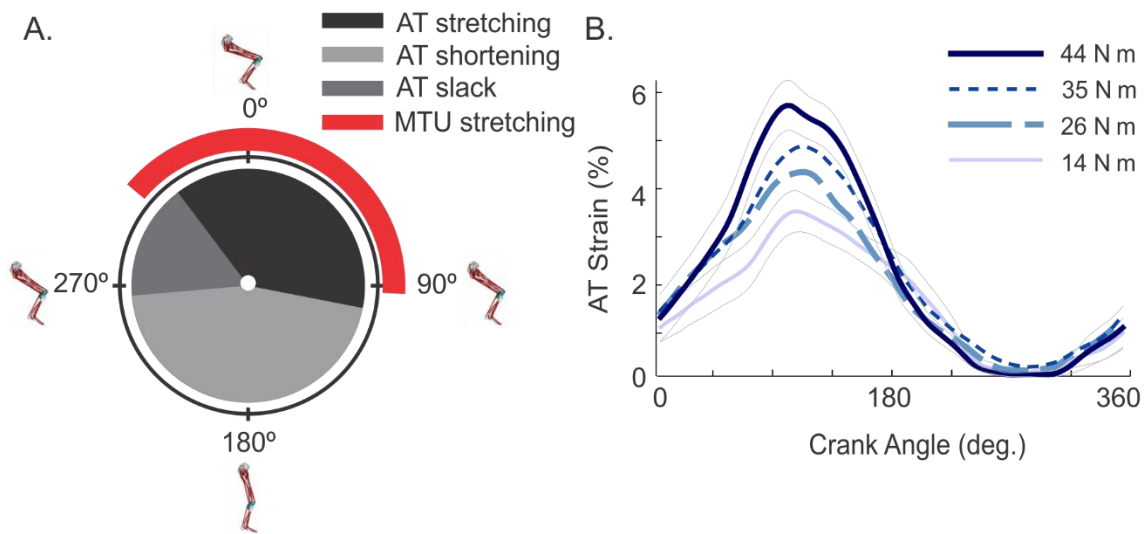


**Figure 2-7. Achilles tendon strains during cycling at 80 r.p.m.**

Variation in AT strain during the crank cycle (A) and across 4 crank loads (B). The tendon stretches from 315° to 100° of the crank cycle (black), shortens through 180° (light grey), and shortens below its slack length at 215° (dark grey). Time-varying AT strains during cycling (B) are presented as mean  $\pm$  SE for 10 subjects at 4 crank loads, corresponding to crank powers of 115, 220, 290, and 370 W. Thin grey curves represent the SE and are shown for the low and high loads; SE values were similar across all loads.

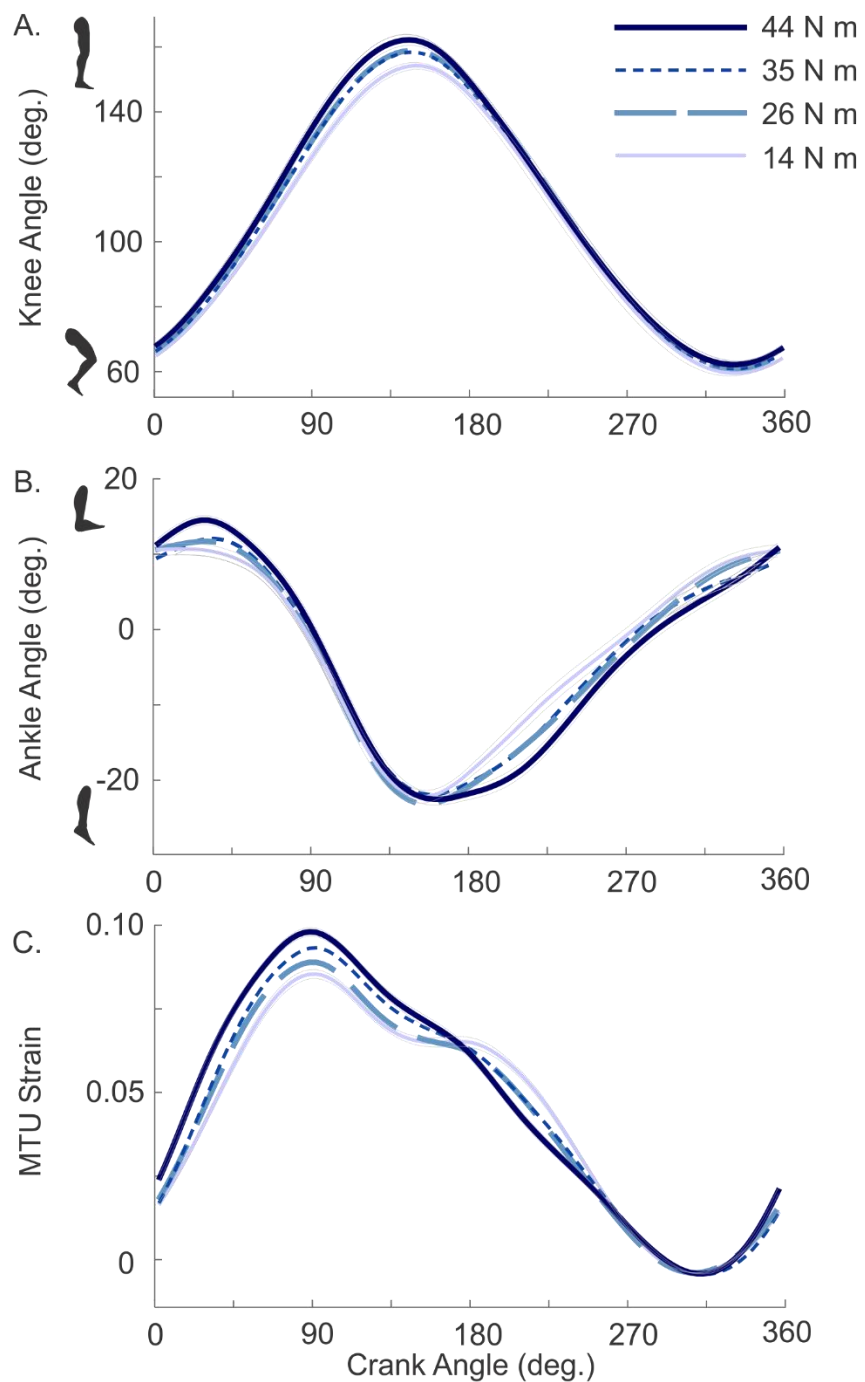


**Figure 2-8. Kinematics and associated muscle-tendon unit strains during cycling at 80 r.p.m.**

Knee angles (A), ankle angles (B), and muscle-tendon unit strains (C) of the medial gastrocnemius (MG MTU) during cycling at 80 r.p.m. at 4 different crank loads. MG MTU length changes were measured relative to the length at 310 ° of the crank cycle. Each curve shows average data for 10 subjects. Thin grey curves represent the SE and are shown for the low and high loads; SE values were similar across all loads.

Subjects' estimated AT forces (Figure 2-9) and the normalized EMG intensities of the MG, LG, and SOL (Figure 2-10) also increased with load ( $p < 0.05$ ). These trends are consistent with the previous tendon buckle study by Gregor et al. (1991) and with EMG data published in the literature (e.g., Ericson et al., 1984; Baum and Li, 2003; Wakeling and Horn, 2009). Subjects' peak AT forces during cycling averaged 920 N (range: 410-1225 N) at the lowest load and 1510 N (range: 650-2180 N) at the highest load (Figure 2-9). At the highest load (44 N m, 370 W), the peak forces represented 30 to 50 % of the combined MG, LG, and SOL muscles' maximum isometric force-generating capacity. These percentages are based on the muscles' scaled volumes (Handsfield et al., 2014) and optimal fibre lengths (Arnold et al., 2010), assuming a specific tension of 225 kPa (Spector et al., 1980; Roy et al., 1982). Increases in the EMG excitations of MG, LG, and SOL across conditions were generally consistent with the timing of increases in AT force. By contrast, the TA was not active during the downstroke (Figure 2-2);

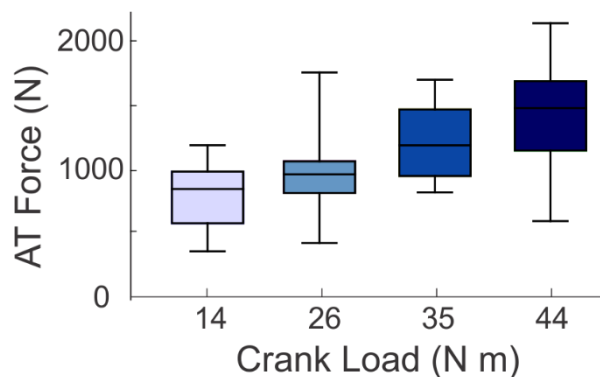


**Figure 2-9. Increase in AT force with crank load.**

Peak AT forces are shown as box and whisker plots (median, interquartile range, range) for 10 subjects cycling at 80 r.p.m. at 4 crank loads, corresponding to crank powers of 115, 220, 290, and 370 W.

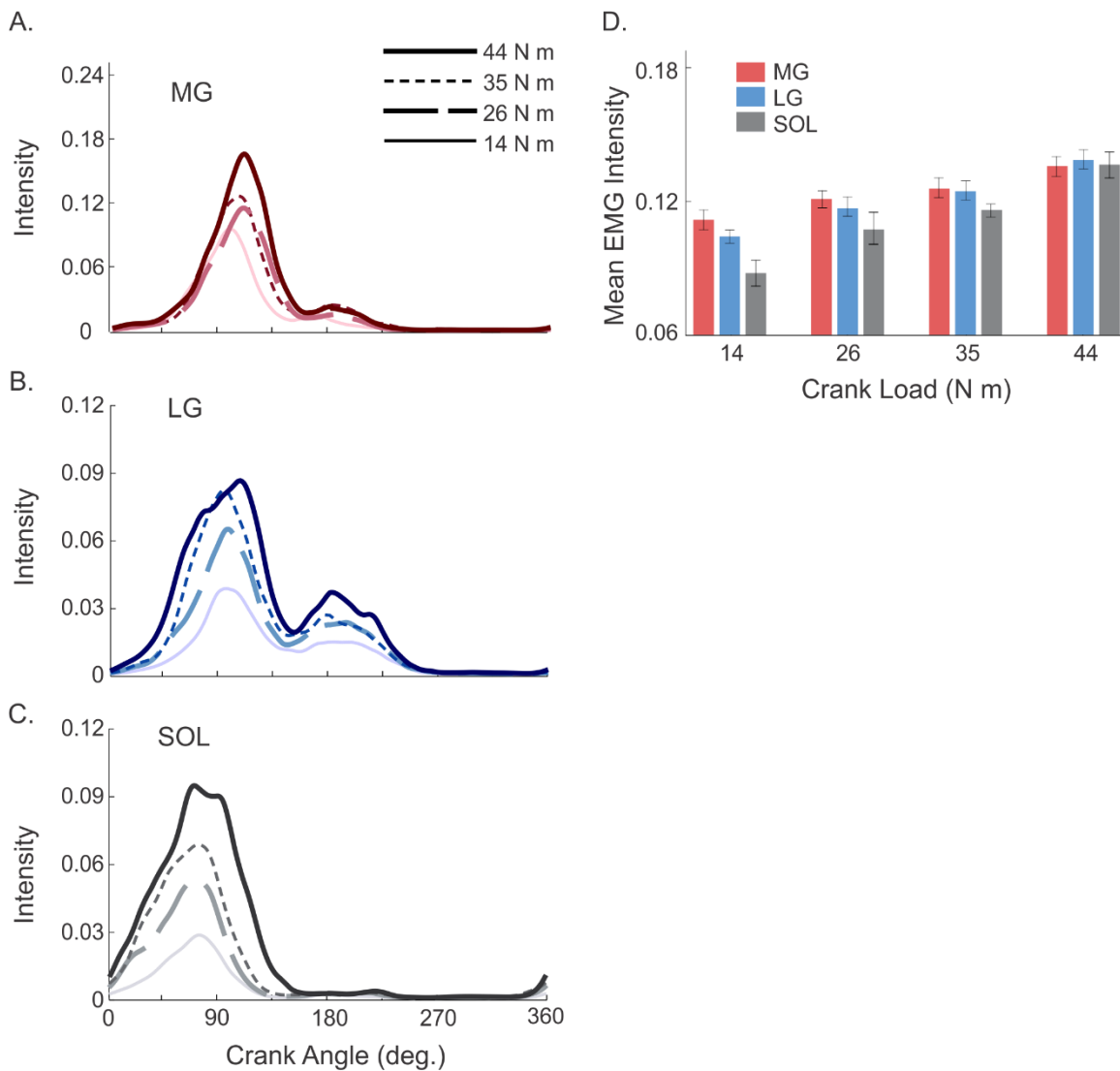


**Figure 2-10. Electromyographic signals during cycling at 80 r.p.m.**

Normalized EMG intensities of the medial gastrocnemius (MG, A), lateral gastrocnemius (LG, B), and soleus (SOL, C) during cycling at 80 r.p.m. at 4 different loads, averaged across 10 subjects. Thin grey curves represent the SE and are shown for the low and high loads; SE values were similar across all loads. Relative intensities of MG, LG, and SOL during cycling vary with load (D). EMG intensity is normalized to muscle-specific maximum values collected during “maximum effort” reference cycling trials. Bars represent mean  $\pm$  SE.

Plantarflexion moments, derived from the estimated AT forces, reproduced the temporal patterns of each subject’s net ankle moments calculated from inverse dynamics (Figure 2-11; Figure 2-12). Subjects’ peak AT moments were less than their net ankle moments in most cases; on average, the ultrasound-based moments were 12 % less at the lowest load and 5 % less at the highest load during the downstroke.

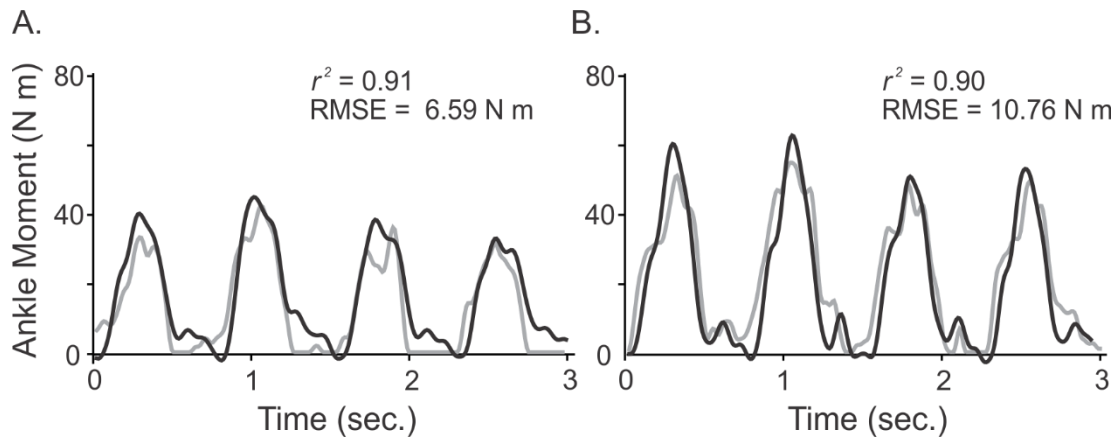


**Figure 2-11. Comparison of time-varying *in vivo* Achilles tendon moment and inverse dynamics net ankle moment.**

AT plantarflexion moments (from ultrasound-based measures of AT strains, grey) and net ankle moments (from inverse dynamics, black) for a representative subject pedalling at 80 r.p.m. at crank loads of 26 N m (220 W, A) and 44 N m (370 W, B).  $r^2$  values were calculated using correlation.

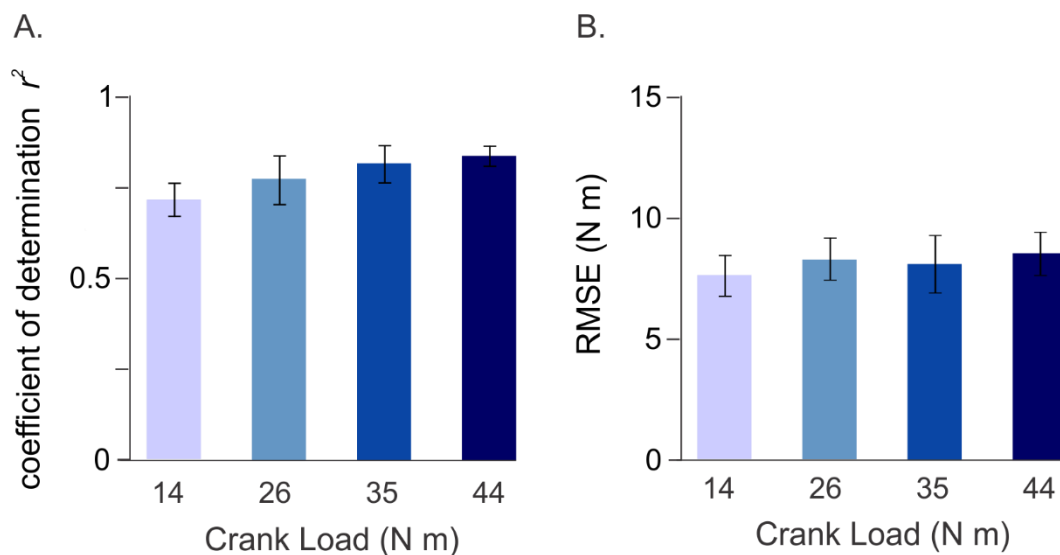


**Figure 2-12. Comparison of ultrasound-based moments to inverse dynamics moments across cycling loads.**

Coefficient of determination  $r^2$  (A) and the root-mean square error (RMSE) (B) between AT ankle moments (from ultrasound-based measures of AT strains) and net ankle moments (from inverse dynamics) at four crank loads. Bars show the mean  $\pm$  SE for 10 subjects.

Differences between subjects' ultrasound-based AT moments and net moments increased substantially when I did not account for changes in the muscles' relative EMG intensities with load (i.e., when I neglected scale factor  $c_e$ ) or, for some subjects, when I used an average AT stiffness,  $\bar{k}_{SEE}$ , rather than the subject's measured value,  $k_{SEE}$  (Figure 2-13). Three subjects, for example, had tendons that were substantially more compliant than the average (i.e.,  $k_{SEE} < \bar{k}_{SEE}$  by 15 N mm<sup>-1</sup> or more). In these cases, using the average stiffness in Eq. 2-1 overestimated AT force (Figure 2-13). All ten subjects showed variations in the muscles' EMG patterns at the different crank loads (Figure 2-10). Typically, the normalized EMG intensities of the three plantarflexors were similar at the high load, but the intensity of SOL was proportionally decreased at the low load. When I did not account for these changes, my procedure overestimated AT force, especially at the low loads (Figure 2-13).

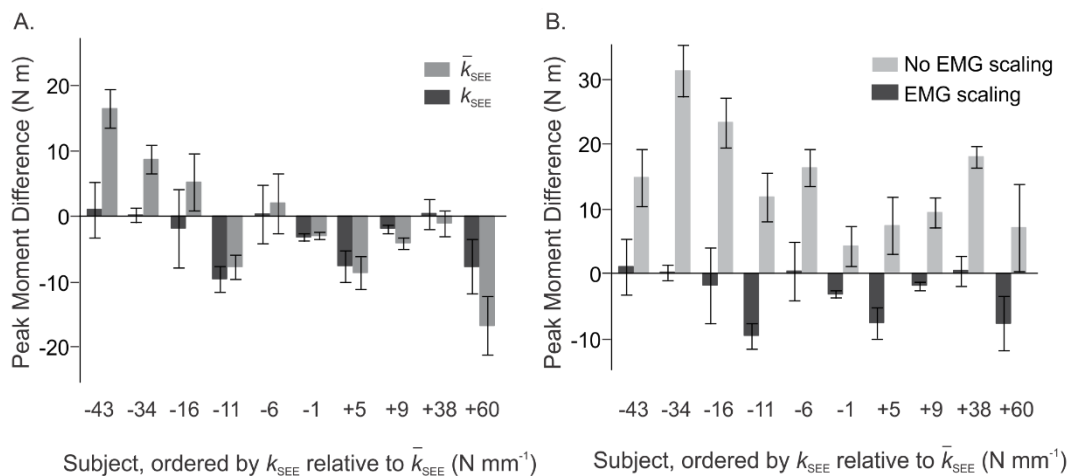


**Figure 2-13. Effects of two methodological refinements on estimated Achilles tendon ankle moments.**

Accounting for subject-specific variations in AT stiffness (A) and accounting for relative changes in the EMG intensities of MG, LG, and SOL (B). Each pair of bars shows the difference between the peak AT moment (from ultrasound) and the peak net ankle moment (from inverse dynamics) for a single subject during cycling, averaged across four loads (mean  $\pm$  SE). A negative value indicates that the ultrasound-based moment was less than the net moment (as expected if plantarflexors in addition to MG, LG, and SOL were active during the downstroke). Subjects are ordered by their estimated AT stiffness ( $k_{SEE}$ ) relative to the group's average AT stiffness ( $\bar{k}_{SEE}$ ); subjects with negative values had more compliant tendons than the average, and subjects with positive values had stiffer tendons than the average. When subject-specific stiffness, together with an EMG scale factor that accounted for the muscles' relative EMG intensities, was used to estimate AT moment (black bars), the resulting estimates were usually better than when moments were calculated using the group's average stiffness ( $\bar{k}_{SEE}$ , dark grey bars, A) or when moments were calculated without accounting for the muscles' relative EMG intensities (light grey bars, B).

## 2.4. Discussion

In this chapter, I presented and evaluated a procedure for estimating *in vivo* AT forces from ultrasound images. Comprehensive data sets from ten female elite cyclists were used to test two approaches: (i) accounting for subject-specific AT stiffness and (ii) accounting for changes in the relative EMG intensities of the MG, LG, and SOL. This analysis showed that length changes of the AT, determined from tracking the MG MTJ, can provide estimates of subjects' AT forces and moments across the pedal cycle that are consistent with the subjects' net ankle moments calculated from inverse dynamics– but only when the muscles' relative EMG intensities are considered. Other investigators have speculated that the muscles' activity should be considered (e.g., Gregor et al., 1991; Farris and Sawicki, 2012). For example, Gregor (1991) highlights that considering PCSA alone when estimating individual muscle forces from total AT force assumes that all muscles are either maximally active or active in some proportion to their PCSA, however we know this is not the case (Wakeling et al., 2006; Wakeling and Horn, 2009). My study provides new evidence that indeed considering each individual muscle's activity (as well as PCSA) is critical when estimating total AT force from length changes measured only at the MG MTJ.

Rigorous evaluation of the estimated AT forces is challenging. Here, I used subjects' net ankle moments from inverse dynamics as a check, and I assumed that the triceps surae could contribute, at most, 91 % of the plantarflexion moment. In 9 of 10 subjects, across all load conditions, the peak AT moments – estimated from Eq. 2-1 and each subject's scaled model – were within  $91 \pm 10$  % of the peak moment calculated from inverse dynamics. Fewer subjects met this criterion when I used an average AT stiffness to estimate AT force (4 of 10 subjects,  $p < 0.01$ , Figure 2-13), and even fewer subjects met this criterion when I neglected the relative muscle excitations using scale factor  $c_e$  (1 of 10 subjects,  $p < 0.01$ , Figure 2-13).

Even with these refinements, the ultrasound-based AT moments for four subjects were equal to or greater than the inverse dynamics-based moments. It is likely that AT forces were overestimated in these cases, and there are several possible explanations. First, co-contraction of the TA or other dorsiflexors may have decreased the net moment calculated from inverse dynamics. The EMG data show that the TA was active from

approximately 260 ° to 360 ° of the crank cycle, and this may explain a portion of the discrepancy near top dead centre (0 ° of the crank cycle) when AT force was rising, particularly at the highest load (Figure 2-11). However, the TA was not active during the downstroke, and our subjects' net ankle moments were within ranges reported in the literature for comparable cadences and loads (Gregor et al., 1985; Hull and Jorge, 1985; Smak et al., 1999).

Second, I may have overestimated the effective moment arm of the AT the ankle. I scaled a generic model to each subject based on markers at the lateral malleolus and calcaneus, and these markers tracked well during cycling. However, I did not directly measure subjects' AT moment arms. If I overestimated subjects' moment arms, then my estimates of AT force may be better than my estimates of AT moments. Lee and Piazza (2009) have shown that sprinters, on average, possess AT moment arms that are 25 % shorter than height matched non-sprinters. Given that our subjects were elite cyclists, it is possible that we overestimated moment arms using the generic *OpenSim* model that we scaled to our individual subjects.

Third, I may have overestimated AT stiffness during the isometric tests if muscles other than MG, LG, or SOL made substantial contributions to the measured plantarflexion torque (i.e., more than 9 %), or if I overestimated the distance between the ankle's axis of rotation and the foot's centre of pressure ( $d_f$  in Figure 2-3 (A)). I did not record EMG data during the isometric tests, nor did I precisely measure the foot's centre of pressure, so I cannot assess these explanations. However, the average AT stiffness that I measured (165 N mm<sup>-1</sup>) is between values commonly cited in the literature (150 to 190 N mm<sup>-1</sup>, Maganaris and Paul, 2002; Lichtwark and Wilson, 2005a). To gain additional insight, I performed a sensitivity study. Changing AT stiffness by ±10 % altered the estimated AT force by ±10 % of the muscles' maximum isometric force (Figure 2-14 (B)); thus, subject-specific errors in AT stiffness could explain the discrepancies observed.

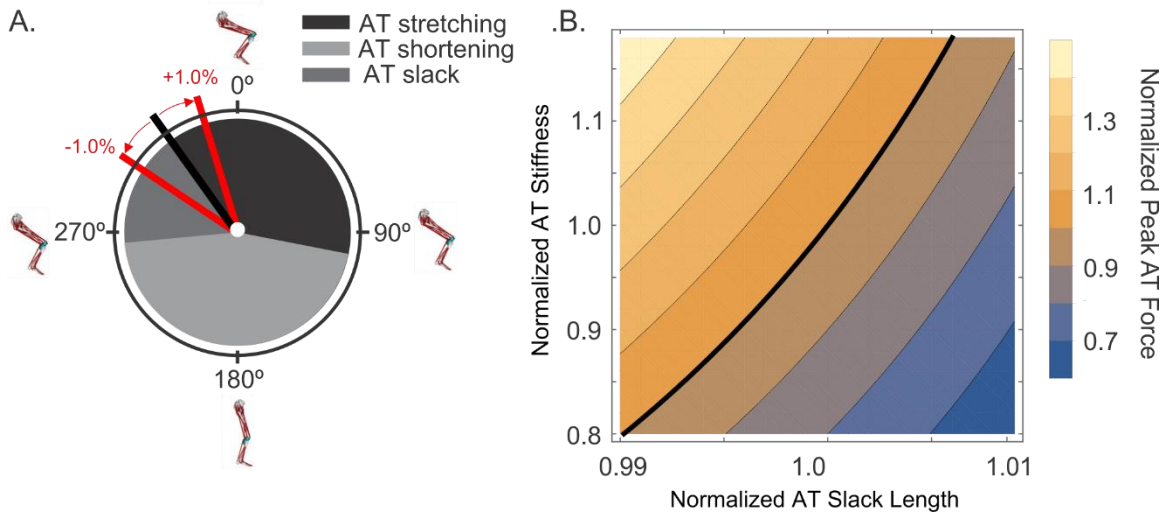


**Figure 2-14. Sensitivity analysis of Achilles tendon forces.** Sensitivity of ultrasound-based AT forces to changes in slack length (A, B) and stiffness (B). Schematic shows how the timing of AT force onset changes during the crank cycle, on average, with a  $\pm 1\%$  change in slack length (A). Contour plot shows how the AT force magnitude changes, on average, with a  $\pm 1\%$  change in slack length and a  $\pm 20\%$  change in stiffness (B). Changes in force were normalized to the peak AT force for each subject at each load.

Fourth, I may have underestimated AT slack length. In the sensitivity study, small increases in slack length at the beginning of the toe region (i.e., 1%) substantially delayed the onset of AT force (i.e.,  $+30^\circ$ ) during the upstroke (Figure 2-14 (A)). Given that the AT began to transmit force at  $315^\circ \pm 5^\circ$  of the crank cycle, when averaged across subjects and conditions, it is possible that we underestimated slack lengths when taking the average tendon length at  $310^\circ$  across pedal cycles based on the observations from Gregor et al. (1987). However, when using these slack lengths the timing of the subjects' estimated AT moments at force onset was generally consistent with the timing of their net moments, particularly at low loads when there was minimal co-contraction.

Fifth, I may have underestimated length changes of the AT within the more compliant toe region. If this was the case, then I may have over-estimated AT strain in the linear region and, consequently, AT force. During the isometric protocol, I was unable to resolve the properties of the toe region for 6 of the 10 subjects tested. The properties of the toe region affect estimated tendon force, or more specifically, the tendon length at which the force-length behaviour shifts from toe region (less stiff) to linear region (more stiff) (Eq. 2-1) and this likely has considerable effects on estimated AT forces. To test the implications of my chosen toe region properties and to confirm the values of the slack

length for the linear region of the AT force-length curve (presented in Table 2-1), I plotted the AT forces derived from each subject's net ankle moments (from inverse dynamics) *versus* the ultrasound-based estimates of AT length. This method provided an inverse dynamics estimated AT length at the beginning of the toe region ( $l_{0,AT,toe}$ ) and the linear region ( $l_{0,AT,linear}$ ), which I compared to the values estimated using 310 ° as the position of AT slack length  $l_{0,AT}$  (reported in Table 2-1).

There was no significant difference in  $l_{0,AT,toe}$  and  $l_{0,AT,linear}$  between the 4 crank loads for each subject, so I chose to use the average values for  $l_{0,AT,toe}$  and  $l_{0,AT,linear}$  across the 4 conditions. As well, I determined the toe region and linear region stiffnesses ( $k_{SEE,T}$  and  $k_{SEE}$ ), which I compared to the results from the maximum plantarflexion contractions in the isometric protocol. There was no significant difference in either  $k_{SEE,T}$  or  $k_{SEE}$  between the 4 crank loads for each subject so I used the average values for  $k_{SEE,T}$  and  $k_{SEE}$  across the 4 conditions.

There were no significant differences in the inverse dynamics derived AT slack lengths and the slack length measured at 310 ° of the crank cycle. The results of this analysis showed that the inverse dynamics derived AT slack lengths were on average 0.11 %  $l_{0,AT}$  shorter than the AT slack lengths ( $l_{0,AT}$ ) measured at 310 ° of the crank cycle. However, the average AT lengths at the beginning of the linear portion of the force-length curve, predicted from the inverse dynamics estimates, were 0.10 %  $l_{0,AT}$  longer than AT lengths at the beginning of the linear portion based on the assumptions that AT slack length occurred at 310 ° of the pedal cycle and that for all subjects, toe region strain and stiffness were 1.03 % and 40 N mm<sup>-1</sup>, respectively (Table 2-1).

This suggests that the toe region is longer when using the inverse dynamics method to calculate the AT force-length properties. However, if we assume that the difference in AT slack length change occurs on the linear portion of the force-length curve, where stiffness is greater, this error would result in a difference in AT force of 32 N (using 0.11 %  $l_{0,AT}$ ) between the two methods. The range in differences between the inverse dynamics derived estimate of AT slack length and the AT slack length estimated at 310 ° of the pedal cycle was -0.47% to +0.62%. This range would have resulted in the estimated AT forces to be 151 N higher (using -0.47 %  $l_{0,AT}$ ) to 199 N lower (using 0.62 %  $l_{0,AT}$ ) than

my current estimates of AT force depending on which method I used to determine the start of the linear region of the force-length curve. These potential errors are not negligible and may help to explain why forces were overestimated in some subjects—for example, we could have overestimated force by up to 16 % at the lowest load and 10 % at the highest load (assuming we overestimated force by 151 N). However, the toe region and the linear region stiffnesses from the inverse dynamics derived AT force-length curves matched well with the stiffnesses measured for the toe region (in 4 subjects) and the linear region (in all subjects) on the isometric frame (average difference less than 8 N mm<sup>-1</sup>) providing confidence in our measures of stiffness.

I must also acknowledge that when differentiating between the toe region and linear region using the inverse dynamics data, I chose a cut-off value (120 N). This value was based on the average force at the end of the toe region from the isometric test, where the knee was fixed at 130 °. However during cycling, the AT transitions from the toe region to the linear region of its force-length curve at a changing and more flexed knee angle (60-70 °; Figure 2-8). The MG is bi-articular so at greater knee flexion angles it would have been at a shorter length, thus the net force corresponding to a given length change at the MG MTJ may have been different in the isometric protocol than during pedalling. In the isometric protocol, I did test the effect of varying ankle angle of the AT force-length curve, and found no effect. However my previous work suggests that knee and ankle motions have different influences on the behaviour of the MG under passive conditions (Hodson-Tole et al., 2016). Future studies should aim to understand the relative contributions of the length changes within the MG, LG, and SOL to total AT force under varied joint angles to determine whether it may be necessary to use joint dependent force-length curves when estimating *in vivo* forces from length changes at a single MTJ, similar to the excitation dependent force-length curves that I have implemented here (using scale factor  $c_e$ ).

Others have highlighted that estimated forces are sensitive to the choice of tendon slack length (Xiao and Higginson, 2010; Ackland et al., 2012), however to my knowledge no study has assessed the sensitivity of forces to toe region properties of the tendon force-length curve. The results of this analysis suggest that our overestimation of AT force in some subjects could be explained by the uncertainty in toe region properties, more specifically, the tendon length at which the toe region ends and the linear region begins.

Knowledge of this value is likely to be critical, even more so than AT slack length at the beginning of the toe region, when estimating forces from tendon strains.

Finally, I characterized AT stiffness and estimated AT forces based on length changes measured at the MG MTJ – yet the AT is a composite tendon and thus forces transmitted by the AT depend on length changes of the MG, LG, and SOL. I scaled the measured length changes by a factor ( $c_e$ ) to account for changes in the muscles' relative EMG intensities with load, but this factor may have been too simple to characterize the nonlinear, non-uniform strains within the AT during cycling (Franz et al., 2015). Without the scale factor, subjects' AT forces were consistently over-estimated (Figure 2-13), particularly at low loads when SOL was less active (Figure 2-10 (C)). Also, AT stiffness, determined from the isometric protocol, was established at only one knee angle. Given that the MG and LG cross both the knee and the ankle whereas the SOL only crosses the ankle, knee angle may influence the relative contribution of the 3 muscles to total AT force. For example, when the knee is highly flexed near pedal top dead centre (Figure 2-8), the MG and LG will be at relatively short lengths compared to the SOL, so their relative contribution to total AT force is likely reduced. Future experiments should aim to determine the effect of knee angle on total AT force-length properties.

The peak AT forces that I estimated during cycling (range: 410-2180 N across 10 subjects and 4 loads) are generally greater than the forces measured by Gregor et al. (1987) (range: 480-661 N across 3 loads) –though there is overlap in the forces at low loads, and the subjects' net moments at these loads (Figure 2-15) are similar to those that Gregor et al. reported (1991). Differences in the forces may be related to the invasive nature of tendon buckle experiments (Gregor et al., 1987; 1991) or to differences in the subjects' muscular capacities that influenced their pedalling strategies. Regardless, my study is the first to confirm non-invasively several of the findings reported by Gregor et al. (1987, 1991). For example, I showed that AT force increases with load, consistent with tendon buckle data.

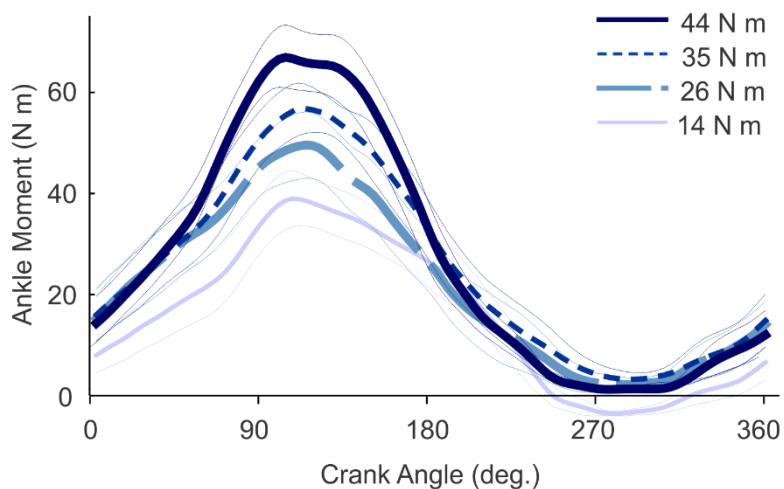


**Figure 2-15. Increase in net ankle moment with crank load at 80 r.p.m.**

Time-varying ankle moments are presented as mean  $\pm$  SE for 10 subjects cycling at 80 r.p.m. at 4 crank loads, corresponding to crank powers of 115, 220, 290, and 370 W. Thin curves represent the SE at each load.

In closing, traditional motion analysis provides information about joint motions during movement, but provides limited insight into muscle-tendon mechanics and the *in vivo* behaviour of skeletal muscle during motor tasks. Hill-type muscle models are increasingly being used within simulations to infer the forces that cause measured motions (e.g. Anderson and Pandy, 2003; Hamner et al., 2010; Kautz and Neptune, 2002), but these predictions are rarely tested against independent measures, such as muscle and tendon length changes or forces determined *in vivo*. Tendon buckle transducers have been used to quantify *in vivo* forces, but remain impractical for most human applications. The ultrasound-based procedure described in this chapter augments existing methods and is applicable to studies of muscle-tendon mechanics and benchmark tests of Hill-type muscle models and muscle-driven simulations.

## Chapter 3.

# **Comparison of gastrocnemius forces predicted by Hill-type muscle models and estimated from ultrasound images during human cycling**

### **3.1. Introduction**

Hill-type muscle models are ubiquitous in biomechanical analyses of movement, providing estimates of a muscle's force as a function of its activation state and assumed force-length and force-velocity properties. For example, Hill-type models have been used, together with reconstructions of musculoskeletal geometry, to analyze the moment-generating capacities of animals during terrestrial locomotion (O'Neill et al., 2013; Hutchinson et al., 2015) and to estimate the locomotor capabilities of extinct species based on fossil records (Hutchinson and Garcia, 2002). Muscle models have also been used in simulations of human locomotion to infer the functions of individual muscles during walking (Arnold et al., 2013) and running (Hamner et al., 2010) and to uncover important insights into the biomechanical factors that contribute to gait abnormalities (e.g. Peterson et al., 2010; Steele et al., 2010). However, the accuracy of the muscle forces predicted by Hill-type models, especially during submaximal, dynamic tasks, remains largely unknown.

The predictive accuracy of Hill-type models has been investigated in a small number of animal studies in which tendon forces were directly measured. For example, Sandercock and Heckman (1997) and Perreault et al. (2003) examined whether a Hill-type model could predict *in situ* forces generated by the cat soleus when they imposed length changes corresponding to those measured during locomotion. Their model reproduced soleus forces measured *in vivo*, using an implanted tendon buckle transducer, to within 10 % of maximal tension during force rise (Sandercock and Heckman, 1997). However, at low motor unit firing rates, differences in the predicted and measured forces were greater than 50 % (Perreault et al., 2003). Previous efforts to predict *in situ* and *in vivo* forces generated by the gastrocnemii muscles of goats (Wakeling et al., 2012; Lee et al., 2013) confirmed that Hill-type models are sensitive to assumptions about activation

state and the force-velocity properties of the models' contractile elements. For example, previous work in our lab showed that Hill-type models reproduced the time-varying forces generated by goats *in vivo* with an average  $r^2$  of 0.40. Errors in force were greater than 15 % and 28 % of maximum isometric force for the MG and LG, respectively when averaged across the gait cycle and across different locomotor speeds. However, errors in force predictions were reduced when models incorporated the independent activations of slow and fast contractile elements, but only during the fastest locomotor speeds (Lee et al., 2013). To date, the ability of Hill-type models to reproduce time-varying muscle force in humans remains unexplored.

To gain more insight into the strengths and weaknesses of Hill-type models, independent estimates of time-varying muscle forces, for a wide range of movements, are needed. However, muscle forces cannot always be directly measured. In chapter 2, I developed and evaluated an ultrasound-based approach to indirectly estimate the *in vivo* forces generated by the human triceps surae muscles during dynamic tasks (Dick et al., 2016). Specifically, I used ultrasound-based measures of tendon length changes, together with subject-specific estimates of tendon stiffnesses and slack lengths, to estimate time-varying forces transmitted by the AT during cycling. In this chapter, I compared gastrocnemii forces predicted by Hill-type models to the forces estimated from ultrasound-based measurements of tendon length changes in humans during cycling over a range of crank loads and cadences. This is the first study to test Hill-type models against *in vivo* estimates of time-varying muscle forces from human subjects.

EMG recordings from the gastrocnemii of cyclists have shown that the recruitment patterns of different muscle fibre types vary with cadence (e.g., Wakeling et al., 2006; Wakeling and Horn, 2009). However, while muscles are composed of a mix of slow and fast fibres with different physiological and biomechanical properties, Hill-type models are typically comprised of a single contractile element with force-length and force-velocity properties that have been estimated from *in vitro* data collected from single fibres under maximally-activated conditions. To represent whole muscle, the fibre's force is scaled based on the muscle's level of activation, accounting for the muscle's physiological cross-sectional area (PCSA), fibre length, pennation angle, and parallel elasticity.

In this chapter, I tested a traditional Hill-type model, with one contractile element, and also a differential model, with slow and fast contractile elements that accounted for the independent contributions of slow and fast muscle fibres. Both models were driven by subject-specific measures of fascicle lengths, velocities, and pennation angles that I derived from ultrasound images and by activation patterns of slow and fast fibres that I derived from surface EMG recordings and wavelet based time-frequency decomposition techniques (von Tscherner, 2000; Wakeling and Horn, 2009). I hypothesized that the two-element model would better reproduce the ultrasound-based estimates of gastrocnemii force at the higher cadences, where preferential recruitment of fast fibres has been reported (Citterio and Agostoni 1984; Wakeling et al., 2006). This is an extension of previous studies done in our lab on the gastrocnemii muscles in goats, where it was shown that a two-element model, driven by the independent activation of slow and fast muscle fibres, provided better predictions of time-varying muscle forces than traditional one-element models for some *in situ* (Wakeling et al., 2012) and *in vivo* (Lee et al., 2013) conditions.

## 3.2. Methods

In this chapter, I analyzed data from 16 competitive cyclists (8 male, 8 female; age:  $30 \pm 7$  years; height:  $173 \pm 7.6$  cm; mass:  $68.8 \pm 10$  kg, mean  $\pm$  S.D) pedalling at 8 different combinations of cadence and load: 60 r.p.m. at 44 N m, 80 r.p.m. at 14 N m, 80 r.p.m. at 26 N m, 80 r.p.m. at 35 N m, 80 r.p.m. at 44 N m, 100 r.p.m. at 26 N m, 120 r.p.m. at 13 N m, and 140 r.p.m. at 13 N m. These methods are largely described in Chapter 2; a brief overview is provided here. I predicted the time-varying forces generated by each subject's LG and MG muscles during cycling using a one-element Hill-type model and a novel two-element Hill-type model. The models were driven by fascicle lengths, velocities and pennation angles that I determined experimentally from ultrasound images, and by muscle activations calculated from simultaneous recordings of surface EMG on the contralateral limb. I compared each subject's predicted LG and MG forces to the forces estimated *in vivo* from ultrasound-based measures of tendon length changes and stiffness.

### 3.2.1. Muscle models for estimating LG and MG forces

I predicted the time-varying forces generated by each subject's LG and MG muscles during pedalling using a traditional Hill-type model:

$$F_m = F_{\max} [\hat{\alpha}(t) \hat{F}_a(l_f) \hat{F}_a(v) + \hat{F}_p(l_f)] \cos \beta \quad (\text{Eq. 3-1})$$

In previous efforts to predict gastrocnemius forces in goats, the intrinsic properties of the contractile element have been formulated in several different ways (Wakeling et al., 2012). However, it was found that the predicted forces were similar across the different formulations (Lee et al., 2013). In this study, I assigned contractile element properties that were consistent with a 'homogeneous one-element model' that assumes the muscle consisted of fibres with homogenous properties. In this model, the maximum intrinsic speed, often referred to as the maximum unloaded shortening velocity ( $v_0$ ), was the maximum intrinsic speed of the different fibre types weighted by their fractional cross-sectional areas. The curvature of the force-velocity relationship ( $\alpha$ ) was an intermediate value between the slow and fast fibres and was assumed to be the same all the fibres within the muscle (Zajac, 1989; Wakeling et al., 2012; Lee et al., 2013) (Figure 3-1 (A)).

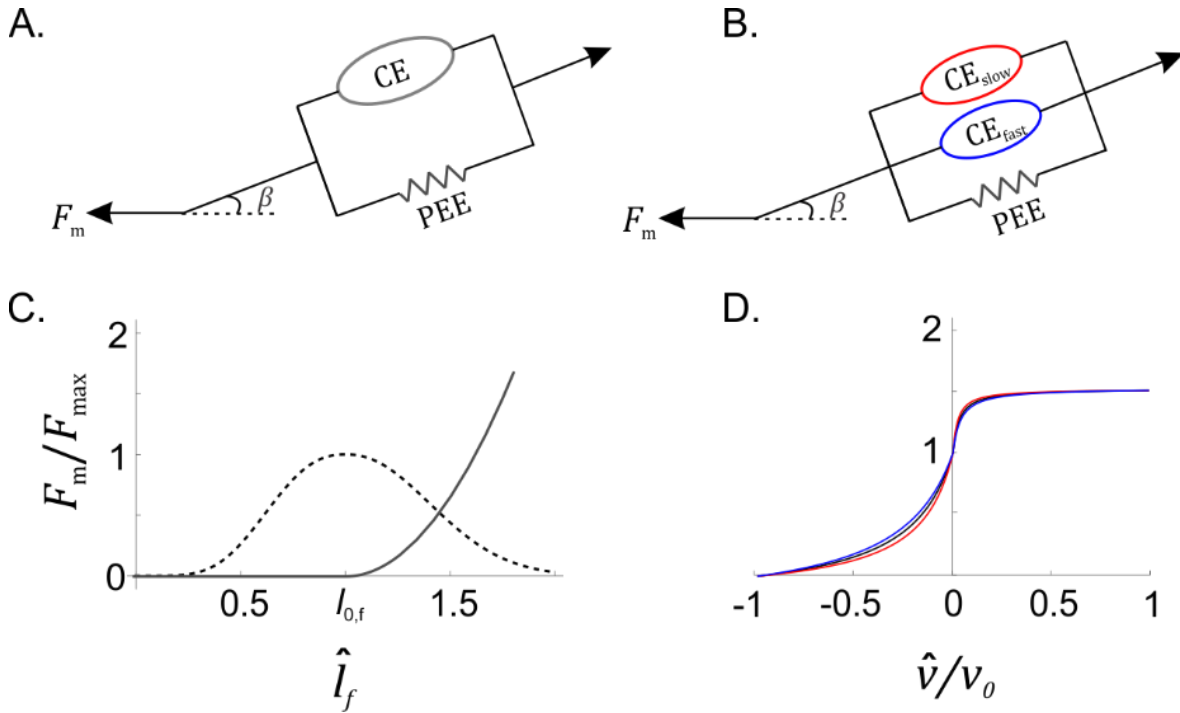


**Figure 3-1. Schematic of muscle models tested.**

One-element (A) and two-element (B) Hill-type muscle models. Normalized active (dashed) and passive (solid) force-length curves (C) and the normalized force-velocity curve used for the contractile element in the one-element model (black) and for the slow (red) and fast (blue) contractile elements in the two-element model (D). CE: contractile element, PEE: parallel elastic element,  $\beta$ : pennation.

I also predicted the subjects' time-varying LG and MG forces using a 'differential two-element model' (Wakeling et al., 2012; Lee et al., 2013) that incorporates independently activated slow and fast contractile elements arranged in parallel (Figure 3-1 (B)):

$$F_m = F_{\max} \left[ [c_1 \hat{a}_{\text{fast}}(t) \hat{F}_a(l_f) \hat{F}_{a,\text{fast}}(v) + \hat{a}_{\text{slow}}(t) \hat{F}_a(l_f) \hat{F}_{a,\text{slow}}(v)] + \hat{F}_p(l_f) \right] \cos \beta \quad (\text{Eq. 3-2})$$

In both models, total muscle force  $F_m$  is a function of the time-varying activation level  $\hat{a}(t)$ , the normalized active and passive force-length relationships  $\hat{F}_a(l_f)$  and  $\hat{F}_p(l_f)$ , respectively, and the normalized force-velocity relationship  $\hat{F}_a(v)$  (Figure 3-2).  $F_{\max}$  represents the subject-specific maximum isometric force of either the LG or the MG:

$$F_{\max} = \left( \frac{v_m}{l_{f,\text{opt}}} \right) \sigma_0 \quad (\text{Eq. 3-3})$$

$F_{\max}$  was calculated based on the muscles' scaled volumes  $V_m$  estimated using the regression equations in Handsfield et al. (2014), and optimal fibre lengths  $l_{f,opt}$  estimated from a subject-specific scaled musculoskeletal model (Arnold et al., 2010),  $\sigma_0$  is estimated specific muscle stress (225 kPa; Spector et al., 1980; Roy et al., 1982) (Table 3-1).  $c_1$  is a scaling factor that accounts for the lower power of the EMG signals that would be expected from action potentials with higher spectral frequencies (Wakeling et al., 2012).  $c_1$  affects the balance between fast and slow fibre contributions and it was given a value of 2 as described below.  $F_{\max}$  scales the fibre (or fascicle) force to whole muscle force and pennation  $\beta$  allows the component of fascicle force that is aligned with the tendon to be estimated.

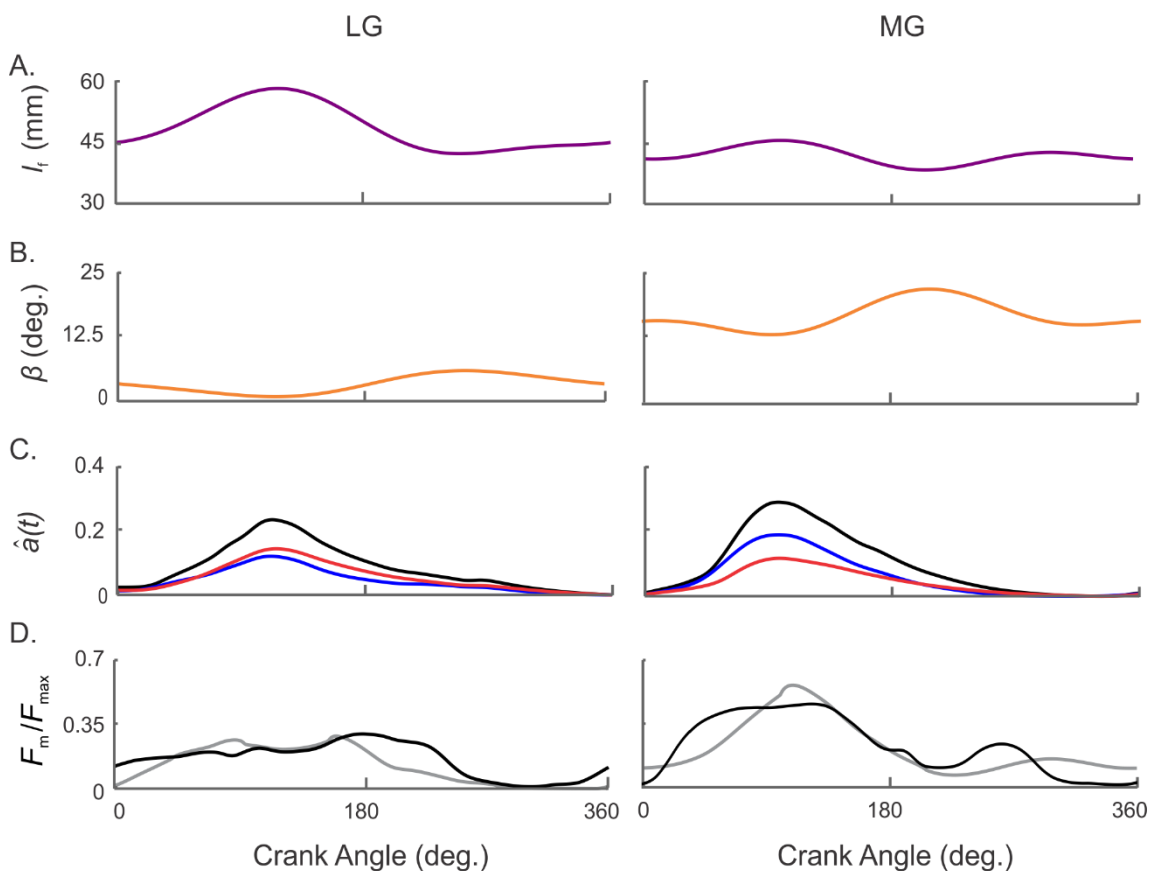


**Figure 3-2. Representative inputs and outputs from muscle models.** Experimental inputs (A-C) and comparisons (D) for muscle models across the entire pedal cycle (crank angle 0°-360°). Fascicle length  $l_f$  (A), pennation angle  $\beta$  (B), normalized lateral (MG) and medial (MG) gastrocnemii muscle activations  $\hat{a}(t)$  for total (black), slow (red), and fast (blue) muscle fibres (C), and the normalized muscle forces predicted by the one-element model (grey) and estimated from the ultrasound-based measures of tendon length changes and stiffness (black)  $F_m/F_{\max}$  (D) for one representative subject pedalling at 80 r.p.m. at 14 N m crank torque.

**Table 3-1. Subject characteristics.**

Subject	Sex	Age (y)	Height (cm)	Body Mass (kg)	LG Max Isometric Force* (N)	MG Max Isometric Force* (N)	LG tendon Stiffness† (N mm <sup>-1</sup> )	MG tendon Stiffness† (N mm <sup>-1</sup> )
1	M	29	186	90.85	674	1179	34.5	63.2
2	M	28	167	68.00	588	1028	22.0	38.9
3	M	33	175	68.00	546	956	36.2	50.0
4	M	32	183	63.00	488	854	22.5	39.0
5	M	37	173	71.80	599	1047	39.2	55.0
6	M	30	179	70.30	555	972	24.5	41.8
7	M	47	183	86.50	661	1157	42.7	59.1
8	M	31	183	82.80	676	1184	26.3	41.2
9	F	30	167	65.80	584	1022	34.5	73.6
10	F	43	174	64.40	552	966	28.9	55.4
11	F	24	171	65.80	571	999	27.8	52.0
12	F	26	167	58.00	500	874	22.1	47.2
13	F	22	160	51.30	474	830	25.3	43.4
14	F	23	168	68.00	608	1065	29.5	58.8
15	F	20	165	67.30	622	1089	26.9	42.4
16	F	32	167	59.40	541	948	38.2	59.2

\* Estimates of the muscles' maximum isometric force-generating capacity based on the muscles' volumes (Handsfield et al., 2014) and optimal fibre lengths, assuming a maximum isometric muscle stress  $\sigma_0$  of 225 kPa. (Spector et al., 1980; Roy et al., 1982).

†Linear region LG and MG AT stiffnesses were estimated as the proportion of the total AT stiffness contributed by each muscle based on ratio of the maximum force-generating capacity  $F_{\max}$  of either the LG or MG to the combined triceps surae maximum force.

The normalized active force-length curve (Figure 3-1 (C)); Otten, 1987) was given by:

$$\hat{F}_a(l_f) = e^{-\left(\left(\frac{l_f^{0.6} - 1}{l_{0,f}^{0.3}}\right)^{2.3}\right)} \quad (\text{Eq. 3-4})$$

The normalized passive force-length curve (Figure 3-1 (C)) was given by:

$$\hat{F}_p = 2.64 \left(\frac{l_f}{l_{0,f}}\right)^2 - 5.30 \left(\frac{l_f}{l_{0,f}}\right) + 2.66 \quad \text{for } l_f > l_{0,f} \quad (\text{Eq. 3-5})$$

$$\hat{F}_p(l_f) = 0 \quad \text{for } l_f \leq l_{0,f} \quad (\text{Eq. 3-6})$$

where  $l_f$  is fascicle length and  $l_{0,f}$  is fascicle slack length.  $l_{0,f}$  was determined to be the length of the fascicle at tendon slack length as determined in Chapter 2. This passive force-length curve is similar to that provided by Millard and co-workers (2013) and is based on a combination of experimental data from chemically-skinned human gastrocnemius fibres (Gollapudi and Lin, 2009) and rabbit whole muscles (Winters et al., 2011).

The normalized force-velocity curve (Figure 3-1 (D)) was given by:

$$\hat{F}_a(v) = \frac{1 - \frac{\hat{v}}{v_0}}{1 + \frac{\hat{v}}{v_0\alpha}} \quad \text{for } v \leq 0 \quad (\text{Eq. 3-7})$$

$$\hat{F}_a(v) = 1.5 - 0.5 \frac{1 - \frac{\hat{v}}{v_0}}{1 - \frac{7.56 \hat{v}}{v_0\alpha}} \quad \text{for } v > 0 \quad (\text{Eq. 3-8})$$

where  $\hat{v}$  is fascicle velocity normalized to  $l_{0,f}$ , which is equivalent to strain rate.  $\alpha$  describes the curvature of the force-velocity relationship and depends on fibre type (Otten, 1987). A literature survey of 59 species from 88 papers concluded that the  $\alpha$  values are 0.18 and 0.29 for slow and fast fibres, respectively (Hodson-Tole and Wakeling, personal communication).  $v_0$  is the maximum intrinsic speed, and I used values of 5 and 10  $l s^{-1}$  for the slow and fast fibres, respectively (Wakeling et al., 2012; Lee et al., 2013). 5 and 10  $l s^{-1}$  are thought to be within the appropriate range for human muscle (Faulkner et al., 1986; Epstein and Herzog, 1998) and are similar to values reported for mouse, cat, and rat muscle measured at physiological temperatures, which range from 4.8 to 7.3  $l s^{-1}$  for slow fibres (Close, 1964; Spector et al., 1980; Askew and Marsh, 1998) and from 9.2 to 24.2  $l s^{-1}$  for fast fibres (Close, 1964; Close, 1965; Luff, 1975; Spector et al., 1980). These values were also selected based on previous modelling results where the sensitivity of predicted forces to different values of  $v_0$  were assessed (Lee et al., 2013).

Histological analysis has shown that the human gastrocnemii contain equal cross-sectional areas of slow and fast muscle fibres (Johnson et al., 1973). Therefore, the one-element homogenous model assumed that the active LG and MG have intrinsic properties that represent the average values for  $\alpha$  and  $v_0$  between slow and fast fibres ( $\alpha = 0.235$ ;

$v_0=7.5 \text{ l s}^{-1}$ ) (Wakeling et al., 2012; Lee et al., 2013). Note that normalized shortening velocity is defined as negative in these equations, while normalized lengthening velocity is defined as positive.  $v_0$  is presented as a positive value, but it is implemented in the models as a negative value.

### **3.2.2. Acquisition of experimental data**

During cycling, I obtained simultaneous recordings of 3D limb and foot kinematics and pedal forces ineffective (radial) and effective (normal) to the crank, as well as LG and MG tendon lengths, fascicle lengths, pennation angles and surface EMG patterns. From an isometric protocol, described in Chapter 2, I determined subject-specific tendon force-length properties (Morrison et al., 2015; Dick et al., 2016). B-mode ultrasound was used to image the gastrocnemii muscle bellies and distal MTJs of the right leg during pedalling while I simultaneously recorded muscle excitations from the LG and MG on the contralateral (left) limb to which the ultrasound transducer was placed.

### **3.2.3. Analysis of experimental data for driving models: muscle fascicle lengths and pennation angles**

Ultrasound was used to alternately image LG and MG fascicles from the right leg during pedalling. The order in which muscles were imaged was randomized; at the end of each block of conditions, the probe was re-positioned over the other muscle. The probe was secured in a custom-made foam support and positioned to image muscle fascicles that were in the middle of the muscle belly where the fascicle architecture is homogeneous (Maganaris et al., 1998a) and in plane with the scanning image (Kawakami et al., 1993).

Ultrasound images were manually digitized (ImageJ, NIH, Maryland, USA) to determine each subject's time-varying fascicle lengths and pennation angles for the eight pedalling conditions (Figure 3-3). Eight points in each ultrasound image were digitized—three points on each of the superficial and deep aponeuroses and two points on a representative muscle fascicle. The aponeuroses were defined based on a linear fit of the three points. Pennation angle was calculated in each image as the mean of the angles made by the fascicle with the deep and superficial aponeuroses. Fascicle lengths and

pennation angles from 10 complete crank revolutions were fit with a 2-harmonic Fourier series, and these data were used as inputs to the muscle models for each muscle, each pedalling condition, and each subject.

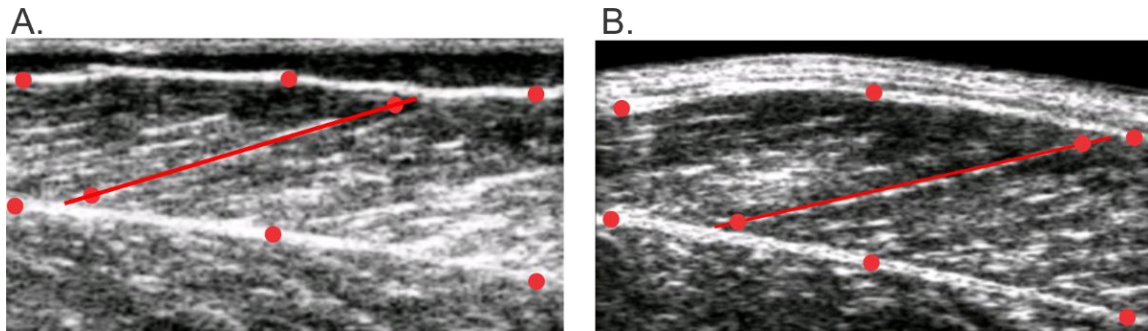


**Figure 3-3. B-mode ultrasound images of the lateral and medial gastrocnemii muscle bellies.**

Images of the LG (A) and MG (B) muscle bellies were digitized to estimate time-varying fascicle lengths. Eight points (red dots) in each ultrasound image were digitized—three points on each of the superficial and deep aponeuroses and two points on a representative muscle fascicle. Pennation angle was calculated as the mean of the angles made by the fascicle (red line) with the deep and superficial aponeuroses.

#### **3.2.4. Analysis of experimental data for driving models: muscle activation patterns**

EMG signals for the LG and MG were quantified by their intensities during each pedal revolution. Intensity was calculated across the frequency band 10–450 Hz using an EMG-specific wavelet analysis (von Tscharner, 2000). Wavelet analysis considers that each motor unit action potential occurs at a distinct time and leaves a distinct frequency spectrum. A bank of non-linearly scaled wavelets was used to analyze EMG to obtain intensity, time, and frequency information (von Tscharner, 2000). Wavelets are preferred over other frequency analysis techniques such as Fourier transforms since, in comparison, they have increased temporal resolution that is likely important when analyzing muscle response times during locomotor tasks with fast movement speeds (Spagele et al., 1999). Also, wavelet analysis provides both time and frequency components of the signal, whereas Fourier analysis provides only frequency information. Wavelets were used by convoluting the myoelectric signal with each wavelet. This is equivalent to passing the myoelectric signal through a band-pass filter with the same frequency characteristics as the wavelet. I calculated the power of the signal (termed the intensity) and this forms an

energy envelope around the square of the signal contained within this wavelet domain (von Tscharner, 2000). The intensity is a close approximation to the time-varying power of the signal and can be calculated across the frequency band of interest. For human EMG signals, I used a bank of 11 non-linearly scaled wavelets that spans frequencies from 10 to 450 Hz (von Tscharner, 2000).

When accompanied with principal component analysis, wavelets can be optimized and tuned to directly target signals from slow and fast motor units and match our best estimate of the frequency spectra of different types of motor units (e.g., Wakeling and Rozitis, 2004; Hodson-Tole and Wakeling 2007; Wakeling and Horn, 2008; Lee et al., 2011). These optimized wavelets can then be applied to EMG signals to calculate the intensities of the slow and fast frequency components to ultimately determine the recruitment of populations of slow and fast muscle fibres during dynamic tasks (Hodson-Tole and Wakeling 2007; Wakeling and Horn, 2008; Lee et al., 2011). In this chapter, I derived muscle-specific optimized wavelets for the gastrocnemii using principal component analysis to identify the major features of the intensity spectra (Figure 3-4). Specifically, the principal components were used to classify the intensity spectra of the myoelectric signal. I used these principal components to reconstruct the intensity spectra that reflect the extreme high and extreme low frequency components of the myoelectric signal. As intensity spectra represent the power within the myoelectric signal they must have non-negative intensities at all frequencies (Figure 3-4). These low and high frequencies were assumed to be representative of slow and fast muscle fibres, respectively (Hodson-Tole and Wakeling 2007; Wakeling and Horn, 2008; Lee et al., 2011). The optimized wavelets were constructed to describe the low and high frequency spectra by fitting a least squares minimisation of a wavelet function  $\psi(f)$  to the reconstructed low and high frequency spectra:

$$\psi(f) = \left(\frac{f}{f_c}\right)^{f_c \cdot s} \cdot e^{\left(\frac{-f}{f_c} + 1\right) \cdot f_c \cdot s} \quad (\text{Eq. 3-9})$$

where  $s$  is a scaling factor that defines the width and shape of the wavelet and  $f_c$  is the central frequency of the wavelet (von Tscharner, 2000). This allowed for identification of the independent recruitment patterns of slow and fast motor units within the muscle (Hodson-Tole and Wakeling, 2007; Wakeling, 2009; Wakeling and Horn, 2009; Lee et al., 2011; Table 3-2). I characterized the signal in two different ways: first by its total intensity

to represent all active motor units within the muscle, and second by the intensity at the low and high frequency bands, calculated using the muscle-specific optimized wavelets, to represent the contributions of slow and fast motor units, respectively. Muscle force is linearly related to the EMG amplitude and not its power (Milner-Brown and Stein, 1975), and so I used the square-root of the EMG intensity as a measure of muscle excitation  $e$ .

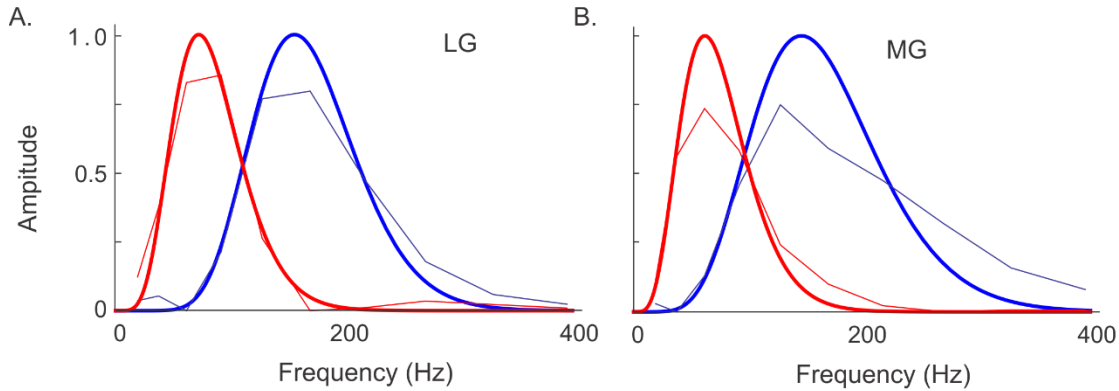


**Figure 3-4. Optimized wavelets for lateral and medial gastrocnemii.** Reconstructed spectra (thin lines) with optimized wavelets (thick lines) for low frequency (red) and high frequency (blue) for the LG (A) and MG (B).

**Table 3-2. Centre frequencies and scale factors of optimized wavelets.**

Muscle	$f_{c\ low}$ [Hz]	$s_{low}$	$f_{c\ high}$ [Hz]	$s_{high}$
LG	72.87	0.085	156.69	0.078
MG	62.32	0.078	146.95	0.051

$f_{c\ low}$  and  $f_{c\ high}$  and scale factors  $s_{low}$  and  $s_{high}$  that characterize the low and high frequency components from the EMG intensity spectra for the muscle-specific optimized wavelets (Eq. 3-9) for the lateral (LG) and medial (MG) gastrocnemii.

In order to compare the time-varying EMG signals from different models, I used the wavelets from von Tschärner (2000) but set the Gauss filter at the end of this process to a 50 ms time resolution for all wavelets. This 50 ms time resolution was chosen to be within the range of physiological time to peak twitch times of skeletal muscle (10 ms and 100 ms, Levin et al., 1999; Spaegle et al., 1999).

Muscle excitation represents the motor unit action potentials, whereas activation level is related to the concentration of calcium ions within the sarcoplasm. In my thesis I used a first-order differential equation (transfer function) that relates the muscle excitation  $e(t)$  to the active state of the muscle  $a(t)$  (Zajac, 1989):

$$\frac{d}{dt}(a) + \left[ \frac{1}{\tau_{act}} (\beta_{act} + [1 - \beta_{act}]e(t)) \right] a(t) = \left( \frac{1}{\tau_{act}} \right) e(t) \quad (\text{Eq. 3-10})$$

The activation time constant  $\tau_{act}$ , specific to slow and fast fibres, and the ratio  $\beta_{act}$  of the activation to deactivation time constants were derived using tetanic contraction data in the literature (Table 3-3). To derive these constants, I manually traced (ImageJ, NIH, Maryland, USA) tetanic curves for cat slow and fast motor units (Kernell et al., 1983) and optimized the parameters  $\tau_{act}$  and  $\beta_{act}$  to reproduce the force traces for a matched stimulation duration.

**Table 3-3. Constants for the excitation-activation transfer functions.**

Constant	Fast Excitation	Slow Excitation	Total Excitation
$\tau_{act}$ [ms]	25	45	35
$\beta_{act}$	0.6	0.6	0.6

$\tau_{act}$  is the activation time constant and  $\beta_{act}$  is the ratio of the activation to deactivation time. These are the values used in Eq. 3-10 to derive activation from excitation.

Histological analysis has shown that the human gastrocnemii contain equal cross-sectional areas of slow and fast muscle fibres (Johnson et al., 1973). Therefore,  $\tau_{act}$  for the activation transfer function for the “one-element” model was calculated as the average between slow and fast fibres. The ratio of activation to deactivation,  $\beta_{act}$ , was independent of fibre-type since both activation and deactivation rates are associated with the motor-unit type (Burke et al., 1973). I used the transfer function to derive the active state for the whole muscle (from the total EMG intensity), as well as for slow and fast motor units. In order to make comparisons between the one- and two-element models, the activation level of the summed slow and fast motor units was scaled in amplitude to equal the total activation during the maximum-effort pedalling trials. Activation traces from 10 cycles were combined to compute a mean LG and MG total, slow, and fast muscle activation trace for each pedalling condition. Activation levels for each muscle are presented as normalized

values  $\hat{a}(t)$  calculated relative to the maximum activation detected during the maximum-effort pedalling trials.

### 3.2.5. Analysis of experimental data for evaluating models: *in vivo* forces

I estimated *in vivo* muscle forces from tendon length changes and stiffness to evaluate the predictions of my Hill-type models. Using ultrasound, I calculated the length changes of each tendon  $l_{AT-LG}$  or  $l_{AT-MG}$  during cycling as the distance from the AT insertion on the calcaneus to the 3D position of the LG or the MG MTJ. I estimated each muscle's contribution to tendon force,  $F_{LG}$  and  $F_{MG}$  (equation shown for MG), during cycling based on the measured length changes  $l_{AT-LG}$  or  $l_{AT-MG}$ , the subject-specific values of toe region stiffness  $k_{SEE,T-LG}$ ,  $k_{SEE,T-MG}$  and linear region stiffness  $k_{SEE-LG}$ ,  $k_{SEE-MG}$  for either the LG or MG (equation shown for MG) (Table 3-1), and the tendon slack length  $l_{0,AT-LG}$  or  $l_{0,AT-MG}$ .

$$F_{MG} = \begin{cases} 0, & l_{AT-MG} \leq l_{0,AT-MG} \\ k_{SEE,T-MG}(l_{AT-MG} - l_{0,AT-MG}), & l_{0,AT-MG} < l_{AT-MG} \leq (l_{0,AT-MG})1.0103 \\ k_{SEE-MG}(l_{AT-MG} - (l_{0,AT-MG})1.0103) + k_{SEE,T-MG}(l_{0,AT-MG}(0.0103)), & (l_{0,AT-MG})1.0103 < l_{AT-MG} \end{cases} \quad (\text{Eq.3-11})$$

Linear region AT stiffnesses  $k_{SEE-LG}$  and  $k_{SEE-MG}$  were estimated from ramped isometric tests where I quantified the total stiffness of the AT (presented in Chapter 2), and for the purposes of this chapter, I also determined the proportion of the total AT stiffness contributed by each of the LG  $k_{SEE-LG}$  and MG  $k_{SEE-MG}$  separately. These muscle-specific stiffnesses were calculated based on the ratio of the maximum force-generating capacity  $F_{\max}$  of either the LG or MG to the combined triceps surae maximum force (Table 3-1). The same toe region stiffness was used for the LG and the MG. Tendon slack lengths  $l_{0,AT-LG}$  and  $l_{0,AT-MG}$  were measured at 310 ° of the crank cycle, averaged over all cycles as described in Chapter 2; this choice was motivated by published tendon buckle data (Gregor et al., 1987). The time-varying tendon force from 10 cycles was used to compute a mean force trace for each condition.

### 3.2.6. Comparison of predicted and estimated forces

I used the one- and two-element models to predict time-varying LG and MG forces for the 16 subjects and 8 pedalling conditions. Additionally, because the forces predicted by Hill-type models are sensitive to the assumed maximum intrinsic speed  $v_0$  and curvature  $\alpha$  of the force-velocity relationship (Shue et al., 1995; Perreault et al., 2003; Wakeling et al., 2012; Lee et al., 2013), I performed a sensitivity analysis and ran the models varying the values of  $\alpha$  and  $v_0$  to determine the extent to which the modelled forces were sensitive to these force-velocity properties. I compared the predicted forces to the forces estimated from ultrasound-based measures of tendon length changes and stiffness, and I characterized differences across the crank cycle using two measures: the coefficient of determination  $r^2$  and the root mean square error (RMSE).  $r^2$  was determined using correlation analysis between the model's predicted forces and the forces estimated from ultrasound-based approach, calculated over the entire crank cycle. RMSE was calculated as the square root of the mean squared differences between the model's predicted forces and the forces estimated from ultrasound-based approach, calculated over the entire crank cycle. A general linear model ANOVA was conducted to determine if differences in the  $r^2$  and RMSE (dependent variable) existed between models, muscles, cycling conditions, subject (random), and values of  $\alpha$  and  $v_0$ . I used chi-square tests at each pedalling condition to determine whether the two-element model reproduced the estimated forces in the LG and MG better than the one-element model (higher  $r^2$  and lower RMSE, each performed as independent tests) over the entire crank cycle, more often than the one-element model. Additionally, an ANCOVA identified changes in the mean muscle activity for total, fast, and slow motor units with cadence, crank load, and fascicle length  $l_f/l_{0,f}$  as covariates and subject as a random factor. Differences were considered significant at the  $p < 0.05$  level. Data are reported as mean  $\pm$  SE.

## 3.3. Results

The traditional one-element Hill-type model, driven by EMG-derived activations and ultrasound-based measures of fascicle lengths, velocities and pennation angles, predicted 30-80 % ( $r^2$ ) of the gastrocnemii forces generated by human subjects during cycling, when compared to the ultrasound-based estimates of tendon force (Figure 3-5).

Peak LG and MG forces predicted by the one-element model were generally within 10 % of the peak forces estimated from ultrasound images and tendon stiffness measurements. In particular, the differences in peak forces were  $10.8 \pm 1.2 \% F_{\max}$  for the LG and  $7.2 \pm 1.4 \% F_{\max}$  for the MG when averaged across subjects and conditions. Time-varying patterns of the predicted and estimated forces, as assessed by the coefficient of determination  $r^2$  and RMSE, showed greater differences than the peak forces (Figures 3-4; 3-5). For some subjects and pedalling conditions,  $r^2$  values were as high as 0.85; in other cases,  $r^2$  values were only 0.31. A comparison of the modelled forces between the pedalling conditions, between muscles, and between the one- and two- element models are shown in Figure 3-6.

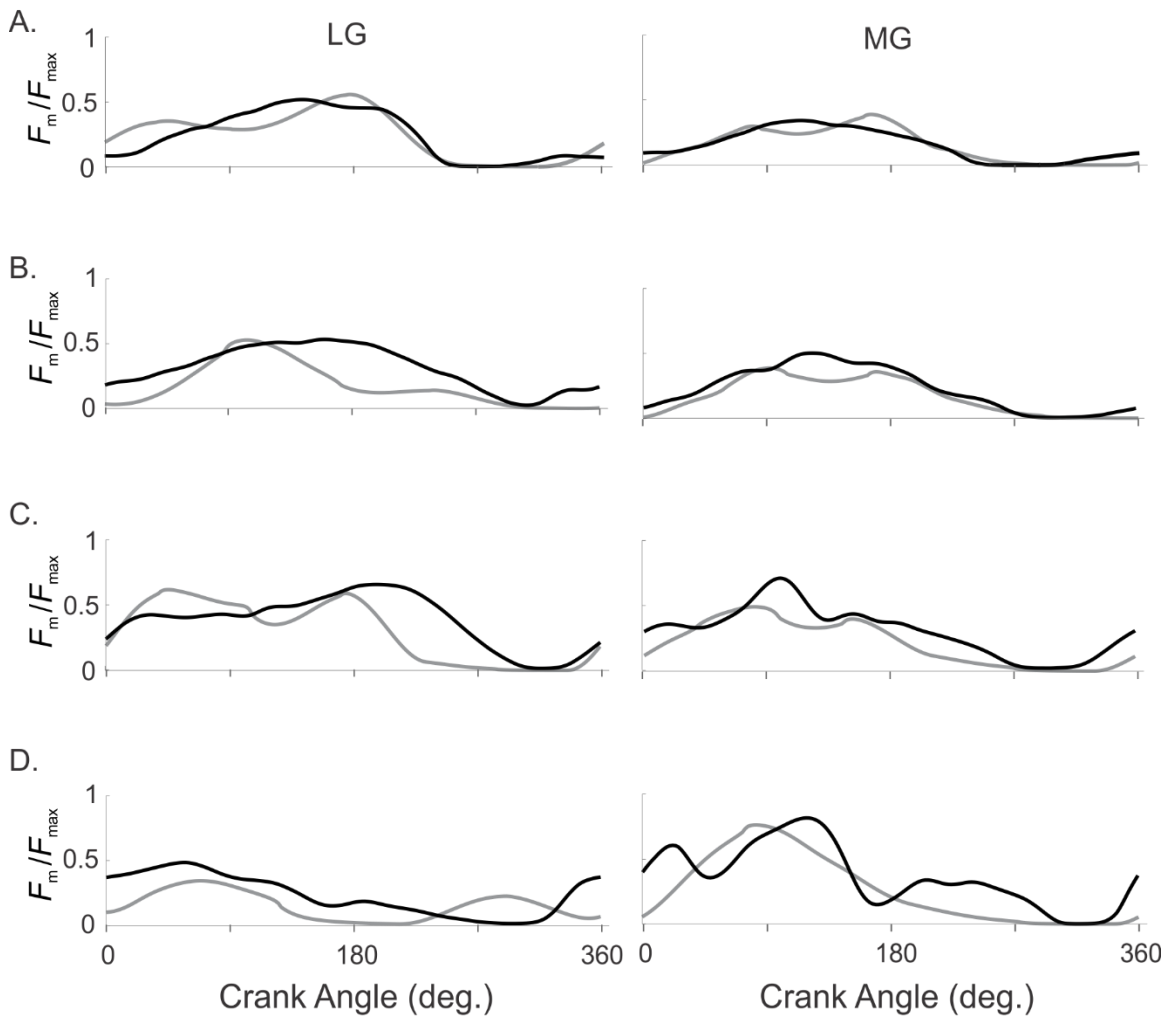


**Figure 3-5. Force profiles for the LG and MG during four different pedalling conditions for one representative subject.**

Time-varying force profiles for the LG and MG at 60 r.p.m. at 44 N m (A), 80 r.p.m. at 44 N m (B), 100 r.p.m. at 26 N m (C), and 140 r.p.m. at 13 N m (D) for one representative subject.

Ultrasound-based estimates of force are represented in black, predicted forces from the one-element model in grey. Muscle forces  $F_m$  are normalized to the maximum isometric force  $F_{max}$  of either the LG or the MG.

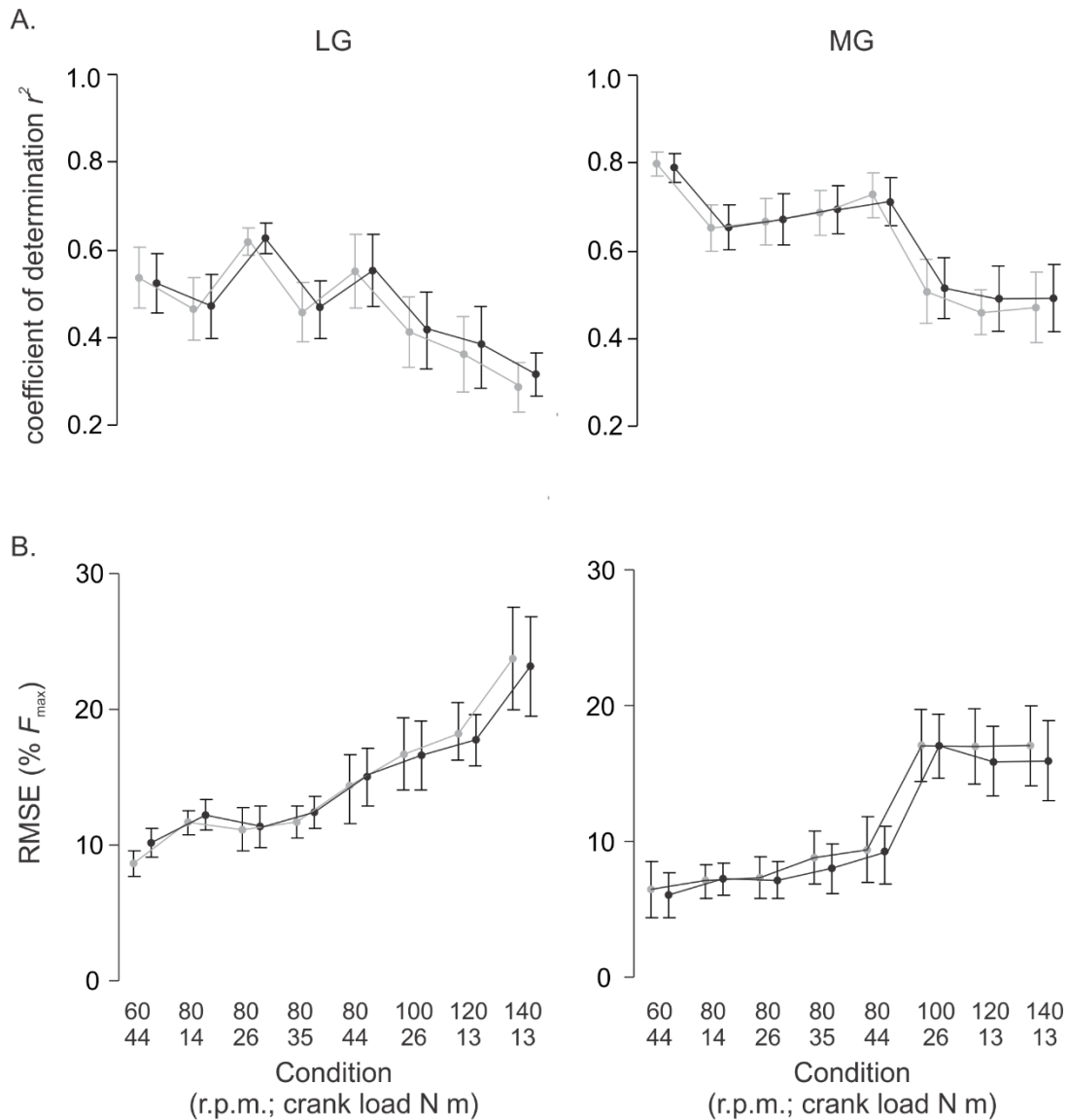


**Figure 3-6. Comparison of the one- and two-element Hill-type models predicted forces to ultrasound-based estimates of force.**

Model predictions differ between muscles, pedalling conditions, and model type. Comparison of the one-element (grey) and two-element (black) Hill-type models  $r^2$  (A) and RMSE (B) across the pedal cycle for the LG and MG across pedalling conditions. Data points shown represent the mean  $\pm$  SE across all subjects at each pedalling condition.

Consistent with previous literature (Wakeling et al., 2006; Blake and Wakeling, 2014) the conditions tested in my study elicited a range of recruitment patterns between slow and fast motor units (Figure 3-7), providing rationale to test the two-element model. The average total activation calculated for the whole crank cycle increased with both crank torque and cadence in both the LG and MG across all subjects ( $p < 0.05$ ). Activation of the

slow motor units decreased with cadence (LG:  $p=0.02$ , MG:  $p=0.045$ ) but increased with crank torque (LG and MG:  $p<0.05$ ). Fast motor unit activation increased with both cadence and load in the LG and MG ( $p<0.05$ ). Therefore, increased cadence resulted in a reduction of slow motor unit activity coupled with an increase in the fast motor unit activity.

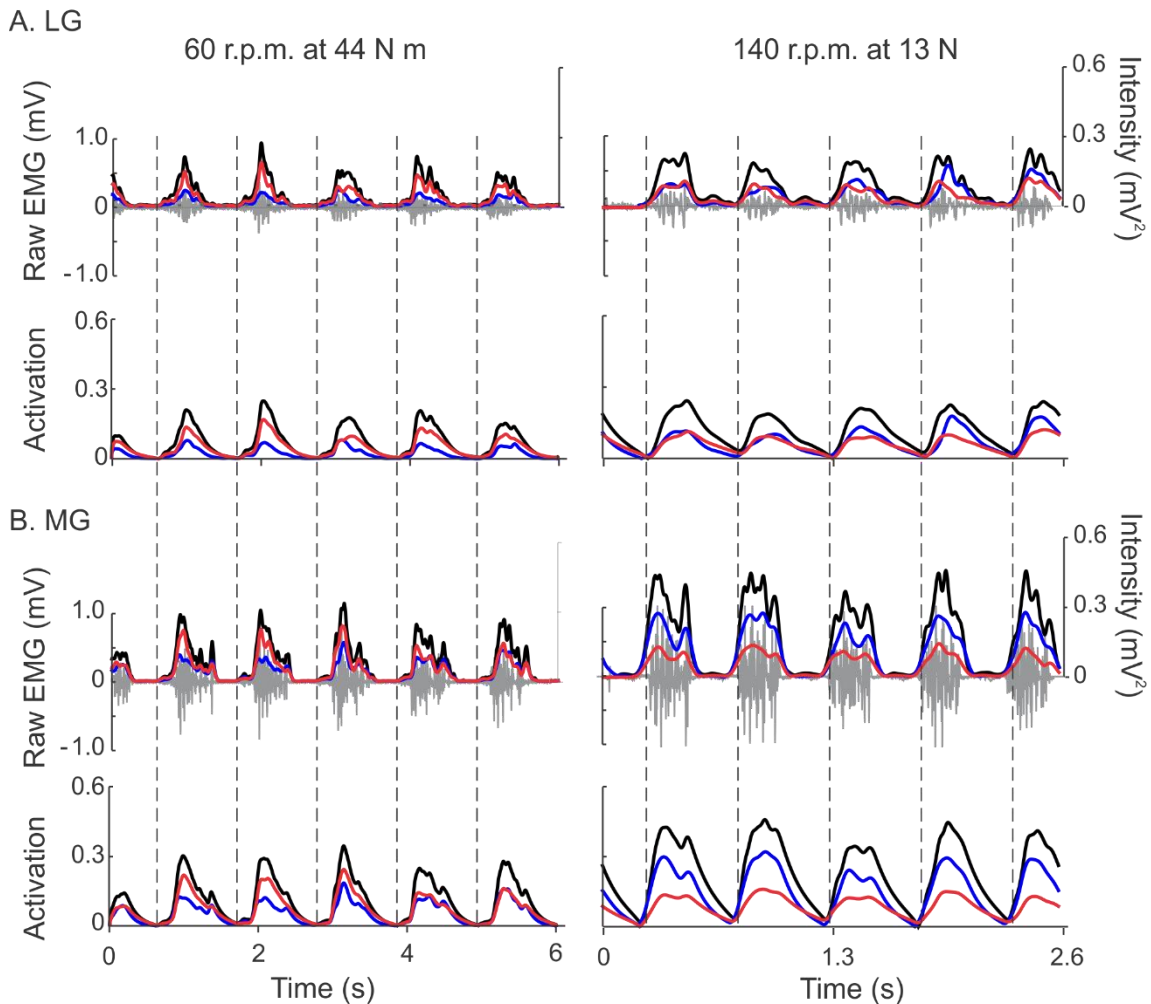


**Figure 3-7. Differential recruitment of slow and fast muscle fibres with pedalling condition.**

Raw EMG (grey) and total (black), slow (red), and fast (blue) intensity and activation traces for one representative subject LG (A) and MG (B) pedalling at 60 r.p.m. at 44 N m (left panel) and 140 r.p.m. at 13 N m (right panel). Vertical dashed lines show timing of pedal top-dead-centre. These conditions have been chosen to highlight the differences in recruitment between slow and fast muscle fibres that can occur across the range of mechanical conditions tested here.

The Hill-type models tested in this chapter reproduced the estimated forces for the MG more accurately than for the LG. Both the one- and two-element models predicted forces with a higher  $r^2$  over the crank cycle for the MG as compared to the LG across all pedalling conditions ( $p < 0.05$ ) (Figure 3-6; Table 3-4). The average coefficient of determination  $r^2$  computed across all subjects and pedalling conditions decreased from 0.62 (range: 0.45-0.79) for the MG to 0.47 (range: 0.29-0.62) for the LG. However, the average RMSE over the crank cycle was similar between muscles: 13.57 %  $F_{\max}$  (range: 9.86-18.25) for the MG and 12.84 %  $F_{\max}$  (range: 7.98-21.91) for the LG.

**Table 3-4. Average LG and MG coefficient of determination  $r^2$  and RMSE between model predictions and ultrasound-based estimates of force, using the one-element and the two-element models across pedalling conditions.**

Cadence (r.p.m.)	crank load (N m)	LG				MG			
		$r^2$ one-element	$r^2$ two-element	RMSE (% $F_{max}$ ) one-element	RMSE (% $F_{max}$ ) two-element	$r^2$ one-element	$r^2$ two-element	RMSE (% $F_{max}$ ) one-element	RMSE (% $F_{max}$ ) two-element
60	44	0.54±0.07	0.52±0.07	7.98±0.86	9.38±0.95	0.79±0.03	0.78±0.03	10.17±1.60	9.86±1.26
80	14	0.46±0.07	0.47±0.07	10.78±0.83	11.32±1.05	0.64±0.05	0.65±0.05	10.60±0.99	10.77±0.89
80	26	0.61±0.03	0.62±0.04	10.27±1.47	10.45±1.40	0.66±0.05	0.66±0.05	10.83±1.20	10.67±1.04
80	35	0.46±0.07	0.46±0.07	10.80±1.20	11.46±1.09	0.68±0.05	0.68±0.05	11.96±1.49	11.36±1.40
80	44	0.55±0.08	0.55±0.08	13.05±2.33	13.88±1.95	0.71±0.05	0.71±0.05	12.39±1.86	12.09±1.59
100	26	0.41±0.08	0.42±0.09	15.40±2.44	15.34±2.36	0.50±0.07	0.51±0.07	18.25±2.03	18.26±1.82
120	13	0.38±0.08	0.38±0.09	15.49±1.99	16.40±1.73	0.45±0.05	0.46±0.05	16.93±2.09	17.45±2.01
140	13	0.29±0.06	0.32±0.05	21.91±3.50	21.40±3.36	0.46±0.08	0.49±0.08	17.53±2.25	17.43±2.25
	Average	0.46	0.47	13.21	12.47	0.61	0.63	13.65	13.49

Data are presented as mean ± SE;  $r^2$  and RMSE were calculated for the time-varying forces across one complete pedal revolution.

Differences in the peak forces predicted by the two-element model were less than the differences in peak forces predicted by the traditional one-element model in both the LG and MG. In particular, when averaged across subjects and conditions, the differences for the two-element model were  $8.2 \pm 1.7 \% F_{\max}$  and  $5.1 \pm 1.1 \% F_{\max}$  for the LG and MG, respectively, compared to  $10.8 \pm 1.2 \% F_{\max}$  and  $7.2 \pm 1.4 \% F_{\max}$  for the one-element model LG and MG, respectively. On average, the one- and two-element models performed similarly at low cadences (Figure 3-6; Table 3-4). However at high cadences (100 r.p.m. to 140 r.p.m.), the two-element model predicted forces with a higher  $r^2$  and lower RMSE across the crank cycle in comparison to the one-element model (Figure 3-6; Table 3-5), although the differences were small (Table 3-4).

**Table 3-5. Chi-square test results for comparison of  $r^2$  and RMSE between one-element and two-element Hill-type muscle models.**

Cadence (r.p.m.)	Load (N m)	Coefficient of determination, $r^2$		RMSE	
		two-element (% total)	P-value	two-element (% total)	P-value
60	44	46.9	0.73	37.5	0.15
80	14	59.4	0.29	28.1	0.01
80	26	62.5	0.16	43.8	0.47
80	35	65.6	0.07	43.8	0.47
80	44	59.4	0.29	46.9	0.72
100	26	71.9	0.01*	62.5	0.15
120	13	68.8	0.03*	68.8	0.03*
140	13	71.9	0.01*	68.8	0.03*

Values in % total column indicate the number of times for the combined MG and LG results across individual subjects and pedalling conditions, as a %, that the two-element model performed better (higher  $r^2$  and lower RMSE). Differences were considered significant at the  $p < 0.05$  level.

\*indicates  $p < 0.05$

The forces predicted by the Hill-type models tested here were sensitive to the force-velocity curvature  $\alpha$  used (Figure 3-8). In both the LG and MG, the models predicted force with a higher  $r^2$  and lower RMSE (data not shown) when using  $\alpha = 0.235$  or  $\alpha = 0.315$  for the one-element model, as compared to  $\alpha = 0.155$  when averaged across all pedalling conditions (Figure 3-8 (A)). The most notable differences in model

performance with  $\alpha$  were evident at cadences of 100 r.p.m. and above, where models predicted force with a higher  $r^2$  and lower RMSE when using greater  $\alpha$  values (Figure 3-8 (A)). In contrast, the predicted forces were not sensitive to the maximum intrinsic speed  $v_0$  implemented within the models. These trends were similar for the one-element and two-element models tested (data shown for the one-element model; Figure 3-8). Most importantly, the results of the sensitivity analysis provide rationale for the values used as input parameters for  $\alpha$  and  $v_0$ , as incorporated within the models used in this chapter.

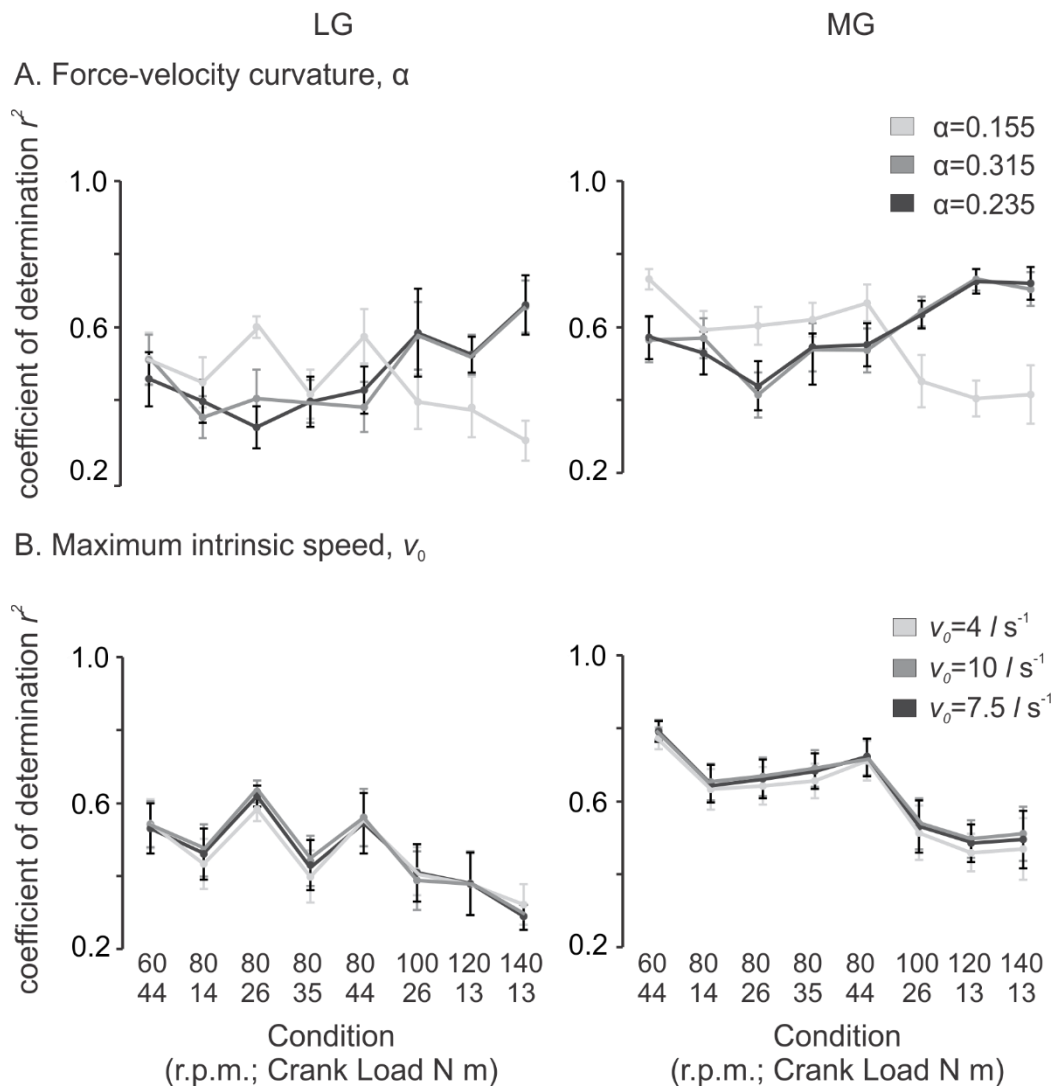


**Figure 3-8. Results of sensitivity analysis to force-velocity parameters.** Sensitivity of one-element model predictions to force-velocity parameters: curvature of force-velocity relation  $\alpha$  (A), and maximum intrinsic speed  $v_0$  (B) in the LG and MG. Data points shown represent the mean  $\pm$  SE across all subjects.

## 3.4. Discussion

In this chapter, I have shown that Hill-type muscle models, driven by EMG-derived activations and ultrasound-based measures of fascicle lengths, velocities and pennation angles, predict 30-80 % of the gastrocnemii forces generated by human subjects during cycling, as estimated via ultrasound-based estimates of tendon length changes. Further, this work provides the first comparison of forces predicted by Hill-type models –driven with *in vivo* human experimental data under submaximal dynamic tasks –to ultrasound and tendon stiffness-based estimates of muscle-tendon force. Identifying the underlying sources of error in force predictions from Hill-type models remains challenging, particularly when having to rely on non-invasive estimates of muscle-tendon force. However, the approach described here provides an important step and an experimental framework for investigating how Hill-type models may be improved; for example, by accounting for the effects of task-specific variations in the recruitment patterns of slower and faster motor units.

### 3.4.1. Comparison to Hill-type models in the literature

Previous studies have assessed the accuracy of Hill-type models against direct measures of force from tendon buckle recordings in animals (Sandercock and Heckman, 1997; Perreault et al., 2003; Wakeling et al., 2012; Lee et al., 2013; Kim et al., 2015) or against measures of heat and work (Umberger et al., 2003; Lichtwark and Wilson, 2005b). In particular, modelling *in situ* forces yielded higher  $r^2$  values (Sandercock and Heckman, 1997; Perreault et al., 2003; Wakeling et al., 2012) than *in vivo* forces (Lee et al., 2013), which likely relates to the more controlled contractions studied during *in situ* experiments in comparison to *in vivo* experiments. Unlike these previous studies, the human muscle models tested here relied on estimates of muscle length and force measured non-invasively using ultrasound, tendon stiffness and surface EMG signals. Further, rather than relying on optimized values, the models in this study used either experimentally derived values of fascicle length, and pennation angle or physiological values, such as those that define the force-length and force-velocity relationships, presented in the literature. I generated comparable force predictions (LG  $r^2=0.29-0.62$ , MG  $r^2=0.45-0.79$ , LG RMSE= 7.98-21.91 %  $F_{\max}$ , MG RMSE= 9.86-18.25 %  $F_{\max}$ ) to the *in situ* (LG  $r^2=0.84$ ,

MG  $r^2=0.76$ ) and *in vivo* (LG  $r^2=0.32-0.51$ , MG  $r^2=0.26-0.48$ , LG RMSE=17-32.2 %  $F_{\max}$ , MG RMSE= 9.6-15.5 %  $F_{\max}$ ) models, which were tested against direct *in vivo* measures of force and length in animals (Wakeling et al., 2012; Lee et al., 2013).

The one- and two-element models tested here use the same formulation (Eq. 3-1, 3-2) as those tested in animal models (e.g., Lee et al., 2013) however there are notable differences in (i) the experimental data used to drive the models and (ii) how the equations within the models were determined. In my studies on human muscle, models were driven with measurements of fascicle length, determined from B-mode ultrasound, and activation, determined from surface EMG and an excitation-activation transfer function commonly used in human muscle models (Zajac, 1989). In the goat studies (Wakeling et al., 2012; Lee et al., 2013), the models were driven with fascicle lengths, determined from sonomicrometry, and activation, determined from fine-wire EMG and a 3-step transfer function determined directly from *in situ* twitch contractions in the goat gastrocnemii. Additionally, in the goat experiments, the active and passive force-length relationships were measured directly from *in situ* experiments in goats, whereas the models tested in this study relied on values taken from the literature collected from a range of animal species. The same force-velocity relationship was used in both studies, however in the goat experiments immunohistochemical testing of the LG and MG confirmed the appropriate force-velocity curvature values to be used within the models whereas we did not have this data. Finally, during the cycling experiments we measured tendon strain and fascicle length in separate pedalling trials. This was necessary because it was not possible to simultaneously secure two ultrasound probes on the same muscle during pedalling (to measure displacement of the MTJ and fascicle length). Therefore, the experimental data that was used to drive the models was based on a different pedalling trial, although at the same mechanical conditions, than the data that model predictions were compared against. To confirm that the pedalling trials were consistent, the magnitude and timing of the pedal forces between trials were compared. If the difference in time-varying crank forces was >5 % between the two trials, these data were not included in the analysis. By contrast, in the goat studies, tendon force and fascicle length were determined simultaneously and model predictions were compared to the time-varying *in vivo* forces over each stride, rather than the average values across cycles. So are non-invasive measurements of skeletal muscle contractile properties as accurate as invasive measurements? Unfortunately research

comparing, for example, fascicle lengths determined from B-mode ultrasound *versus* those determined from sonomicrometry, does not exist. However one study suggests that surface EMG measurements may record additional muscle activity, from cross-talk of surrounding muscles, at low contraction levels during high load isometric tests in comparison to fine-wire EMG (Semciw et al., 2014). Future work should aim to identify the potential for non-invasive gold standard measurements of skeletal muscle contractile properties.

### **3.4.2. Differences between muscles and pedalling conditions**

Human LG and MG muscles vary in architecture (Maganaris, 1998), recruitment patterns (Wakeling et al., 2011) and motor-unit twitch profiles (Vandervoort and McComas, 1983). Specifically, the MG has shorter, more pennate fascicles than the LG (Wakeling et al., 2006; Ward et al., 2009), while the LG has a more complex architecture than the MG, with multiple heads that have different fascicle arrangements (Wolf et al., 1998). This complexity may have diminished my ability to accurately estimate the lengths, velocities, and pennation angles of the LG, which were sensitive to the location of the ultrasound probe relative to the muscle. Consequently, these differences may help to explain the variation in model performance shown here, particularly my finding that models reproduced the estimated forces more closely across the pedal cycle for the MG than the LG, which is consistent with the modelling results in the gastrocnemii of goats (Lee et al., 2013).

Model predictions also varied with cadence. The one- and two-element models predicted forces with higher  $r^2$  and lower RMSE values at low cadences (60-80 r.p.m.,  $r^2=0.61\pm 0.1$ ,  $RMSE= 11\pm 1.2\% F_{max}$ ) than at high cadences (100-140 r.p.m.,  $r^2=0.42\pm 0.07$ ,  $RMSE= 17.6\pm 2.1\% F_{max}$ ) for the LG and MG. In part, this likely reflects the increased errors in digitizing the ultrasound images at higher cadences when determining fascicle length changes and motions of the MTJ, which are critical to quantifying changes in tendon length, from which muscle-tendon forces were estimated. The gastrocnemii also bulge (Fukunaga et al., 1997; Kawakami et al., 1998; Maganaris et al., 1998a; Randhawa et al., 2013) when they contract, and these shape changes likely have an effect on the force output of muscle. However, the models implemented here fail to account for changes in

muscle thickness and depth, which are thought to be important in uncoupling fascicle velocity from that of the whole MTU (Azizi et al., 2008). It has been suggested that the structural and material properties of connective tissue likely affect muscle bulging, the gearing of whole muscle to fascicle length change, and ultimately the mechanical output of a muscle during contraction (Azizi et al., 2008). Muscle gearing is likely important for predicting operating velocity and force, thus it is possible that dynamic changes in muscle shape during a contraction, which Hill-type models largely ignore, as those tested here, may help to reduce discrepancies between ultrasound estimated and model predicted forces at higher cadences. I address this question in Chapter 4.

### **3.4.3. Comparison of one- and two-element models**

The main differences between the one- and two-element models are the active states and associated force-velocity parameters that drive slow *versus* fast contractile elements. The one-element model was driven by the muscle's total active state and average force-velocity properties, whereas the two-element model was driven by the independent active states and force-velocity properties of slow and fast fibres acting in parallel to each other (Figure 3-1). The differences in the muscle forces predicted by the two models were small at low cadences but increased at higher cadences (Figure 3-6; Table 3-5). These results are consistent with a previous study of goat gastrocnemii (Lee et al., 2013), in which a two-element model generated significantly better force predictions than a one-element model during galloping, but not walking or trotting.

Consistent with previous cycling studies (Wakeling et al., 2006; Wakeling and Horn, 2009; Blake and Wakeling, 2014), higher cadences elicited differential recruitment patterns that displayed an increase in the activation of the faster motor units coupled with a decrease in activation of the slower motor units, when compared to the lower cadences (Figure 3-7). However, the differences between predicted forces for the one- and two-element models at even these highest cadences were minor. This could be attributed to the fact that (i) the one-element model was not sensitive to  $v_0$  (Figure 3-8) or (ii) the differences in recruitment across the range of loads and cadences tested here may not have been large enough to elicit substantial differences in model performance. The differences between the forces predicted by the one- and two-element models in this study

were smaller than the differences predicted by similar one- and two-element models in the goat gastrocnemii (Lee et al., 2013). This may be related to differences in the relative recruitment between fast and slow fibres necessary for galloping versus high speed cycling. Alternatively, consistent with recent work indicating that the recruited fraction of a muscle's fibres is most critical to determining muscle force-velocity properties (Holt et al., 2014), differences in the recruitment of slow *versus* fast fibres across the cycling conditions examined here may not be as important as the fraction of gastrocnemii fibres recruited to power cycling at different loads and cadences.

To date, our understanding of whole muscle behaviour has come from studies in which muscles are maximally activated, yet recent evidence suggests that muscle behaviour may be different depending on the level of activation (Rack and Westbury, 1969; Josephson and Edman 1988; Rassier et al., 1999; Holt and Azizi, 2014; Holt et al., 2014; Holt and Azizi, 2016). One previous study (Holt et al., 2014) has shown that the effects of accounting for the percent of total muscle activated are more substantial than the effects accounting for independent differences in slow and fast motor unit recruitment when measuring whole muscle behaviour. Specifically, Holt et al. (2014) demonstrated that activating faster motor units does not result in faster rates of force development or higher shortening velocities than activating both slow and fast motor units in an isolated whole muscle, suggesting that the physical properties of skeletal muscle (e.g., mass, viscosity) may obscure the mechanical effects of differential recruitment between muscle fibre types. This is an underappreciated topic that to my knowledge only two studies have explored (Josephson and Edman, 1988; Holt et al., 2014); thus, we still know little about whole muscle contractile properties during submaximal contractions, and even less about whole muscle contractile properties within intact musculoskeletal systems, where surrounding muscles and bones likely have an effect on muscle behaviour. Future work should aim to consider the mechanical effects of physical properties (e.g., mass, viscosity), as well as the potential contributions of elastic tissue (e.g., aponeurosis) on muscle contractile function, which will be critical to improving more reliable muscle models and for understanding whole-muscle function during dynamic sub-maximal contractions.

#### 3.4.4. Sensitivity of models to assumed intrinsic properties

Previous studies have shown that the errors in forces predicted by Hill-type models are often related to the assumed maximum intrinsic speed  $v_0$  and curvature  $\alpha$  of the force-velocity relationship (Shue et al., 1995; Perreault et al., 2003; Wakeling et al., 2012; Lee et al., 2013). In contrast to a previous study (Lee et al., 2013), predicted forces of the models here were not sensitive to maximum intrinsic speed  $v_0$  (Figure 3-8). However, predicted forces were sensitive, in a cadence-specific manner, to the curvature  $\alpha$  of the force-velocity relationship. Most notably, models reproduced the estimated forces more closely (higher  $r^2$  and lower RMSE over the pedal cycle) using low  $\alpha$  values at low cadences, but models performed better using higher  $\alpha$  values at high cadences (Figure 3-8 (A)). For a given shortening velocity, lower  $\alpha$ , which actually reflects a higher curvature of the force-velocity relationship (Figure 3-1 (D)), would result in a lower force whereas a higher  $\alpha$  (lower curvature of the force-velocity relationship) would result in a larger force. As mentioned previously, slow fibres are characterized by a higher curvature (lower  $\alpha$ ) whereas fast fibres are characterized by a lower curvature (higher  $\alpha$ ) (Otten, 1987; Umberger et al., 2003). My results suggest that the forces predicted by traditional Hill-type models may be improved by incorporating a force-velocity curvature  $\alpha$  that varies appropriately with type of muscle fibres recruited for the specific mechanical demands of the task— a larger  $\alpha$  for high speed tasks where faster fibres are recruited, and a smaller  $\alpha$  for low speed tasks where slower fibres are recruited. Umberger and colleagues (2003) have previously alluded to this, and have shown that Hill-type models with force-velocity parameters, to include maximum intrinsic speed and curvature of the force-velocity relationship, that are matched to the proportions of slow and fast muscle fibres generate reasonable predictions of whole muscle energetics during isolated muscle contractions, single joint motion and whole body movement.

#### 3.4.5. Limitations

In this chapter, I aimed to determine the ability of two different Hill-type models to reproduce ultrasound-based *in vivo* estimates of force; however, certain experimental limitations should be acknowledged. First, EMG was measured non-invasively using electrodes on the skin surface. However, the surface EMG signal has been shown to

contain distinct frequency characteristics that allow for characterization of recruitment between different types of motor unit using the methods presented here (Wakeling and Rozitis, 2004; Reaz et al., 2006; Wakeling, 2009).

Second, muscle strain has been shown to affect the frequency content of the EMG signal, with longer fibre lengths resulting in lower frequencies (Doud and Walsh, 1995). However I included this as a covariate in the EMG statistical analysis, which removes the strain effect as a confounding factor.

Third, it is also possible that there are errors in my estimates of fascicle and tendon slack lengths. Fascicle slack length depended on the accuracy of the chosen tendon slack length. In Chapter 2, I assessed the sensitivity of the ultrasound-based tendon force estimates to tendon slack length (Dick et al., 2016) and found that small increases in tendon slack length delay the onset of AT force during cycling and decrease the magnitude of predicted force. In Chapter 2 I also demonstrated that force estimates are more sensitive to the tendon length at which the force-length relationship shifts from the toe region (less stiff) to the linear region (more stiff), rather than AT slack length (AT length at the beginning of the toe region). If indeed I did under or over-estimate AT length changes within the toe region, then this would have contributed to errors in AT force estimates throughout the pedal cycle. However the models tested here did not consistently underestimate or overestimate force.

Fourth, I determined stiffnesses for the LG and MG portions of the AT in the isometric protocol at a fixed knee angle. It is possible that at different knee angles, where the relative lengths of the MG, LG, and SOL are altered, we may get a different value of stiffness and thus a different value of muscle force. Future studies should focus on determining the extent to which tendon force-length curves are dependent on joint angle; to my knowledge, this remains unexplored.

Finally, it is likely that digitizing errors of the ultrasound images at higher cadences led to increased error in the estimates of tendon length change and, thus, estimates of muscle-tendon force. The decreased  $r^2$  and increased RSME of modelled *versus* estimated muscle forces at higher cadences, in part, reflects this error.

### 3.5. Conclusions

The overarching aim of this chapter was to determine the accuracy with which Hill-type models of human muscle predict *in vivo* forces during submaximal dynamic tasks. Here, I have shown that models driven with experimentally derived *in vivo* parameters, determined non-invasively, predict the ultrasound-derived time-varying gastrocnemii forces to within 10 % of peak force. Hill-type models are highly relevant where knowledge of the forces produced by skeletal muscle could enhance clinical decision-making for those with neuromuscular and orthopaedic conditions. Yet to date, Hill-type models incorporated within musculoskeletal simulations of movement lack a strong set of validation experiments. As such, their clinical use has been limited. Here, I provide evidence that Hill-type models of human muscle can be as accurate as animal models. I suggest that a two-element model, that allows for flexibility to account for variations in contractile performance and motor unit properties of slow and fast muscle fibres, may be particularly useful for estimating muscle forces in populations with neuromuscular deficits, who often exhibit altered motor unit recruitment patterns (Wakeling et al., 2007; Hafer-Macko et al., 2008).

## Chapter 4.

# Shifting gears: muscle shape changes and force-velocity behaviour in the human gastrocnemius during cycling

### 4.1. Introduction

As muscles shorten during contraction they increase in girth in order to maintain (or nearly maintain) their volume, and this occurs at the level of the myofilament lattice (Williams et al. 2013; Daniel et al. 2013), muscle fibres (Huxley, 1969), muscle fibre bundles (Smith et al. 2011) and whole muscle (Swammerdam, 1758: in Cobb, 2002; Baskin and Paolini, 1967). Muscles can bulge in thickness (the distance between the two aponeurosis) or in width (the distance orthogonal to thickness) (Zatsiorsky and Prilutsky, 2012). Studies have shown that the axial muscle in salamanders undergoes increases in both dorso-ventral thickness and medio-lateral width during myomere shortening (Azizi et al., 2002) and that the lateral gastrocnemius in turkeys increases in thickness and decreases in width during low force contractions (Azizi et al., 2008). Human studies have shown that the gastrocnemii change thickness during both isometric (Maganaris et al., 1998a) and dynamic contractions (Randhawa et al., 2013) and that muscle fascicles undergo transverse expansions during shortening (Wakeling and Randhawa, 2014). These dynamic shape changes have been suggested to play a functional role in modulating the velocities at which fibres shorten. However to date, the functional consequences of *in vivo* shape changes on whole muscle mechanical behaviour during submaximal dynamic tasks remain largely unexplored.

Shape changes of a contracting muscle are tightly linked to the muscle's architecture. In pennate muscles, fascicles shorten and typically rotate to greater pennation angles during contraction (Benninghoff and Rollhäuser, 1952; Gans and Bock, 1965; Otten, 1987; Fukunaga et al., 1997; Randhawa et al., 2013). These fascicle rotations decouple the length changes of the fascicles from the length changes of the whole muscle in a process known as gearing ( $v_{\text{MTU}}/v_f$ ; Azizi et al., 2008). In a muscle-

tendon unit with a compliant tendon, gearing is the product of two components:  $v_{\text{MTU}}/v_{\text{b}}$  and  $v_{\text{b}}/v_{\text{f}}$ , where  $v_{\text{MTU}}$ ,  $v_{\text{b}}$ , and  $v_{\text{f}}$  are the shortening velocities of the muscle-tendon unit, the muscle belly, and the muscle fascicles, respectively (Wakeling et al., 2011). Pennate muscles exhibit gearing values  $>1$ , which means that the whole muscle shortens faster than its constituent fascicles (Azizi and Roberts, 2014). Studies have shown that gearing changes in response to the mechanical demands of the task, thereby allowing fascicles to operate at speeds more favorable for force and power production (Azizi et al., 2008; Wakeling et al., 2011; Randhawa et al., 2013; Azizi and Roberts, 2014). For example, low force contractions have been shown to be associated with high gearing values whereas high force contractions were associated with lower gearing values (Azizi et al., 2008). It has been suggested that the structural and material properties of surrounding connective tissues, such as aponeurosis, play a significant role muscle shape changes, gearing, and the overall mechanical output of skeletal muscles (Azizi et al., 2008; Azizi and Roberts, 2009; Rahemi et al., 2014). However, to date our understanding surrounding this topic has come from experiments performed on isolated muscle *in situ* under maximally active conditions and it is not known whether similar effects occur within intact muscle-tendon units under submaximal dynamic conditions.

Results from finite-element modelling suggests that force plays a critical role in dynamic muscle shape shapes. For example, when fascicles shorten, a component of their force acts to compress the muscle between its superficial and deep aponeuroses (Rahemi et al., 2014). This decrease in muscle thickness inhibits the fascicles ability to rotate, and thus may also reduce gearing. However the association between force, dynamic muscle shape change, and gearing has not been explored *in vivo* under submaximal activity levels.

Our understanding of whole muscle behaviour—to include shape changes and gearing—has largely come from studies in which muscles have been maximally activated under constant lengths and tensions. Yet, the mechanical properties of skeletal muscle are not consistent across varying levels of activation (Rack and Westbury, 1969; Holt et al., 2014; Josephson and Edman 1988; Rassier et al., 1999) or force (Holt and Azizi, 2014). For example, recent evidence suggests that the level of activation modulates the operating velocities of contracting fibres, allowing fibre velocities during locomotion to be

tuned to maximize performance (Holt and Azizi, 2016). Holt and Azizi (2014) have also shown that the fibre force-length curve shifts with changes in muscle activation, and conclude that this is a result of the level of force, rather than solely the result of calcium levels (Rassier et al., 1999). This force dependence is likely related to the internal mechanics and physical properties of the muscle, more specifically, the internal work required to stretch connective tissues for effective force transmission (Holt and Azizi, 2014). A comprehensive understanding of the extent to which both activation and force affect muscle shape change, fascicle shortening velocity, and gearing is important to advance our understanding of *in vivo* muscle function.

The first aim of this study was to establish a comprehensive understanding of how activation and force affect dynamic muscle shape change, to include fascicle shortening velocity, pennation, thickness and gearing, across a wide range of mechanical demands. To address this, *in vivo* experiments were conducted on the human MG during cycling. I altered the mechanical requirements of the task by systematically varying cadence and crank load, and I examined how the MG met these different speed and load requirements by obtaining simultaneous recordings of tendon length, fascicle length, pennation angle, and thickness using B-mode ultrasound, and muscle activation, derived from surface EMG. Cycling is the ideal experimental paradigm to explore the influence of both activation and force on muscle behaviour because we can test a range of mechanical conditions where force and activation can be uncoupled. For example, by altering velocity (cadence) at a fixed load, we can increase activation but keep force (crank load) relatively constant. This is not possible during locomotor tasks such as walking and running because force increases with movement speed. In this chapter I test three specific hypothesis: (i) as load increases, fascicle shortening velocity will increase, fascicle rotation will decrease and the change in muscle thickness will decrease; (ii) as load increases, muscle belly gearing will decrease; (iii) force will have a greater effect than activation on gearing.

Traditional Hill-type models greatly simplify the dynamic shape changes of pennate muscles that may be important in modulating the velocities at which fibres contract. In a traditional Hill-type muscle model (Eq. 3-1), the force generated by a muscle fibre is a function of its activation state, active and passive force-length properties, force-velocity properties, and pennation angle. In this formulation, length and pennation angle are not

related to each other, however within a contracting muscle, length and pennation are tightly linked (e.g. Maganaris et al., 1998a; Randhawa and Wakeling, 2015). In order to account for this, an additional modelling constraint, that relates length and pennation angle, is commonly added to the Hill-type model (Zajac, 1989; Delp et al., 1990; van den Bogert et al., 2011). This geometric constraint allows length and pennation angle to vary during contraction, but assumes that the muscle's thickness remains constant. This constant thickness assumption offers a convenient 1D approach for enforcing a constant volume constraint. However, it is possible to change the relationship between length and pennation angle using a range of geometric models that satisfy 1D, 2D, or 3D constraints and testing these different geometric formulations is one of the main aims of this chapter. To avoid confusion, geometric model (1D, 2D, or 3D) refers to muscle models that describe the relationship between length and pennation integrated within the Hill-type model whereas Hill-type model refers to the traditional formulation (Eq. 3-1), where muscle geometry is not included.

Imaging studies have confirmed that a muscle's thickness, as well as its pennation, can change dramatically *in vivo* (Fukunaga et al., 1997; Kawakami et al., 1998; Maganaris et al., 1998a; Wakeling et al., 2011; Randhawa et al., 2013) and the bulging of pennate muscles during contraction could have implications for the prediction of *in vivo* force (Azizi et al., 2008). For example, when fibers rotate during low-force high-velocity contractions, the fibers shorten slower than the muscle belly (Azizi et al., 2008; Wakeling et al., 2011). In effect, the force-velocity characteristics of the fibres are decoupled from those of the muscle belly (Azizi and Brainerd, 2007). While 1D models allow for gearing, they assume thickness remains constant and thus do not allow gearing to vary for a given fibre length change. Thus muscle models that neglect this variable geometric 'gearing' therefore may underestimate *in vivo* force.

1D models of contracting muscle have recently been shown to be appropriate for predicting pennation angle (Randhawa and Wakeling, 2015), however others have questioned this constant thickness assumption (Zuurbier and Huijing, 1992; 1993; Herbert and Gandevia, 1995). To date, geometric models have been tested under relatively isolated conditions, where the muscle shortens at a constant velocity or load (Randhawa and Wakeling, 2015). However, during locomotion skeletal muscles rarely shorten under

constant speeds and loads, so whether the 1D assumption is also appropriate for submaximal dynamic contractions at a range of mechanical conditions is unclear. 2D and 3D models add varying levels of complexity and allow us to test mechanistic explanations for muscle shape changes and gearing by allowing for aponeurosis stretch and muscle bulging in thickness and width to occur.

The second aim of this study was to determine whether a 1D representation of contracting muscle, which is assumed by traditional Hill-type models, is sufficient to predict time-varying fascicle length and pennation angle for submaximal dynamic contractions at a range of mechanical conditions. To do this I compared estimates of fascicle length and pennation angle predicted by 2D and 3D Hill-type models, similar to those presented in Randhawa and Wakeling (2015), to estimates predicted by a traditional 1D Hill-type model. Models were driven with muscle activation and muscle belly length, determined experimentally. Model predictions of fascicle behaviour (length and pennation angle) and gearing were compared to *in vivo* measurements. I hypothesize that a 3D model, that is able to account for bulging in thickness and in width will better predict fascicle length, pennation angle, and gearing during submaximal dynamic conditions. The combination of *in vivo* muscle lengths, pennation angles, and activations together with multidimensional geometric Hill-type models provides new insights into how the interactions between contractile and elastic machinery affect dynamic muscle shape changes under varied locomotor demands.

## **4.2. Methods**

### **4.2.1. Acquisition of experimental data**

This chapter utilizes data from ten competitive cyclists (6M, 4F; age  $33\pm 6$  years). Briefly, subjects pedalled at a range of conditions while I recorded ultrasound images of the MG muscle belly and muscle-tendon junction (MTJ), the 3D trajectories of 32 LED markers, and surface EMG patterns from 10 muscles (Figure 4-1). In this chapter, I analyzed trials in which subjects pedalled at 9 combinations of cadence and crank torque: 80 r.p.m. at 14 N m, 80 r.p.m. at 26 N m, 80 r.p.m. at 35 N m, 80 r.p.m. at 44 N m, 100 r.p.m. at 13 N m, 100 r.p.m. at 26 N m, 120 r.p.m. at 13 N m, 120 r.p.m. at 24 N m, and

140 r.p.m. at 13 N m, corresponding to crank powers of 115 W, 220 W, 290 W, 370 W, 135 W, 270 W, 165 W, 300 W, and 200 W, respectively. Full details of the cycling protocol are described in the previous chapters, so only a brief overview is provided here.

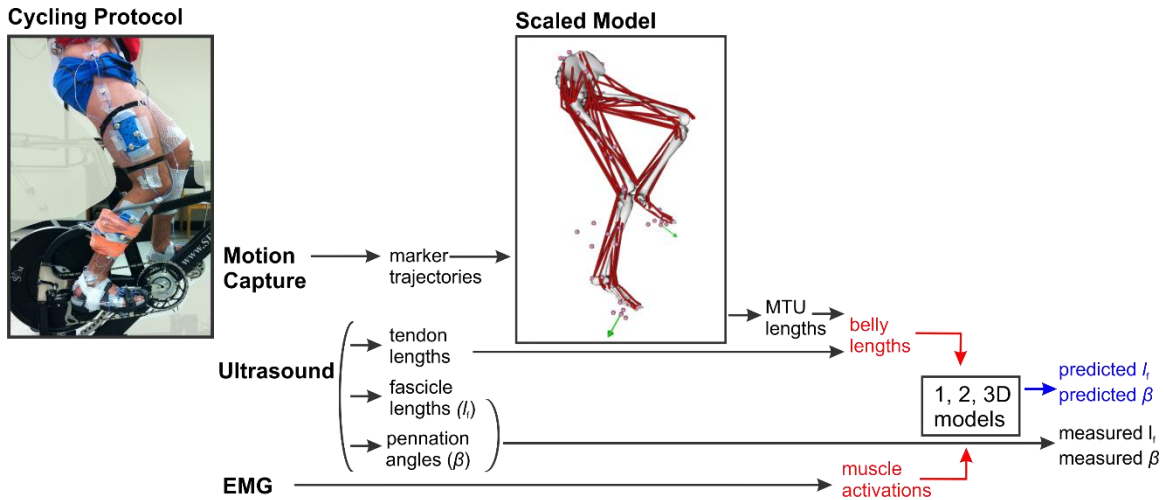


**Figure 4-1. Approach for testing 1D, 2D, and 3D muscle models using experimental data collected during human cycling.**

During the cycling protocol (A), subjects pedalled on a stationary bike while I measured 3D marker trajectories, tendon lengths, fascicle lengths, pennation angles, and surface EMG. A musculoskeletal model (B) was scaled to each subject and was used to calculate the MG muscle-tendon unit (MTU) lengths during cycling. The difference between the time-varying MTU lengths, from the scaled musculoskeletal model, and the tendon lengths, from tracked ultrasound-images was used to determine muscle belly lengths during cycling. Geometric muscle models, of varying dimensions, were driven with the experimentally determined belly lengths and muscle activations. Model predictions of fascicle length and pennation angle were compared against the experimentally measured fascicle lengths and pennation angles. I examined whether models' predictions changed when I allowed the aponeurosis to stretch (2D model), or when I allowed the fascicles to bulge in thickness and width during shortening (3D model).

#### 4.2.2. Analysis of experimental data

Ultrasound images from the muscle belly and MTJ were analyzed to estimate time-varying fascicle lengths, pennation angles, muscle thickness, and tendon lengths during cycling. These methodologies are described in further detail within Chapters 2 and 3. Briefly, the B-mode ultrasound images were manually digitised (ImageJ, NIH, Maryland, USA) to determine fascicle lengths, pennation angles, and muscle thickness (distance between superficial and deep aponeurosis) and were combined with crank angles over 10 pedal cycles for each pedalling trial. These data were fit with a 2 harmonic Fourier series

to estimate average fascicle lengths, pennation angles, and muscle belly thickness during one complete pedal revolution for each subject at each condition.

Ultrasound images from the distal MTJ were manually digitised to estimate time-varying AT lengths during pedalling. AT length was determined by the distance from the 3D coordinates of the AT insertion on the calcaneus (after correcting for LED marker dimensions and skin thickness) to the digitized MG MTJ. AT force was estimated based on the measured AT length changes, tendon stiffnesses, and slack lengths and normalized to the combined maximum isometric force ( $F_{\max}$ ) of the triceps surae muscles determined using the methods presented in Chapter 2 (Dick et al., 2016). These forces were not used within the muscle models.

I estimated the time-varying muscle-tendon unit (MTU) lengths of the MG using a subject-specific scaled musculoskeletal model for each subject together with the experimental LED marker data via inverse kinematics (Figure 4-1) (*OpenSim v3.3*, Delp et al., 2007; Arnold et al., 2010). Time-varying MG muscle belly lengths were calculated as the difference between MTU length, from the scaled musculoskeletal model, and tendon length, from the tracked ultrasound images.

Instantaneous belly velocity  $v_b$  and fascicle velocity  $v_f$  were calculated as the first time-derivative of the changes in  $l_b$  and  $l_f$  respectively. Gearing  $v_b/v_f$  was determined at the time at which belly shortening velocity was maximum. Note that shortening velocities are indicated by negative values.

EMG intensities of the muscles were calculated across a 10 to 450 Hz frequency band using an EMG-specific wavelet analysis (von Tscherner, 2000) and were normalized for each muscle by the maximum intensity detected during the reference cycling trials. Muscle force is linearly related to the EMG amplitude and not its power (Milner-Brown and Stein, 1975), so I used the square-root of the normalized EMG intensity as a measure of muscle excitation  $\hat{e}$ . I used a first-order differential equation to determine normalized muscle activation  $\hat{a}(t)$  from normalized muscle excitations  $\hat{e}(t)$  (Zajac, 1989):

$$\frac{d}{dt}(\hat{a}) + \left[ \frac{1}{\tau_{\text{act}}}(\beta + [1 - \beta]\hat{e}(t)) \right] \hat{a}(t) = \left( \frac{1}{\tau_{\text{act}}} \right) \hat{e}(t) \quad (\text{Eq. 4-1})$$

I used values of 35 ms for the activation time constant  $\tau_{act}$  and 0.6 for the ratio  $\beta$  of the activation to deactivation time constants consistent with chapter 3.

### 4.2.3. Multidimensional muscle models

The three models presented here are Hill-type models, driven with the same muscle activation, length, and velocity for each condition, yet differ in their geometric constraints (Figure 4-2). These models are consistent with those derived in Randhawa and Wakeling (2015); however, in this study models were driven with muscle activations determined from surface EMG and belly lengths  $l_b$  determined from the difference between MTU length, derived from a scaled musculoskeletal model, and tendon length, derived from B-mode ultrasound. Fascicle length  $l_f$  and pennation  $\beta$  were predicted by the 1, 2, and 3D models. The models are presented here using  $l_f$  which can be calculated as:

$$l_f = \frac{l_{apo} - l_b}{\cos \beta} \quad (\text{Eq. 4-2})$$

where fascicle length  $l_f$  is equal to the difference between aponeurosis length  $l_{apo}$  and belly length  $l_b$ , divided by the cosine of pennation angle  $\beta$ .

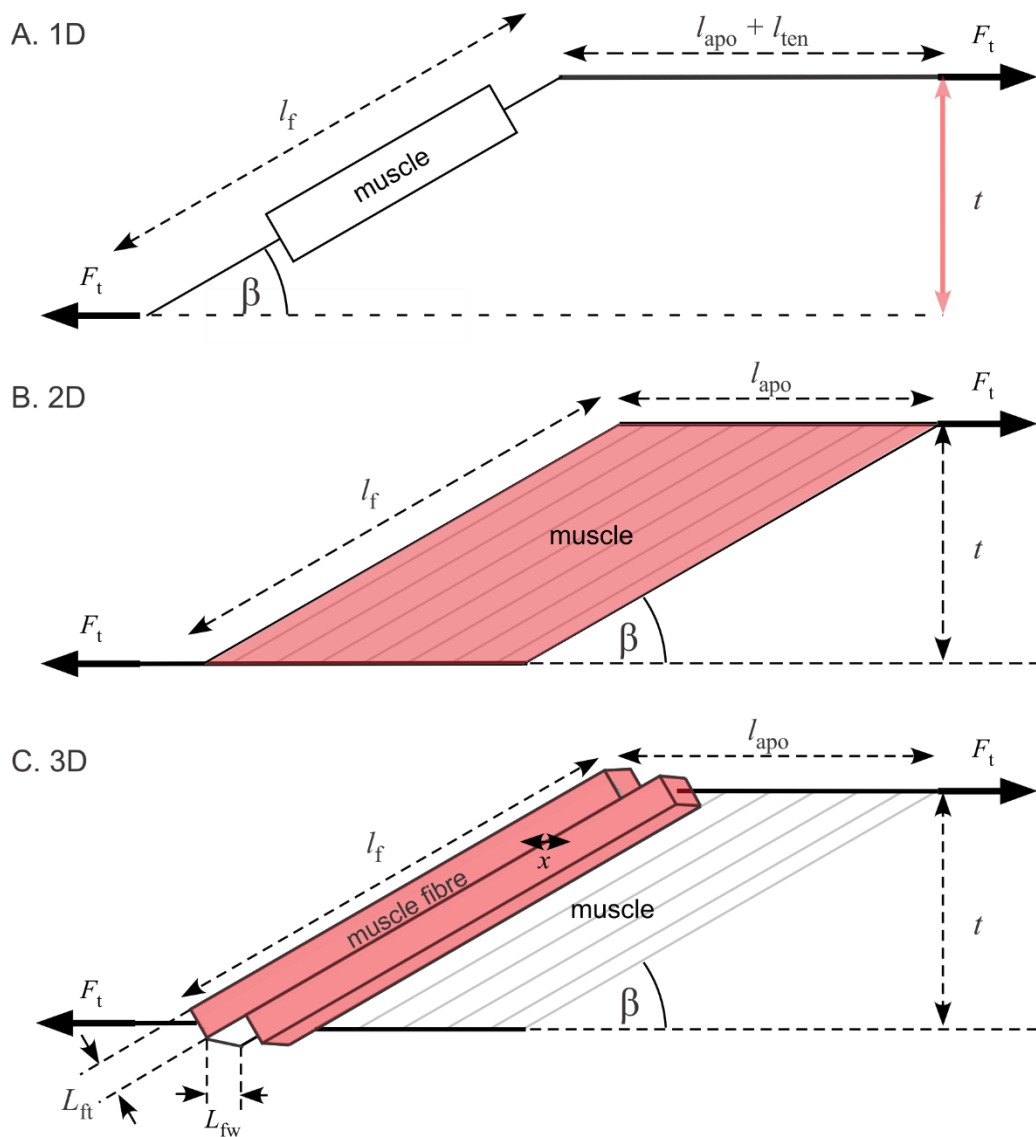


**Figure 4-2. Representation of 1D, 2D, and 3D muscle models.**

The 1D model assumes thickness ( $t$ ) remains constant (A). The 2D model assumes that the area of the muscle remains constant (B). The 3D model assumes that the volume of the muscle fibre remains constant (C). These geometric muscle models are based on those presented in Randhawa and Wakeling (2015).

### 1D Model

The 1D model is based on the traditional Hill-type model (e.g., Zajac, 1989; Delp et al., 1990) where a contractile element is in series with an elastic element (Figure 4-2 (A)). The contractile element represents the muscle fascicle ( $l_f$ ), arranged at a pennation

angle  $\beta$  relative to the force-generating axis of the muscle. In the 1D model, the thickness remains constant, where

$$l_{f,i} \sin \beta_i = l_{f,c} \sin \beta_c \quad (\text{Eq. 4-3})$$

such that current pennation angle  $\beta_c$  and fascicle length  $l_{f,c}$  is entirely dependent on initial pennation angle  $\beta_i$  and initial fascicle length  $l_{f,i}$  and there is only one possible  $\beta_c$  for a given  $\beta_i$  and  $l_{f,i}$  of initial conditions. Initial conditions for  $l_b$ ,  $\hat{a}(t)$ , as well as  $l_f$  and  $\beta$  for each trial were determined from the experimental data at  $270^\circ$  of the crank cycle before the muscle was active and were specific to each subject and condition.

### 2D Model

The 2D model considers the muscle as a panel with pennate fascicles that originate and insert on two parallel aponeuroses in line with the external tendon (Van Leeuwen, 1992) (Figure 4-2 (B)). In the 2D model, the area remains constant, where:

$$l_{f,i} \sin \beta_i l_{\text{apo},i} = l_{f,c} \sin \beta_c l_{\text{apo},c} \quad (\text{Eq. 4-4})$$

The aponeurosis has a compliance  $C_{\text{apo}}$  (represented as strain from 0 to 0.15) and thus can stretch as a function of force. The amount of stretch depends on the fascicle force ( $\hat{F}_f$ ) in the direction of the muscle's line of action. Fascicle force was calculated using a Hill-type model:

$$\hat{F}_f = \hat{a}(t) \hat{F}_a(l_f) \hat{F}_a(v) + \hat{F}_p(l_f) \quad (\text{Eq. 4-5})$$

Where  $\hat{F}_f$  is function of the time-varying activation  $\hat{a}(t)$ , the normalized active and passive force-length relationships  $\hat{F}_a(l_f)$  and  $\hat{F}_p(l_f)$ , respectively, and the normalized force-velocity relationship  $\hat{F}_a(v)$ . The active and passive force-length curves, the maximum intrinsic speed  $v_0$ , and the force-velocity curve used in these models have been previously described in Chapter 3.

The predicted  $\hat{F}_f$  can be used to determine how much the aponeurosis stretches:

$$\frac{l_{apo,c}}{l_{apo,i}} = 1 + C_{apo} \hat{F}_f \cos \beta_c \quad (\text{Eq. 4-6})$$

Combining Eqs. (4-4) and (4-6) gives:

$$\sin \beta_i = \frac{l_{f,c}}{l_{f,i}} \sin \beta_c (1 + C_{apo} \hat{F}_f \cos \beta_c) \quad (\text{Eq. 4-7})$$

### 3D Model

The 3D model considers that muscles can bulge not only in thickness but also in width, and this can be modelled using an additional shape factor  $n$ , which relates the bi-directional bulging of individual fascicles (in the thickness and width dimensions) (Figure 4-2 (C)). In the 3D model, the volume of fascicles (and thus the whole muscle), remains constant to satisfy:

$$\frac{l_{f,c}}{l_{f,i}} \frac{l_{ft,c}}{l_{ft,i}} \frac{l_{fw,c}}{l_{fw,i}} = 1 \quad (\text{Eq. 4-8})$$

where the product of the changes in the normalized dimensions along the fascicles' length  $l_f$ , thickness  $l_{ft}$ , and width  $l_{fw}$  equals 1. Decreases in fascicle length  $l_f$  must be matched by increases in the cross-sectional area of the fascicle, and these changes can occur in thickness and in width. Shape factor  $n$  relates the thickness and width-wise expansion of the fascicles.

$$\left( \frac{l_{ft,c}}{l_{ft,i}} \right)^n = \left( \frac{l_{fw,c}}{l_{fw,i}} \right)^{(1-n)} \quad (\text{Eq. 4-9})$$

The normalized distance between the fascicle centres in the longitudinal direction  $\hat{x}$  (Figure 4-2 (C)) is:

$$\hat{x} = \frac{l_{ft,c}}{l_{ft,i}} \frac{\sin \beta_i}{\sin \beta_c} \quad . \quad 4-10$$

$\hat{x}$  is also the distance between the fascicle centres where they insert onto the aponeurosis, which is the equal to the normalized length of the aponeurosis:

$$\hat{x} = \frac{l_{\text{apo},c}}{l_{\text{apo},i}} = 1 + C_{\text{apo}} \hat{F}_f \cos \beta_c \quad (\text{Eq. 4-11})$$

where the normalized aponeurosis length ( $\frac{l_{\text{apo},c}}{l_{\text{apo},i}}$ ) depends on the aponeurosis compliance ( $C_{\text{apo}}$ ), normalized fascicle force ( $\hat{F}_f$ ), and current pennation angle ( $\beta_c$ ).

Combining Eqs. (4-9), (4-10), and (4-11) gives:

$$\sin \beta_i = \left( \frac{l_{f,c}}{l_{f,i}} \right)^{(1-n)} \sin \beta_c (1 + C_{\text{apo}} \hat{F}_f \cos \beta_c) \quad (\text{Eq. 4-12})$$

Note that this equation becomes a 2D model (Eq. 4-7) if  $n=0$ , whereas if  $n=0.5$ , the fascicle expands equally in thickness and in width during shortening. Alternatively, if  $n=0$  and  $C_{\text{apo}}=0$ , then the aponeurosis cannot stretch, so this equation becomes a 1D model (Eq. 4-3). The mechanical properties and length changes of the external tendon (Figure 4-2 (A)) were not included in any of our models.

#### 4.2.4. Model comparisons

I used the Eq. 4-12 and varied  $C_{\text{apo}}$  from 0 to 0.15, which indicates that the aponeurosis could stretch from 0 % to 15 % at maximum isometric force. I varied  $n$  from -0.2 to 1, which corresponds to the changes fascicle dimensions presented in Table 4-1. While the physiological range for  $C_{\text{apo}}$  has been measured in numerous studies with reported values typically between 1 % and 10 % (Huijing and Ettema, 1988; Ettema and Huijing, 1989; Lieber et al. 1991; Scott and Loeb, 1995; van Donkelaar et al. 1999; Maganaris et al. 2001; Magnusson et al. 2001; Muramatsu et al. 2001, 2002a; Monti et al. 2003; Arampatzis et al. 2006; Azizi and Roberts, 2009), there remains less information on the physiological values for  $n$ . One modelling study reports optimized values of  $n = 0.025$  for the human MG, which corresponds to a 0.25 % increase in fascicle width accompanied by a 9.7 % increase in fascicle thickness for 10 % fascicle shortening (Randhawa and Wakeling, 2015), whereas another finite-element modelling simulation reports values of 7.83 % and 0.74 % for the changes in fascicle width  $l_{f,w}$  and fascicle thickness  $l_{f,t}$ , respectively, which corresponds to an approximate value of  $n = 0.91$  (Rahemi, 2015).

Varying the values of  $C_{\text{apo}}$  and  $n$  beyond the physiological range reported in the literature allowed us to explore 1D, 2D, and 3D models with varying levels of aponeurosis compliance and various combinations of fascicle bulging.

**Table 4-1. Physiological representation of fascicle shape factor  $n$ .**

$n$	$\Delta l_{\text{fw}}$ (%)	$\Delta l_{\text{ft}}$ (%)
-0.2	-2	12
0.025*	0.02	9.7
0	0	10
0.5	5	5
0.91†	7.83	0.74
1	10	0

Values represent changes in fascicle width  $l_{\text{fw}}$  and fascicle thickness  $l_{\text{ft}}$  for a 10 % shortening of the muscle fascicles. Negative values indicate a decrease.

\*Value from Randhawa and Wakeling, 2015.

†Value from Rahemi, 2015.

Models were driven with time-varying belly lengths  $l_b$ , and activations  $\hat{a}(t)$ . In order for models to run, I had to specify initial conditions for  $l_b$ ,  $\hat{a}(t)$ , as well as  $l_f$  and  $\beta$  for each trial. These were determined from the experimental data during pedal upstroke before the muscle was active and were specific to each subject and condition. Models predicted time-varying fascicle lengths  $l_f$  and pennation angles  $\beta$ , and these were compared to the experimentally determined values. I also calculated the models' predicted gearing by taking the first time-derivative of  $l_f$  to calculate predicted  $v_f$ . I characterized differences between the models' predicted muscle parameters  $l_f$  and  $\beta$  and the *in vivo* ultrasound-based measures of  $l_f$  and  $\beta$  across the entire pedal cycle using two measures: the coefficient of determination  $r^2$  and the root mean square error (RMSE). I also compared the predicted gearing to the measured gearing, determined at the time of maximum belly shortening velocity, by calculating the difference between the two values.

#### 4.2.5. Statistics

A general linear model ANOVA was conducted to determine if differences in the experimentally determined muscle parameters (belly shortening velocity, fascicle

shortening velocity, pennation angle, thickness, activation, gearing, tendon strain, and tendon force) existed between the different pedalling conditions (cadence and load), and subject (random factor). A general linear model ANCOVA was conducted to identify significant associations between activation and gearing, tendon strain and gearing, and tendon force and gearing, with fascicle shortening velocity, pennation angle, thickness, tendon force, and activation as covariates. Linear regression was used to determine the association between activation and tendon force and additionally an ANCOVA to determine whether the association (slope of regression lines) between activation and tendon force differed between pedalling conditions with increasing crank load at a constant cadence (80 r.p.m.) and those with increasing cadence at a constant crank load (13-14 N m). Multiple regression analysis was used to determine whether activation or force (independent variables) had a larger effect on each of the dependent variables: maximum belly shortening velocity, maximum fascicle shortening velocity, maximum rate of pennation angle change, change in thickness, and gearing. A general linear model ANOVA was also conducted to determine if differences in the  $r^2$  and RMSE values existed between the 1, 2, and 3D models with subject (random) and pedalling condition as factors. Differences were considered significant at the  $p < 0.05$  level. Data are reported as mean  $\pm$  SE.

### 4.3. Results

During cycling, the MG was active during pedal downstroke. The MTU, muscle belly, and tendon began to lengthen late in the pedal upstroke and began shortening between 90 ° and 130 ° of downstroke. The MG fascicles lengthened and decreased pennation angle during pedal upstroke and then began to shorten and rotate to greater pennation angles near 90 ° of the pedal cycle (Figure 4-3). Muscle belly thickness increased during fascicle shortening. There was a consistent decrease in the maximum belly shortening velocity with increasing crank load at each cadence (Figure 4-4 (A)). Maximum belly shortening velocity ranged from  $-0.24 \pm 0.02 \text{ m s}^{-1}$  at 120 r.p.m. at 13 N m to  $-0.11 \pm 0.004 \text{ m s}^{-1}$  at 80 r.p.m. at 44 N m. Maximum fascicle shortening velocity followed an opposite trend compared to muscle belly shortening velocity and increased with increases in crank load at each cadence (Figure 4-4 (A)). Maximum fascicle

shortening velocity ranged from  $-0.11 \pm 0.01 \text{ m s}^{-1}$  at 80 r.p.m at 14 N m to  $-0.20 \pm 0.01 \text{ m s}^{-1}$  at the highest cadence-lowest load condition, 140 r.p.m. at 13 N m (Figure 4-4 (A)).

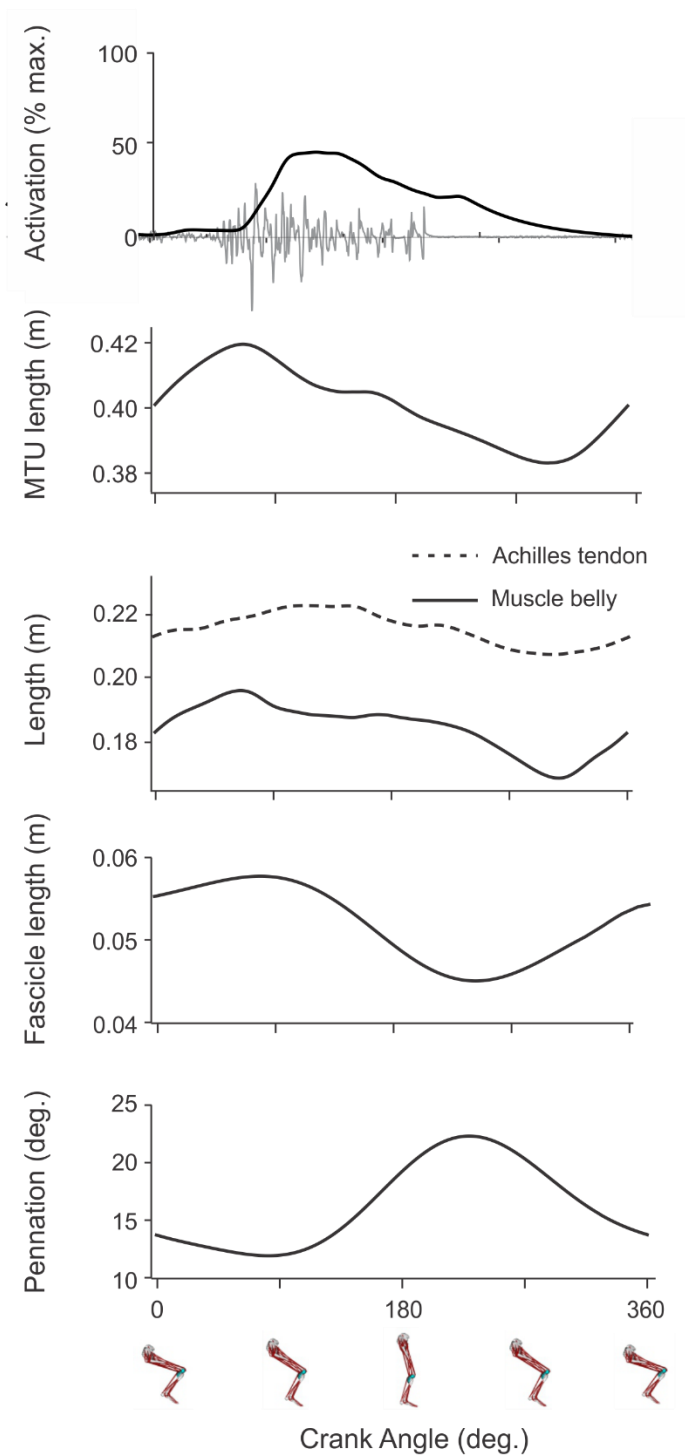


**Figure 4-3. Experimental pedalling data.**

Plots show the time-varying normalized muscle activation with raw EMG recordings from the medial gastrocnemius (MG); muscle-tendon unit (MTU) length; Achilles tendon (AT) length; belly length; fascicle length; and pennation angle over one complete crank cycle. Data are shown for one representative subject pedalling at 80 r.p.m. at 44 N m averaged over 10 pedal cycles.

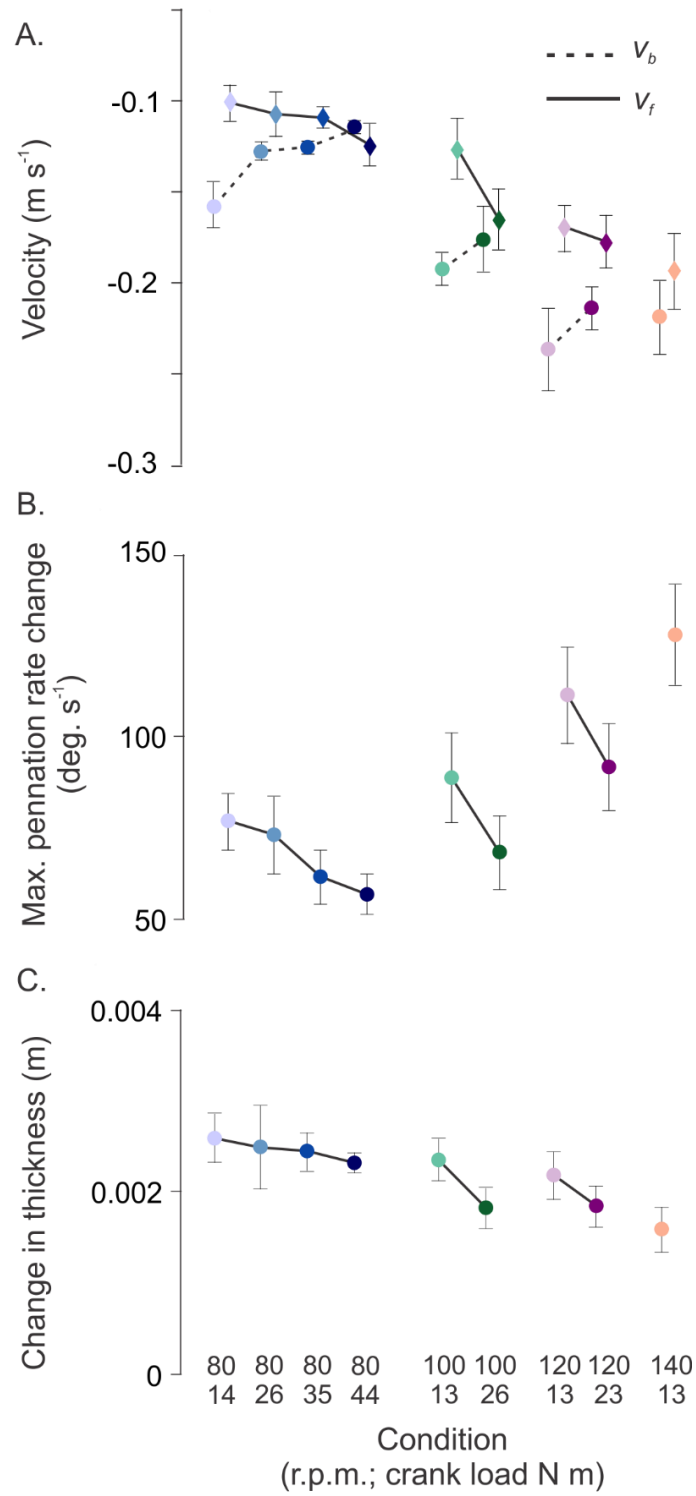


**Figure 4-4. Changes in muscle belly and fascicle behaviour with varying pedalling conditions.**

Variation in maximum muscle shortening velocities (A) rate of pennation angle change (B) and change in muscle thickness (C) at each pedalling condition are presented as mean  $\pm$  SE for 10 subjects. The maximum shortening velocities during pedalling are shown for the muscle belly (circles with dashed lines) and muscle fascicle (diamonds with solid lines) (A).

The measured belly and fascicle shortening velocities were tightly linked to the dynamic muscle shape changes during cycling. For example, the increases in fascicle shortening velocity with increases in load at each cadence ( $p < 0.05$ ) were accompanied by decreases in the rate at which the fascicles rotated within each cadence ( $p < 0.05$ ) (range: 57-128  $^{\circ}$  s $^{-1}$ ) (Figure 4-4 (B)). The changes in muscle thickness (range: 0.0016-0.0026 m) were also related to the associated belly and fascicle velocities. Average muscle thickness was  $0.0153 \pm 0.0016$  m and within each cadence, the change in muscle thickness decreased with increasing crank load ( $p < 0.05$ ) (Figure 4-4 (C)). These results are in support of my first hypothesis. The smallest change in muscle thickness ( $0.0016 \pm 0.0002$  m) occurred at the high cadence-low load condition, 140 r.p.m. at 13 N m (Figure 4-4 (C)).

Muscle activation and gearing varied across cadences and crank loads. Peak muscle activation ranged from 32 % to 45 % (Figure 4-5 (A)). Activation increased with load at each cadence with the lowest activation  $32 \pm 3.1$  % at 80 r.p.m. at 14 N m and the highest activation  $45 \pm 2.7$  % at 80 r.p.m. at 44 N m. However, during the high cadence-low load condition, 140 r.p.m at 13 N m, peak muscle activation also reached relatively high levels ( $45 \pm 3.3$  %). Measured belly gearing varied from  $1.01 \pm 0.09$  to  $1.46 \pm 0.14$  across the range of cadences and loads (Figure 4-5 (B)). The maximum gearing was  $1.46 \pm 0.14$  and occurred at 100 r.p.m. at 13 N m. In support of my second hypothesis, gearing decreased with increasing crank load at each cadence. There was a significant association between activation and gearing, tendon strain and gearing, and force and gearing ( $p < 0.05$ ), suggesting that decreases in gearing were related to the increased muscle activation and force (Figure 4-5).

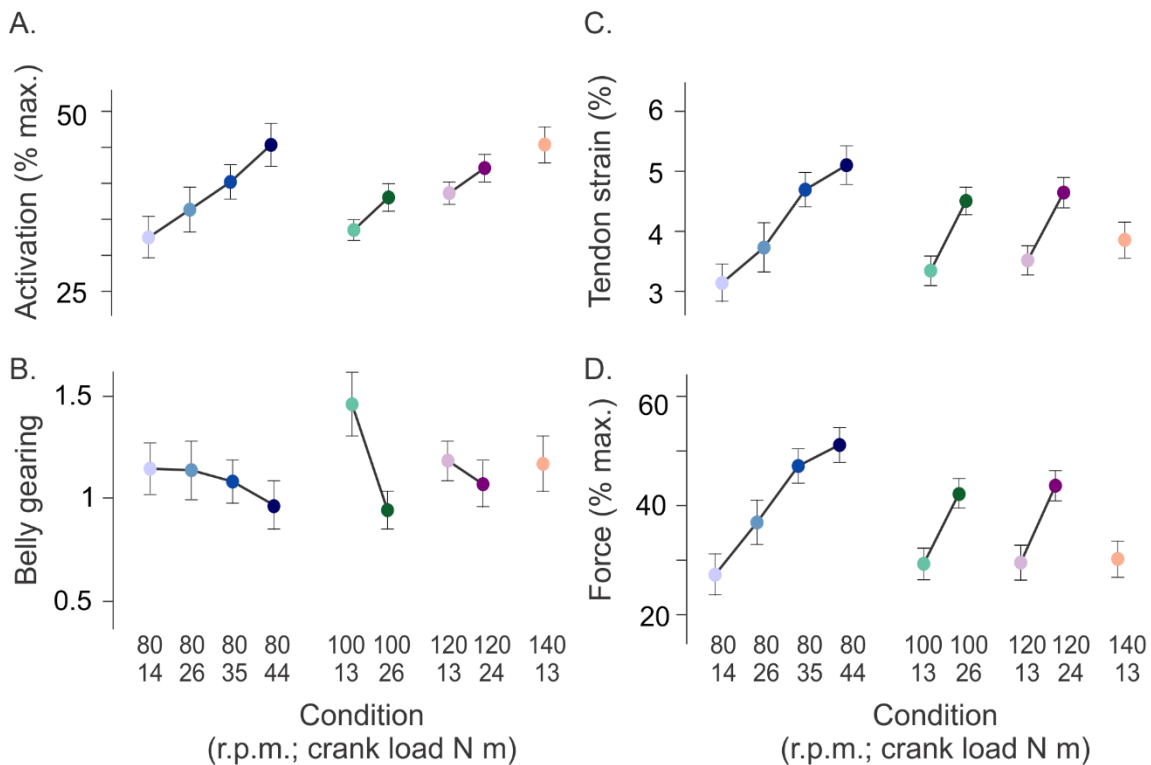


**Figure 4-5. Changes in muscle activation (A), muscle belly gearing (B), tendon strain (C), and tendon force (D) at each pedalling condition.**

Data are presented as mean  $\pm$  SE for 10 subjects. The normalized muscle activations were determined from the surface EMG using wavelet analysis and a first-order differential equation (Zajac, 1989) and normalized to maximum effort pedalling trials (A). The gearing for each trial was calculated as  $v_b/v_f$  (B). Tendon forces were normalized to the  $F_{max}$  of the MG (D).

The increases in activation with load were accompanied by increases in measured tendon strain and estimated tendon force with load at each cadence. On average, peak tendon strains varied from  $3.1 \pm 0.14$  % at the low cadence-low load condition to  $5.1 \pm 0.16$  % at the low cadence-high load condition (Figure 4-5 (C)). Subjects' estimated tendon forces also increased with load. Peak tendon forces ranged from 27-30 % of  $F_{max}$  at the lowest load conditions to 50 % of  $F_{max}$  at the highest load condition (Figure 4-5 (D)).

Across all 9 pedalling conditions, there was a weak association between peak muscle activation and peak AT force ( $r^2=0.29$ ). For example, at the high cadence-low load condition, the MG had a relatively high activation ( $45 \pm 3.3$  %) but low force ( $29 \pm 1.3$  %  $F_{max}$ ), whereas at the low cadence-high load condition, the MG had a relatively high activation ( $45 \pm 2.1$  %) and also a high force ( $52 \pm 1.1$  %  $F_{max}$ ) (Figure 4-5). However when

we separate the pedalling conditions into two distinct groups: (1) 80 r.p.m at increasing crank load from 14 N m to 44 N m and (2) 13-14 N m at increasing cadence from 80 r.p.m to 140 r.p.m., we can observe the independent effects of load (group 1) and cadence (group 2) on the relationship between activation and force (Figure 4-6). These results show that there was a strong association between activation and force within each group (group 1  $r^2=0.94$ , group 2  $r^2=0.92$ ; Figure 4-6). However there was a significant difference between the association of activation and force, as signified by the difference in the slopes, between the two groups (group 1  $m=0.51$ , group 2  $m=6.19$ ; Figure 4-6).

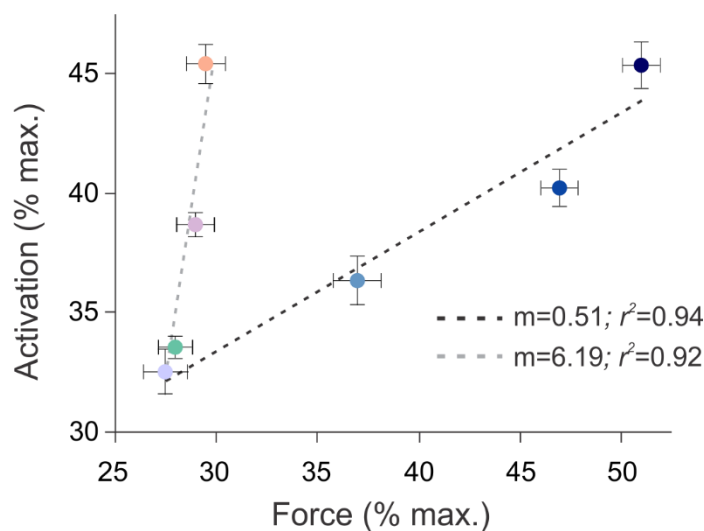


**Figure 4-6. Correlation between muscle activation and tendon force during pedalling.**

Data points represent average peak tendon force normalized to the combined maximum isometric force in the triceps surae muscles (x-axis) versus average peak muscle activation normalized to maximum muscle activation recorded during reference cycling trials (y-axis) for 10 subjects at 7 different pedalling conditions. SE bars are shown for both mean peak activation and mean peak normalized force. Slopes and  $r^2$  values are shown for two groups of pedalling conditions: (1) the four pedalling conditions with a cadence of 80 r.p.m. and increasing crank load from 14 N m to 44 N m (dashed black line) and (2) the four pedalling conditions with crank loads less than 13-14 N m and increasing cadence from 80 r.p.m. to 140 r.p.m. (dashed grey line). Data point colours correspond to the pedalling conditions listed in Figure 4-5.

Results from the multiple regression analysis showed that force was a significant predictor of maximum belly shortening velocity ( $r^2=0.64$ ;  $p<0.05$ ), maximum fascicle shortening velocity ( $r^2=0.59$ ;  $p<0.05$ ), and gearing ( $r^2=0.56$ ;  $p<0.05$ ); however, activation was only a significant predictor for maximum belly shortening velocity ( $r^2=0.58$ ;  $p<0.05$ ).

In support of my third hypothesis, force had a greater effect than activation on gearing. There was no effect of either activation or force with maximum rate of pennation angle change or the change in thickness.

The 1D, 2D, and 3D models tested here were able to capture the time-varying patterns of pennation angle and fascicle length over the complete pedal cycle (Figure 4-7); however, models performed better (higher  $r^2$  and lower RMSE) at low cadences in comparison to high cadences ( $p < 0.05$ ) (Figure 4-7). The 1D model predicted greater pennation angle changes and fascicle length changes in comparison to the 2D and 3D models (Figure 4-7). However, the differences in time-varying predictions of pennation angle and fascicle length were small when  $C_{apo}$  varied from 0.05 and 0.10 within a 2D model, and when  $C_{apo}$  and  $n$  varied from 0.05-0.10 and 0.25-0.50, respectively, within the 3D model. The largest difference in model predictions occurred between the 1D model and the most extreme 3D model where  $C_{apo}=0.1$  and  $n=0.05$  (Figure 4-7).

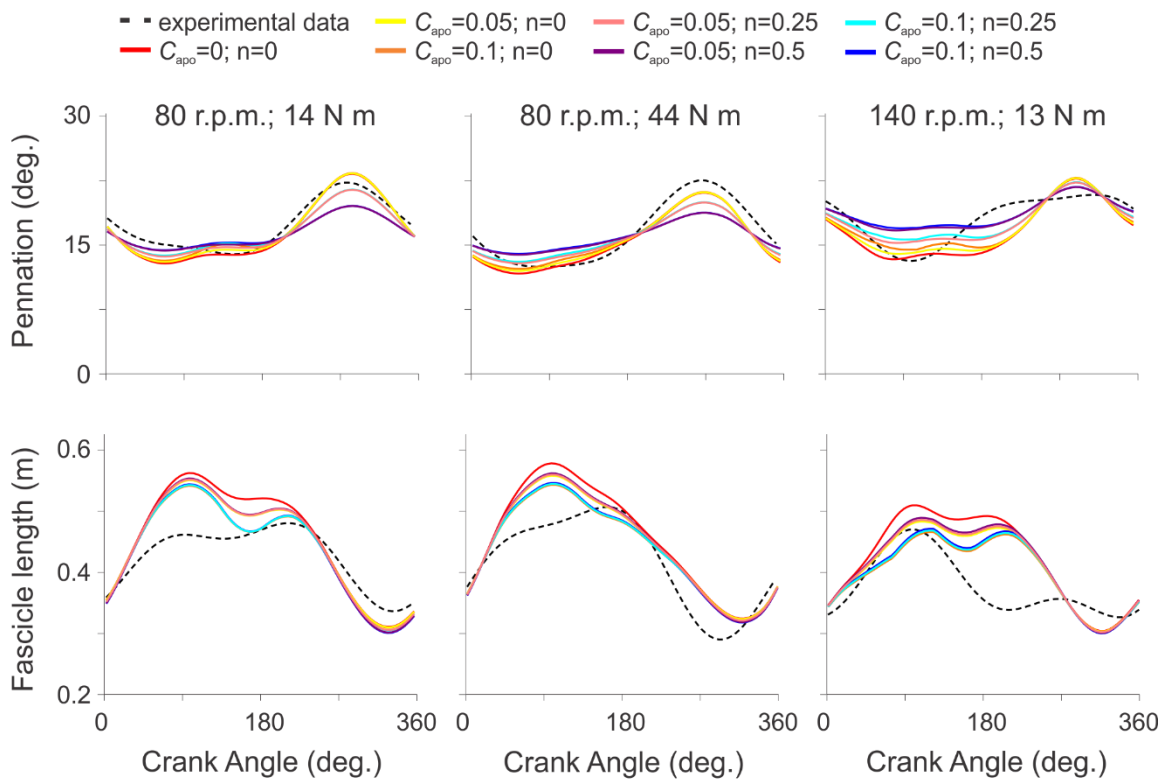


**Figure 4-7. Comparison of experimentally measured and model predicted time-varying pennation angles and fascicle lengths.**

Data are shown for pennation angles (top row) and fascicle lengths (bottom row) measured using ultrasound (dashed black line) and predicted from the 1D, 2D, and 3D Hill-type models (coloured lines) varying the values of  $C_{apo}$  and  $n$  used within each model. Data are shown for one representative subject pedalling at 80 r.p.m. at crank loads of 14 N m and 44 N m and at 140 r.p.m. at 13 N m.

When comparing the predicted time-varying pennation angles and fascicle lengths across the pedal cycle for a 1D model, a 2D model with  $C_{apo}=0.05$ , and a 3D model with  $C_{apo}=0.05$  and  $n=0.5$ , there were no significant differences in the  $r^2$  or RMSE between the 1D, 2D, and 3D model predictions (Figure 4-8). The 1D model predicted the measured changes in pennation angle with an  $r^2$  of  $0.73 \pm 0.019$  and the measured changes in fascicle length with an  $r^2$  of  $0.70 \pm 0.021$ . The 2D and 3D models had  $r^2$  values similar to those of the 1D model:  $0.70 \pm 0.019$  and  $0.72 \pm 0.019$  for pennation angle and  $0.62 \pm 0.024$  and  $0.63 \pm 0.024$  for fascicle length for the 2D and 3D models, respectively (Figure 4-8 (A, B)). RMSE's were similar for the models ranging from  $3.28^\circ$ - $3.39^\circ$  and  $13.4$ - $13.5\%$   $l_0$  for pennation angle and fascicle length, respectively (Figure 4-8 (C, D)). Gearing

predictions between the 1D, 2D, and 3D models were similar, with differences ranging from 0.158-0.165 (Figure 4-8 (E)).

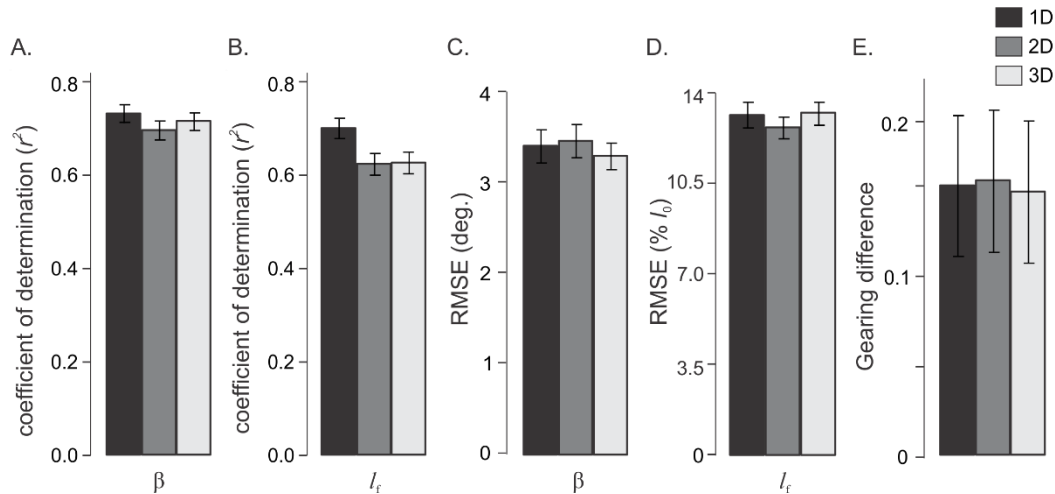


**Figure 4-8.  $r^2$  and RMSE comparing the measured and predicted pennation angle, fascicle length, and muscle gearing.**

$r^2$  and RMSE comparing the measured and predicted pennation angles (A,C), fascicle lengths (B,D) and gearing differences (E) for the 1D ( $C_{apo}=0, n=0$ ), 2D ( $C_{apo}=0.05, n=0$ ), and 3D ( $C_{apo}=0.05, n=0.5$ ) models. Each set of bars represents the 1D (black), 2D (dark grey), and 3D (light grey) model comparisons to the experimentally determined parameters. Each bar represents the average across subjects and pedalling conditions (mean  $\pm$  SE). RMSE for fascicle length was normalized to optimal fascicle lengths. Gearing differences were calculated as the difference between measured gearing and the model predicted gearing. Positive values indicate that experimental gearing was consistently higher than predicted gearing.

When I altered the models' aponeurosis compliance ( $C_{apo}$ ) and fascicle shape factor ( $n$ ), the 1D, 2D and 3D models showed small differences in their ability to predict time-varying pennation angles and fascicle lengths during pedalling.  $r^2$  varied from 0.69 to 0.75 and from 0.61 to 0.69 for pennation angle and fascicle length predictions, respectively, when  $C_{apo}$  varied from 0 to 0.15 and  $n$  varied from -0.2 to 1 (Figure 4-9 (A, C)). RMSE varied from 2.8  $^\circ$  to 3.6  $^\circ$  and 10.4 to 10.6 %  $l_0$  for pennation angle and fascicle length predictions, respectively, when  $C_{apo}$  varied from 0 to 0.15 and  $n$  varied from -0.2 to 1 (Figure 4-9 (B, D)). The 1D models generated similar predictions of pennation angle and fascicle length as compared to 2D models with low aponeurosis compliance ( $C_{apo}$ ) and small values for the fascicle shape factor ( $n$ ). However, consistent with Figure 4-8, the RMSE is lowest for the 3D model predictions of pennation angle (Figure 4-9 (B)) and the

2D model predictions of fascicle length (Figure 4-9 (D)). Overall, the differences between the 1D model, 2D model, and 3D model within the range of  $C_{apo}$  and  $n$  values tested here were small:  $r^2$  for pennation angle=0.04;  $r^2$  for fascicle length=0.06, and RMSE for pennation angle=0.4 °; RMSE for fascicle length = 0.2 %  $l_0$ . The differences in predicted gearing and measured gearing between the 1D, 2D, and 3D models were also small—they varied by 0.008 within the physiological space (Figure 4-9 (E)).

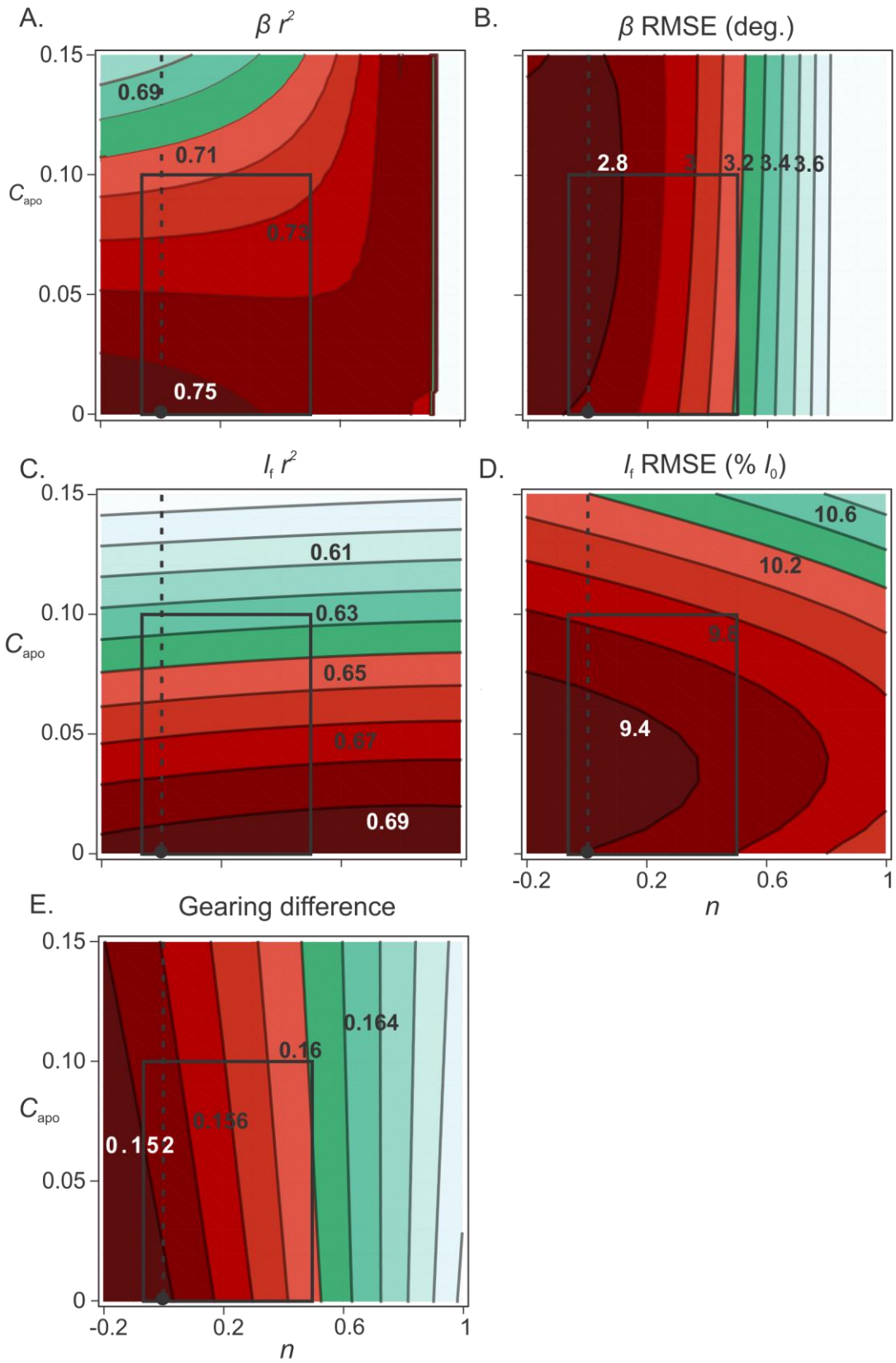


**Figure 4-9. Contour plots comparing the measured and predicted pennation angle, fascicle length, and muscle gearing.**

Contour plots for  $r^2$  (A,C) and RMSE (B, D) comparing experimentally measured and model predicted pennation angles, fascicle lengths, and gearing differences (E) for the range of  $C_{apo}$  and  $n$  values tested. Contour plots show how well the model predictions fit the experimental data when varying  $C_{apo}$  from 0 to 0.15 and  $n$  from -0.2 to 1.0. Darker colours indicate a better fit (higher  $r^2$  or lower RMSE) between the experimental data and model predictions. RMSE for fascicle length was normalized to optimal fascicle lengths. Gearing differences were calculated as the difference between measured gearing and predicted gearing. Positive values indicate that experimental gearing was greater than predicted gearing, with lower values indicating a better fit between model and experimental values. The black circle indicates the position of 1D model; the dashed line indicates 2D models and the box indicates 3D models within physiological range.

#### **4.4. Discussion**

In this study I used ultrasound-based measurements of fascicle length, pennation angle, muscle thickness, and tendon length together with EMG-derived measurements of muscle activation to determine how internal muscle geometry, activation, and force vary across different cadences and loads during human cycling. I showed that the shortening behaviour of muscle fascicles is uncoupled from the shortening behaviour of the whole muscle belly. Specifically, maximum fascicle shortening velocities increased with load, whereas maximum belly shortening velocities decreased. Further, alterations in the shortening velocities were associated with the rate at which fascicles rotated and the changes in muscle thickness during contraction. These alterations in internal muscle geometry and fascicle shortening velocity were linked to the muscles' levels of activation and force. We found that there is likely a larger effect of force, rather than activation, underlying the dynamic muscle shape changes and fascicle velocities during submaximal dynamic contractions. In addition, I used 1D, 2D, and 3D geometrical models, driven with the experimental ultrasound and EMG data, to determine whether the observed changes in the measured fascicle behaviour and gearing could be predicted when using a model that allowed the aponeurosis to stretch and variable muscle shape changes (in thickness and width) to occur. The modelling results showed that 2D and 3D models predict similar fascicle lengths and pennation angles compared to the 1D model suggesting that a traditional 1D Hill-type model that assumes thickness does not change may be sufficient to predict muscle fascicle behaviour during submaximal dynamic tasks.

#### 4.4.1. Dynamic muscle shape changes

Studies have shown that pennate muscles bulge asymmetrically during shortening (e.g.: Azizi et al., 2008; Randhawa et al., 2013; Rahemi, 2015). These shape changes are related to the internal constraints placed on the muscle fibres. When muscle actively shortens, cross-bridges develop forces that act to (1) shorten fibres in their longitudinal direction and (2) compress the myofilaments in their thickness and width directions (Williams et al., 2013). However, muscle fibres are filled with fluid so as fibres shorten, additional forces will develop that oppose these decreases in fibre girth (thickness and width) and will actually cause increases in girth to maintain a (near) isovolumetric state (Rahemi et al., 2014; 2015). These expansions require muscle fibres to rotate to higher pennation angles in order to fit within the same volume. Fibre expansions are also linked to the properties of the aponeurosis and ultimately limited by how much the aponeurosis can stretch (Rahemi, 2015). However these increases in fibre girth will be resisted by additional forces caused by (1) connective tissue sheaths that wrap around muscle fibres which may or may not be anisotropic (Holt et al., 2016) and (2) nearby structures such as bones and neighbouring muscles. These stiffnesses will determine the extent of the changes in muscle fibre shape (thickness and width) and the increases in pennation angle. Modelling studies have shown that asymmetries in fibre bulging must reflect asymmetries in the transverse stresses acting on the fibres (when fibres are considered transversely isotropic; Rahemi et al., 2014; 2015). For example, finite-element models of the gastrocnemii have shown that during shortening contractions, an asymmetric stress distribution will develop across the muscle belly, in particular with a higher compressive force between the superficial and deep aponeuroses. This is in large part due to the longitudinal fibre forces having a component that draws the aponeuroses together, that is not matched by an equivalent compression in the widthwise direction. Therefore the compressive forces during shortening would be greater in the direction bound by the aponeurosis (thickness) in comparison to the width direction where there is no aponeurosis bounding the muscle. This asymmetric stress distribution will tend to cause the fibre deformations to be greater in their width than their thickness direction. Additionally, external forces from other tissues, or even external forces applied to the body will also cause asymmetries in the stress distributions throughout the muscle fibres

(Wakeling et al., 2013). However these will not be apparent in experimental tests of isolated muscle, and thus their effects warrant further investigation.

Thus when a fascicle shortens, it is likely this interplay between the compressive forces and the connective tissue resistance that underlies dynamic muscle shape changes (Azizi et al., 2008; Rahemi et al. 2014; Holt et al., 2016). The changes in muscle thickness and fascicle rotation observed within this study are consistent with the mechanisms put forward in both *in situ* animal studies (Azizi et al., 2008; Holt et al., 2016) and modelling studies (Rahemi et al., 2014; Rahemi, 2015). Specifically, I found a decrease in the change in muscle thickness (smaller increases in muscle thickness during fascicle shortening) and a decrease in fascicle rotation with increasing force. Therefore the ability of fascicles to rotate and operate at high gearing is likely limited in situations where fascicle compressive forces constrain the ability for a muscle to increase in thickness during shortening.

The mechanical properties and behaviour of the aponeurosis have also been suggested to play a key role in modulating dynamic shape changes and internal muscle geometry during contractions (Azizi et al., 2008; Azizi and Roberts, 2009). Longitudinal aponeurosis strains during maximal force contractions reported in the literature vary from from 1 % to 12 % (Huijing and Ettema, 1988; Ettema and Huijing, 1989; Scott and Loeb, 1995; van Donkelaar et al. 1999; Lieber et al. 1991; Maganaris et al. 2001; Magnusson et al. 2001; Monti et al. 2003; Muramatsu et al. 2001, 2002a; Arampatzis et al. 2006; Azizi and Roberts, 2009). When contracting muscles bulge, the aponeurosis not only strains longitudinally, but also transversely (width-wise) (Scott and Loeb, 1995; van Donkelaar et al. 1999; Maganaris et al., 2001; Azizi et al. 2008; Azizi and Roberts, 2009). During active contractions, transverse aponeurosis strains have been reported to reach up to 8 % and these biaxial aponeurosis properties have been suggested to play an important functional role (Azizi and Roberts, 2009). Specifically, they allow the longitudinal aponeurosis stiffness to be modulated by the amount of transverse bulging, thus transmitting more force for a given stretch under certain mechanical conditions (Azizi and Roberts, 2009). In the context of our results, it is plausible that the increases in muscle force which were likely associated with increases in muscle width, given that the change in muscle thickness decreased, would have resulted in greater transverse aponeurosis strains and subsequent

increases in the longitudinal stiffness. Although we did not measure aponeurosis stiffness during pedalling, the theorized increases in longitudinal stiffness is supported by the observed decreases in fascicle rotation rate that occurred with increases in force (Figure 4-4). Again, these experimental results are consistent with previous finite-element modelling studies that reported less fascicle rotation with increases in longitudinal aponeurosis stiffness (Rahemi et al, 2015). There may be additional mechanisms responsible for the decrease in fascicle rotation rate with increases in force. For example, the increase in the component of fascicle force acting to compress the muscle between the aponeurosis, as mentioned previously, would also counter the fascicles tendency to rotate (Rahemi et al., 2014).

#### **4.4.2. Gearing**

Gearing within the gastrocnemii has been looked at in different experimental contexts, however these studies report conflicting results. The gearing results for the MG reported here differ from those reported for the MG, LG, and SOL measured in a previous study during cycling under similar mechanical conditions (Wakeling et al., 2011). In particular, my results show that MG gearing was similar between the low cadence-low load condition and the high cadence-low load condition, whereas it was previously shown that belly gearing in the MG, LG, and SOL increased with increasing cadence (Table 2 in Wakeling et al., 2011). This may be related to the differences in the equipment used (e.g, geometry of indoor cycle ergometer) in the two studies or to differences in the experimental methods used to calculate gearing. Here I directly measured the length changes of the series elastic element using ultrasound, and then estimated time-varying belly lengths as the difference between MTU lengths, derived from kinematics and a scaled musculoskeletal model, and tendon lengths, measured using ultrasound. Previously, Wakeling and co-workers estimated 'projected belly length' from fascicle length changes.

Differences in results between the MG and SOL may be related to differences in muscle architecture between the two muscles. It has been suggested that the SOL has a more complex arrangement of fascicles compared to the MG, comprised of multiple heads with varying fascicle pennation angles (Agur et al., 2003; Rana et al., 2013). My results show that increases in load at a constant cadence were associated with increases in MG

fascicle shortening velocity, decreases in belly shortening velocity, and decreases in gearing. Alternatively, Randhawa and co-workers (2013) found that during isotonic and isokinetic ankle plantarflexion contractions, increases in ankle plantarflexion torque were accompanied by increases in belly gearing, whereas increases in joint rotational velocity were linked to decreases in muscle belly gearing. These results are also in contrast to the increases in belly gearing reported with increases in pedalling speed for the MG, LG, and SOL during cycling (Wakeling et al., 2011). It is difficult to compare these results to those from animal experiments (Azizi et al., 2008; Azizi and Roberts, 2014) because force and speed were not controlled independently.

The variations in gearing during pedalling observed in this study are not solely a result of the changes in fascicle shortening velocity. Changes in gearing are related to alterations in the shortening velocity of the muscle belly. During cycling, it is not possible to maintain constant belly velocity while altering load due to the series elasticity of the AT. Our data show that increases in load at a constant cadence result in decreases in gearing—this is related to the increased fascicle shortening velocity as well as the decreased belly shortening velocity. With increasing loads, the AT underwent larger strains which uncoupled length changes of the MTU from length changes of the muscle belly leading to the observed decrease in belly shortening velocity. This has previously been defined as tendon gearing (e.g., Wakeling et al., 2011).

#### **4.4.3. Activation and force effects**

The relationship between EMG and force during dynamic locomotor tasks is complex. EMG excitation may provide a reliable estimate of muscle force during isometric contractions (Hof, 1984), however additional factors such as muscle length and velocity will drastically influence the force-generating ability of the muscle (Eq. 4-5). For example, the relationship between force magnitude and EMG in running guinea fowl ranges from  $r^2=0.33-0.65$  depending on locomotor speed and muscle (Daley and Biewener, 2003). Within the mechanical conditions elicited here, activation and force were not strongly associated when considering all of the pedalling conditions tested here ( $r^2=0.29$ ), however when separated based on the mechanical conditions of the task, into low cadence-increasing load and low load-increasing cadence groups, there were strong yet different

associations between activation and force between the two groups of pedalling conditions (Figure 4-6). This suggests the mechanical conditions elicited within this study provides an ideal paradigm to test the different effects of both activation and force. For example, the low cadence-high load conditions required the same muscle activation as high cadence-low load cycling but the fascicle velocities were very different; pedalling at 140 r.p.m. required fascicle shortening velocities more than twice as fast the 80 r.p.m. condition (Figure 4-4).

Previous studies in humans have shown that fascicle shortening velocities are uncoupled from whole muscle shortening velocities under a range of locomotor tasks including cycling (Wakeling et al., 2011), running (Farris and Sawicki, 2012), and walking (Arnold et al., 2013). Farris and Sawicki (2012) suggested that the observed shifts in fascicle velocity, to more favorable velocities for force production during the walk to run transition, may serve as a mechanism to reduce muscle activation while maintaining the necessary force output. However EMG was not measured within their study and in fact few studies provide estimates of both *in vivo* force and EMG-derived activations during human locomotor tasks. Our results provide evidence that although activation is linked to muscle shape changes, there is a greater effect of force underpinning the alterations in dynamic muscle shape changes and fascicle shortening behaviour during submaximal dynamic tasks. Others have tested the effect of force on muscle shape change and gearing (e.g., Azizi et al., 2008), however these experiments were performed under maximally active conditions so the effect of activation could not be determined.

#### **4.4.4. Multidimensional Hill-type models**

In this study, I used the 2D, and 3D muscle models to test mechanistic explanations for the observed dynamic shape changes and gearing during human cycling, which are not possible to test with a traditional 1D Hill-type model. I ran 2D and 3D models that spanned, and exceeded the reported physiological values of maximum aponeurosis strain (0-15 %;  $C_{apo}=0-0.15$ ) and fascicle shape factor ( $n=-0.02-1$ ) (Table 4-1). I hypothesized that the 3D model that is able to account for bulging in thickness and in width would better predict fascicle length, pennation angle, and gearing during submaximal dynamic conditions. However, consistent with Randhawa and Wakeling (2015) our results

show that the predictions of 2D and 3D models are similar to the predictions of 1D models under submaximal conditions. Some of the rationale to test these different geometric models was based on previous studies that suggest aponeuroses properties may play an important role in modulating muscle shape changes, fascicle rotations, and fascicle velocities (Azizi et al., 2008; Azizi and Roberts, 2009; Holt et al., 2016).

The differences in the influence of aponeurosis on dynamic muscle shape change and gearing between *in situ* animal experiments (Azizi et al., 2008) and the models tested in this study may be related to experimental differences between the two studies. The MG is closely associated with the neighboring LG and the underlying SOL; it is likely that shape changes and fascicle velocities within the MG depend on external forces applied from surrounding muscles, connective tissues, and bone. In *in situ* experiments, these surrounding structures are typically removed. The influence of the aponeurosis on constraining shape changes is likely greater in an isolated single muscle under maximum activation levels in comparison to an intact submaximally active muscle surrounded by other active and passive tissues. To date, the relationship between muscle properties measured on single muscles *in situ* or *in vitro* and those measured *in vivo* within physiologically intact systems during natural motor tasks remains unclear.

Whilst our knowledge of aponeurosis properties largely comes from studies where the muscle was maximally activated, the influence of aponeurosis properties on dynamic shape changes should be considered within activations relevant to everyday motor tasks. The activations measured here, at relatively high loads and speeds do not exceed 50 %. Although some studies suggest that the aponeurosis may strain by up to 12 %, these high values are potentially related to the experimental methodologies that these studies utilized, and more conservative estimates suggest that it is unlikely for aponeurosis strain to exceed 3 % under maximal activation (Azizi and Roberts, 2009). The activations reported here would have likely resulted in the aponeurosis stretching less than 1.5 %. The differences in pennation angle and fascicle length predicted by a 1D model, where the aponeurosis was unable to stretch, compared to a 2D or 3D model with an aponeurosis compliance of 5 % were small—less than 1 ° and 1 %  $l_0$  for pennation angle and fascicle length, respectively. This suggests that it is unlikely for the aponeurosis to have a large effect on muscle gearing and the resulting mechanical output of a pennate muscle. This

may not be surprising when considering the magnitude of strains that the aponeurosis undergoes in comparison to muscle fascicles. Studies have shown that during walking and running, fascicles shorten up to 30 % (e.g., Lichtwark and Wilson, 2006; Randhawa et al., 2013; Lai et al., 2014), and here we found that during pedalling fascicles shortened between 20 % and 35 % across the range of mechanical conditions. This is nearly 20 times greater than the average aponeurosis stretch we would expect.

When pennate muscle shortens, the aponeuroses slide past each other considerably—this leads to fascicle shortening and changes in pennation angle (fascicle rotations) (Huijing and Woittiez, 1983). The influence of the aponeurosis on the internal muscle geometry (shortening and rotations) is likely only as important as far as the aponeurosis can stretch (approximately 3 %; Azizi and Roberts, 2009), which is less than the amount it slides (approximately 30 % of total muscle belly length change; estimated from the values presented in Table 1 and Figure 4 from Huijing and Woittiez, 1983). Thus, aponeurosis sliding rather than aponeurosis stretch potentially plays a key role in modulating the variations in fascicle shortening velocity and gearing observed here.

The influence of aponeurosis sliding on gearing was first recognized over 30 years ago. Huijing and Woittiez (1983) showed (using a 2D geometric model and experimental data) that during maximum isometric contractions in the rat MG, fibres shorten and rotate due to considerable aponeurosis (defined as tendon plate) sliding. This allowed fibres to undergo smaller length changes than that of the whole muscle belly (i.e.: belly gearing), and operate at more optimal positions on their force-length curve. These results may suggest that the traditional 1D model, where the aponeurosis are able to slide but cannot stretch may be sufficient to predict the variations in fascicle behaviour and gearing. Future work should aim to quantify the association between *in vivo* aponeurosis stretch and sliding on the changes in muscle geometry, gearing, and ultimately the mechanical output of pennate muscle during contraction.

The isovolumetric nature of skeletal muscle during contraction is assumed by nearly all muscle models (e.g., Zajac, 1989; Lee et al., 2013; Millard et al., 2013), including those tested here. And while constant volume has been demonstrated at the level of the muscle fibre (Huxley, 1969) and the myofilament (Elliott et al., 1963), there is evidence to

suggest that fibre bundles (Smith et al., 2011) and whole muscles (Baskin and Paolini, 1967) are not isovolumetric during contraction. Given that even small changes in muscle volume would likely result in significant changes in  $n$ , constant volume models may not be appropriate to understand the mechanisms of dynamic muscle shape change. The nature and importance of potential volume changes on the mechanical behaviour of skeletal muscle warrants further investigation.

#### 4.4.5. Limitations

The results presented here must be considered within the context of the experimental and modelling limitations. In particular, I was unable to constrain the MG contractions to maintain a constant level of force or constant shortening velocity during pedalling and thus was unable to eliminate possible contributions of series elasticity. However, I experimentally measured the length changes of the AT in an effort to understand its contribution to whole muscle-tendon unit behaviour. These experimental conditions are different than those elicited within typical *in situ* experimental preparations, where gearing and shape changes were determined at constant force and constant muscle-tendon unit velocity (Azizi et al., 2009; Azizi and Roberts, 2014). There were some discrepancies between the experimentally determined fascicle lengths and those predicted by the different models (Figure 4-7). The model was driven with muscle belly lengths, determined as the difference between MTU length, estimated from a scaled musculoskeletal model, and tendon length, determined from ultrasound measurements. Experimental fascicle lengths were determined from digitized ultrasound images of the MG muscle belly. It is likely that differences in the timing between tendon length changes and fascicle length changes contributed to this discrepancy between predicted and measured fascicle lengths. The greater discrepancies at the higher cadences (Figure 4-7) may be related to the digitizing errors of ultrasound images at higher cadences. Finally, the experimental fascicle lengths determined from the ultrasound images assumed the fascicles are linear, following paths from the superficial to the deep aponeurosis. But muscle fascicles are in fact curvi-linear (Muramatsu et al., 2002b; Namburete et al., 2011; Rana et al., 2013) which is suggested to be necessary to maintain mechanical stability within the muscle (Van Leeuwen and Spoor, 1992). However, 2D B-mode ultrasound measurements of pennate muscles report errors of less than 6 % for fascicle length

(Muramatsu et al., 2002b) and less than  $1^\circ$  for pennation angle (Rana et al., 2013) when treating fascicles as linear rather than curvi-linear structures, and thus the effects of this assumption are likely minor.

## 4.5. Conclusions

In this study I have shown that during submaximal contractions, dynamic shape changes modulate the force-velocity behaviour in pennate muscle to match the mechanical demands of contraction. The results presented here highlight that activation and force play a critical role in modulating the *in vivo* muscle shape changes that uncouple the force-velocity behaviour of fascicles from the muscle belly—with force having a greater effect.

The implementation of the 1D, 2D and 3D geometric models, together with the Hill-type formulation used in this study is novel. Particularly, models were driven by muscle activations and muscle belly lengths rather than fascicle lengths which allowed us to explore the effects of variable aponeurosis compliance and muscle shape changes on whole muscle behaviour within an intact MTU during submaximal dynamic tasks. Our modelling results showed that a 1D Hill-type model predicted fascicle lengths and pennation angles similar to a 3D model that allowed the aponeurosis to stretch and variable muscle shape changes to occur. This suggests that if the intent of a geometric model is to predict the behaviour of muscle fascicles (length and pennation angle), then a traditional 1D Hill-type model may be sufficient. However 1D models do not allow us to infer the mechanisms by which shape changes influence muscle mechanics. Future work should aim to characterize and better quantify the 3D shape changes of contracting muscle and the effect of these shape changes on *in vivo* muscle function.

## Chapter 5.

### Discussion

#### 5.1. Summary of thesis

The mechanical behaviour of the contractile and elastic machinery within human skeletal muscle-tendon systems during dynamic motor tasks remains in many ways unknown. Direct measurements of *in vivo* muscle forces have been made using invasive procedures (e.g., Gregor et al., 1987; Komi, 1990; Finni et al., 1998) yet these methodologies are not often feasible in typical laboratory or clinical settings. This research provides a novel and alternative non-invasive approach, utilizing experimental tools including B-mode ultrasound, surface EMG, and motion capture, to estimate *in vivo* muscle-tendon forces during dynamic tasks. In particular, in **chapter 2**, I showed that ultrasound-based measures of AT length changes, combined with information about the tendon's stiffness and slack length, can provide estimates of subjects' AT forces and moments that are consistent with subjects' net ankle moments determined from inverse dynamics – but only when the relative EMG intensities of the triceps surae muscles and the subject-specific AT stiffness are considered. Other investigators have speculated that the muscles' activity should be considered when estimating *in vivo* forces transmitted by a complex, composite tendon such as the AT (Gregor et al., 1991; Farris and Sawicki, 2012), and my study provides the first direct evidence that this is indeed the case. The procedure tested and described here offers a non-invasive approach for studying *in vivo* muscle-tendon mechanics in humans and provides comparative data that I can use to test the predictions of muscle models.

Hill-type muscle models are ubiquitous in biomechanical simulations of movement. However, at present, the accuracy with which Hill-type models predict the muscle forces generated by humans remains largely unresolved. Developing independent tests that can validate the predictions of Hill-type models and identify the underlying sources of error remains challenging; however, this thesis provides a unique set of studies to test Hill-type models against *in vivo* estimates of time-varying muscle forces from human subjects.

There are many neuromuscular disorders where the knowledge of individual muscle forces could enhance clinical decision making, providing a scientific basis for decisions regarding the most effective orthopaedic surgery or rehabilitation program for a particular patient. For example, surgeons sometimes lengthen the hamstrings of patients with cerebral palsy (CP) in an attempt to improve their impaired posture and gait (Laracca et al., 2014). However, lengthening the hamstrings can compromise the force-generating ability of these muscles (Arnold et al., 2006). Knowledge of a patient's hamstring's lengths and forces during gait, predicted from a musculoskeletal model, has the potential to aid in decision making; is this particular surgical intervention warranted, and if yes, how much should the hamstrings be lengthened? Another example is in post-stroke patients, whose walking ability is often reduced as a result of impaired muscle excitations that inhibit the force-generating ability of key locomotor muscles. Due to the dynamic coupling of the musculoskeletal system (Zajac, 1993), experiments alone are not fully able to identify the functions of individual muscles, so it is difficult to determine which muscles are most important to target for an effective rehabilitation program. Muscle modelling and simulation techniques can help to quantify individual muscle contributions to walking in an effort to understand the mechanisms of impaired gait in post-stroke patients (e.g., Peterson et al., 2012). However, to date, the ability for clinical scientists to guide treatment planning using models and simulations within individual patients remains limited, in large part, by uncertainties associated with the predictions of muscle force.

The force generated by a contracting muscle depends on its size and architecture, its activation, and the operating lengths and velocities of its contracting fibres. Muscle models predict the forces based on these physiological parameters. Here I experimentally measured many of these key parameters within individual subjects during a range of pedalling cadences and loads, rather than relied on optimized or predicted values. These experimental data provided the necessary measures for us to test the predictions of traditional Hill-type muscle models, and additionally offered a framework to determine whether traditional models could be improved. In this thesis, I used the time-varying *in vivo* forces estimated from the ultrasound-based methods in **chapter 2** to test two particular assumptions of traditional Hill-type models.

First, traditional Hill-type models greatly simplify the potential effects of task-specific variations in the recruitment patterns of slower and faster motor units because they assume single fibre-type properties that are then scaled to represent whole muscle force. In **chapter 3**, I compared gastrocnemii forces predicted by Hill-type models to the forces estimated from ultrasound-based measures of tendon length changes. I tested a traditional model with one contractile element. Additionally, I tested a differential model with two contractile elements that accounted for independent contributions of slow and fast muscle fibres. Both models were driven by subject-specific, ultrasound-based measures of fascicle lengths, velocities, and pennation angles and by activation patterns of slow and fast muscle fibres derived from surface EMG recordings. I found that both models predicted peak gastrocnemii forces within 10 % of the peak forces estimated from ultrasound images. The errors in the predicted and estimated forces were similar to differences obtained from *in situ* and *in vivo* animal studies, where forces were directly measured (Sandercock and Heckman, 1997; Perreault et al., 2003; Wakeling et al., 2012; Lee et al., 2013). Additionally, I showed that a two-element model provided modestly better predictions—in comparison to the traditional one-element model—of the ultrasound-based forces at higher pedalling cadences, because of its ability to account for the increased recruitment of fast fibres that occurs at the higher cadences. This is the first study to test Hill-type models against non-invasive *in vivo* estimates of time-varying muscle forces from human subjects.

Traditional Hill-type models also neglect or greatly simplify the effects of dynamic shape changes within contracting muscles that may be important in modulating the shortening velocity and mechanical output of muscle fascicles. In **chapter 4** I compared time-varying estimates of fascicle length and pennation angle predicted from a traditional Hill-type model, which is 1D and assumes muscle thickness remains constant, to the predictions of 2D and 3D geometric representations of the Hill-type model that allowed for aponeurosis stretch and dynamic muscle shape changes to satisfy constant area and constant volume constraints, respectively. I showed that 2D and 3D models predict similar fascicle lengths and pennation angles compared to the 1D model. This suggests that although a 1D model provides little use if we want to better understand the mechanisms of how internal muscle geometry and shape changes are linked to muscle mechanics and *in vivo* muscle function, it is likely sufficient to predict muscle geometry with reasonable

confidence under submaximal conditions. The experimental results presented within Chapter 4 were particularly interesting. I provided experimental evidence to support the suggested mechanisms of dynamic shape change from modelling and experimental studies (Azizi et al., 2008; Rahemi et al., 2014; 2015). I showed that the maximum shortening velocity of the fascicle and muscle belly change in an opposite manner when the mechanical demands of the task are altered, and these changes were tightly linked to the level of muscle activation and force. I have provided a comprehensive understanding of how force and activation affect dynamic muscle shape changes and the *in vivo* operating lengths and velocities of contracting muscle fibres during a range of mechanical conditions. To my knowledge, this is the first study to (i) explore the relationship between activation, force, and dynamic muscle shape changes on the mechanical performance of human skeletal muscle and to (ii) test the predictions of the multidimensional Hill-type muscle models, driven with *in vivo* experimental data, under submaximal dynamic conditions. Recent evidence suggests that the level of force has substantial effects on a muscle's *in vivo* operating lengths (Holt and Azizi, 2014). However these ideas remain unexplored within intact muscles during *in vivo* motor behaviours. Identifying these mechanisms, such as the effect of force on 3D dynamic muscle shape changes and fascicle behaviour, is necessary if we are to understand how muscle functions to power locomotor tasks.

## **5.2. Using *in vivo* experimental data to inform muscle models**

Integrating subject-specific measures of muscle-tendon properties obtained from ultrasound imaging into models of the musculoskeletal system has the potential to improve our understanding of muscle-tendon function during both normal and pathological movement (Passmore et al., 2016). This approach also allows for rigorous comparison studies to quantify the ability of existing musculoskeletal simulations to predict muscle force, which to date remains unknown. Here I provide a set of benchmark data to test the predictions of dynamic musculoskeletal simulations. In particular, ultrasound imaging can provide subject-specific measurements of fascicle lengths, pennation angles, muscle thickness, tendon lengths, and tendon stiffness—all of which I have directly measured

within this research. Further, this thesis highlights the importance of obtaining simultaneous EMG recordings. For example, in **chapter 2** I showed that the forces transmitted by the composite AT depends on the relative EMG excitations of the triceps surae muscles. In **chapter 4**, I found that due to the force-velocity effects, the relationship between muscle activation and force is not consistent across a wide range of mechanical conditions. Together, these findings illustrate that measurements of muscle length alone may be misleading without obtaining similar measurements of muscle excitation, or vice versa, but when collected together, we can begin to understand the integrated neural and mechanical behaviour of skeletal muscle.

Very few studies have attempted to incorporate ultrasound-measured muscle-tendon properties within subject-specific models of the human musculoskeletal system—and those that have are limited to relatively constrained single joint motions. Gerus et al. (2012) utilized ultrasound to derive subject-specific force-strain relationships for the free tendon and aponeurosis of the ankle plantarflexors and showed that incorporating subject-specific measurements within a muscle model resulted in better agreement with ankle joint moments compared to a model that utilized a generic tendon force-strain relationship. The same group also demonstrated that combining ultrasound-based tendon force-strain relationships together with initial muscle fascicle geometry determined using ultrasound further improved the accuracy of their predicted net ankle joint torques during fixed-end contractions in comparison to models that were not given initial fascicle geometry (Gerus et al., 2013).

The use of subject-specific input parameters into muscle models is likely even more important for individuals who display altered muscle-tendon properties as a result of pathology. Li and co-workers (2009) found large errors when comparing model predictions to *in vivo* measurements of fibre length, pennation angle, and maximum muscle stress between stroke patients and generic cadaveric data, but model predictions improved when muscle-tendon parameters specific to the stroke patients were included within the models.

In addition to acquiring input parameters for subject-specific muscle models, ultrasound imaging is useful to compare model predictions of muscle-tendon lengths and muscle forces. For example, muscle models commonly utilized within whole body

simulations (e.g., Delp et al., 2007) constrain the operating lengths, velocities and angles of the contracting fibres and tendon based on the assigned force-length and force-velocity properties. *In vivo* measurements, such as those collected, analyzed and reported in this thesis, can be particularly useful as an independent means of verifying the ability of musculoskeletal simulations to capture the *in vivo* behaviour of muscle and tendinous tissues. Few studies have compared fascicle and tendon length changes and operating regions predicted from musculoskeletal simulations to those measured using ultrasound during walking, running (Arnold et al., 2013; Lai et al., 2014), and hopping (Farris et al., 2013). In general, these studies showed that model-derived fibre lengths operated on similar regions of the force-length curve during walking and running as compared with the experimental results. Thus, ultrasound imaging provides a non-invasive, practical tool for evaluating the predictions of muscle models during movement. However, to my knowledge no previous study has compared the forces predicted by muscle models to *in vivo* forces estimated from tracked ultrasound images. Therefore, this research provides the next logical, yet critical step in advancing the utility of musculoskeletal models. Here I have directly compared muscle models, driven with *in vivo* ultrasound and EMG-based parameters to predicted muscle-tendon forces.

Integrating comprehensive sets of high-quality experimental data with advanced muscle models implemented within whole body musculoskeletal models allows the potential to both test and improve the accuracy with which current models predict force. However one major barrier to this is that many laboratories collect comprehensive datasets or develop their own models and simulations, and do not make these available to others. Therefore it remains difficult for the biomechanics field to make great advances. Collecting comprehensive datasets and developing models and dynamic simulations of movement is technically challenging—many laboratories lack the resources and necessary equipment or the technical expertise to do both. Since 2007, when *OpenSim*—an open-source platform for the biomechanics community to analyze, test, and exchange models and simulations (Delp et al., 2007)—was first released, great strides have been made within this regard. However models and simulations are still limited as they lack validation and comparison studies, which has prevented their use in clinical practice and ultimately their ability to have a broader impact (Hicks et al., 2015). In order to move forward as a biomechanics community, a collaborative approach between research

groups with expertise in biomechanics, engineering, computer science, physiology, and medicine is vital.

### **5.3. Application to clinical research**

The mechanical behaviour of skeletal muscle, specifically its ability to change length and produce force, contributes not only to function of the musculoskeletal system, but maybe of even greater importance, to dysfunction. Clinicians frequently measure the EMG signals, joint angles, and ground reaction forces of patients in an effort to design effective rehabilitation programs to improve mobility. However, these data are rarely analyzed using modern computational tools that can elucidate the recruitment patterns of motor units or identify the dynamic actions of individual muscles. Modelling and simulation of the human musculoskeletal system shows great promise for improving the diagnosis and treatment of the many conditions that limit human mobility. Despite this great promise, modelling and simulation have yet to be applied widely in clinical practice, in large part due to the previously mentioned gaps in validating these models to ensure their accuracy and reliability (Hicks et al., 2015). Although this thesis integrates *in vivo* measurements of muscle and tendon together with muscle models in a group of elite cyclists, this is the first step towards testing the predictive accuracy of Hill-type models that have broad application to the diagnosis and treatment of neuromuscular disorders and their associated movement abnormalities.

One neuromuscular disorder that is commonly studied using B-mode ultrasound, EMG, and muscle models is cerebral palsy (CP). CP is the most common childhood movement disorder and is characterized by impaired locomotor ability (Yeargin-Allsopp et al., 2008). For example, children with CP commonly walk in a crouch gait pattern characterized by excessive flexion of the hip, knee, and ankle during the stance phase of gait. Ultrasound studies have shown that individuals with CP have relatively smaller and weaker muscles (Barber et al., 2011a), stiffer fascicles (Barber et al., 2011b), reduced muscle-tendon unit lengths (Huijing et al., 2013) and longer AT slack lengths (Barber et al., 2012) in comparison to healthy control subjects. EMG studies have shown that children with CP have a reduced number of muscle synergies, indicating that CP patients use simplified motor control strategies (Steele et al., 2015). In addition, wavelet-based EMG

frequency analysis has shown that muscle dysfunction in children with CP is related to altered motor unit recruitment strategies, with greater muscle dysfunction in distal as compared to proximal muscles (Wakeling et al., 2007). Groups have developed muscle models, with modified properties to represent, for example, the spasticity characteristic displayed within CP muscle (Van der Krogt et al., 2013). These models can be incorporated within subject-specific simulations of movement to better understand the mechanistic determinants of impaired locomotor patterns within CP patients. However, rigorous validation and comparison between the forces predicted by modified Hill-type models is necessary in order to be confident in predictions of musculoskeletal simulations.

Although not directly targeted at CP, the refined Hill-type models presented in this thesis have a direct translation to CP research. For example, the methods presented in **chapter 2** could be directly applied to individuals with CP, and when coupled with the advanced EMG processing techniques and the two-element Hill-type model presented in **chapter 3**, I can begin to understand how altered muscle and tendon mechanical properties as well as altered motor unit recruitment strategies, which occur together in CP, contribute to locomotor dysfunction. Further, to my knowledge, there is yet to be a study that has determined how dynamic muscle shape changes are altered in children with CP. Yet, given the evidence of altered passive properties due to connective tissue elements (Booth et al., 2001), it is likely that the ability of CP muscle to undergo dynamic shape and length changes is restricted or modified in comparison to healthy muscle. When applied to individuals with CP, the experimental methodologies presented in **chapter 4** have the potential to provide mechanistic explanations for the impaired mechanical output of CP muscle. Yet these ideas remain largely unexplored. Future work should focus on integrating *in vivo* ultrasound and EMG derived inputs into refined Hill-type models, targeted directly towards CP populations.

#### **5.4. Modelling human muscle force: where are we now, where are we going?**

In this thesis, I have developed novel experimental methods to test traditional and modified Hill-type muscle models against *in vivo* estimates of force, derived from ultrasound measurements of tendon strain. However, even when accounting for

independent contributions of slow and fast muscle fibres and allowing for aponeurosis compliance and dynamic muscle shape changes, Hill-type models are still only able to explain between 30 and 80 % of the force generated by skeletal muscle during submaximal dynamic tasks. These results may seem discouraging, however they also present an exciting future for the biomechanics community. Skeletal muscle is complex, and its *in vivo* behaviour during everyday submaximal dynamic locomotor tasks remains largely unknown. Despite the relatively conserved nature of skeletal muscle in terms of the molecular mechanisms responsible for force production (Schiaffino and Reggiani, 1996), there are still differences in the properties of the contractile and elastic machinery across muscles and organisms that remain poorly understood. These complexities are challenging to address because we still know little about differences in the mechanical behaviour of skeletal muscle within an experimental environment *versus* the natural world as well as the differences between isolated muscles fibres *versus* whole muscles within intact biological systems. There are likely numerous skeletal muscle phenomena that emerge within an intact muscle-tendon unit of a moving animal that remain unexplained because they have not yet been characterized. However, the experimental tools presently available provide optimism that it is only a matter of time before we will be able to characterize, understand, and explain these phenomena.

So then do we need to be more sophisticated in how we model muscle forces? The answer to this question largely depends on the particular aim of one's research. Sometimes, simple models are adequate, if not preferred. The best models are simple models that make few assumptions but can still explain a large amount of data (Robinson, 1977). For example, the dynamics of walking—a locomotor process that involves the coordination of numerous muscles across multiple joints with varying degrees of freedom—can largely be explained by a much simpler passive inverted pendulum model (McGeer, 1990). However if my goal is to determine how altered motor unit recruitment patterns, spasticity, and dynamic muscle shape changes contribute to the impaired force-generating ability of the medial gastrocnemius in a child with CP, then the answer is yes, the complexity of my model would need to increase in order to understand the mechanisms of impaired function as well as improve the predictions of *in vivo* muscle force. However, with advances in the technologies available—to include shear-wave ultrasound imaging, automated processing techniques, high contrast cine-phase MRI,

XROMM, as well as marked improvements in the processing abilities of modern day computers—this is a realistic approach.

To conclude, muscle models that enable accurate and reliable assessment of *in vivo* motor function, rigorously tested against high-quality experimental data, have broad application to human health and life-long mobility. In this thesis, I have developed an innovative set of Hill-type models, driven with subject-specific *in vivo* data, and for the first time, directly compared the predictions of Hill-type models driven with experimentally determined muscle lengths, velocities, pennation angles, and activation patterns against *in vivo* estimates of muscle-tendon forces in human subjects. This thesis provides novel experimental techniques integrated within new-age Hill-type muscle models that account for differences in recruitment patterns between slow and fast fibres and dynamic muscle shape changes, as well as a comprehensive set of experimental data that will enable future studies to test the predictions of whole body dynamic musculoskeletal simulations.

## References

- Ackland, D. C., Lin, Y. C. and Pandy, M. G.** (2012). Sensitivity of model predictions of muscle function to changes in moment arms and muscle–tendon properties: A Monte-Carlo analysis. *J. Biomech.*, **45**, 1463-1471.
- Agur, A. M., Ng-Thow-Hing, V., Ball, K. A., Fiume, E. and McKee, N. H.** (2003). Documentation and three-dimensional modelling of human soleus muscle architecture. *Clin. Anat.*, **16**, 285-293.
- Alexander, R. M.** (1988). *Elastic mechanisms in animal movement*. Cambridge: Cambridge University.
- Alexander, R. M.** (1992). *Mechanics of animal locomotion*. Berlin: Springer-Verlag.
- Alexander, R. M. and Vernon, A.** (1975). The dimensions of knee and ankle muscles and the forces they exert. *J. Hum. Mov. Stud.*, **1**, 115-123.
- Anderson, F.C. and Pandy, M.G.** (1999). A dynamic optimization solution for vertical jumping in three dimensions. *Comput. Methods Biomech. Biomed. Engin.*, **2**, 201-31.
- Anderson, F.C. and Pandy, M.G.** (2003). Individual muscle contributions to support in normal walking. *Gait Posture*, **17**, 159-69.
- Arampatzis, A., De Monte, G., Karamanidis, K., Morey-Klapsing, G., Stafilidis, S. and Bruggemann, G.P.** (2006) Influence of the muscle-tendon unit's mechanical and morphological properties on running economy. *J. Exp. Biol.*, **209**, 3345–3357.
- Arnold, A. S., Liu, M., Ounpuu, S., Swartz, M., and Delp, S. L.** (2006). The role of estimating hamstrings lengths and velocities in planning treatments for crouch gait. *Gait Posture*, **23**, 273-281.
- Arnold, E.M., Ward, S.R., Lieber, R.L. and Delp, S. L.** (2010). A model of the lower limb for analysis of human movement. *Ann. Biomed. Eng.*, **38**, 269-279.
- Arnold, E. M., Hamner, S. R., Seth, A., Millard, M. and Delp, S. L.** (2013). How muscle fiber lengths and velocities affect muscle force generation as humans walk and run at different speeds. *J. Exp. Biol.*, **216**, 2150-2160.
- Ashley, C. C. and Ridgway, E. B.** (1968). Simultaneous recording of membrane potential, calcium transient and tension in single muscle fibres. *Nature*, **219**, 1168-1169.

- Askew, G.N. and Marsh, R.L.** (1998). Optimal shortening velocity ( $V/V_{max}$ ) of skeletal muscle during cyclical contractions: length-force effects and velocity-dependent activation and deactivation. *J. Exp. Biol.*, **201**, 1527-1540.
- Azizi, E., Gillis, G. B. and Brainerd, E. L.** (2002) Morphology and mechanics of myosepta in a swimming salamander (*Siren lacertina*). *Comp. Biochem. Phys. A.*, **133**, 967-978.
- Azizi, E. and Brainerd, E.L.** (2007). Architectural gear ratio and muscle fiber strain homogeneity in segmented musculature. *J. Exp. Zool. A Ecol. Genet. Physiol.*, **307**, 145-55.
- Azizi, E., Brainerd, E. L. and Roberts, T. J.** (2008). Variable gearing in pennate muscles. *PNAS*, **105**, 1745-1750.
- Azizi, E. and Roberts, T. J.** (2009). Biaxial strain and variable stiffness in aponeuroses. *J. Physiol.*, **587**, 4309-4318.
- Azizi, E. and Roberts, T. J.** (2010). Muscle performance during frog jumping: influence of elasticity on muscle operating lengths. *Proc. R. Soc. B*, **277**, 1523-1530.
- Azizi, E. and Roberts, T. J.** (2014). Geared up to stretch: pennate muscle behavior during active lengthening. *J. Exp. Biol.*, **217**, 376-381.
- Barber, L., Barrett, R. and Lichtwark, G.** (2009). Validation of a freehand 3D ultrasound system for morphological measures of the medial gastrocnemius muscle. *J. Biomech.*, **42**, 1313-1319.
- Barber, L., Hastings-Ison, T., Baker, R., Barrett, R. and Lichtwark, G.** (2011a). Medial gastrocnemius muscle volume and fascicle length in children aged 2 to 5 years with cerebral palsy. *Dev. Med. Child Neurol.*, **53**, 543-548.
- Barber, L., Barrett, R. and Lichtwark, G.** (2011b). Passive muscle mechanical properties of the medial gastrocnemius in young adults with spastic cerebral palsy. *J. Biomech.*, **44**, 2496-2500.
- Barber, L., Barrett, R. and Lichtwark, G.** (2012). Medial gastrocnemius muscle fascicle active torque-length and Achilles tendon properties in young adults with spastic cerebral palsy. *J. Biomech.*, **45**, 2526-2530.
- Baskin, R. J., Paolini, P. J.** (1967). Volume change and pressure development in muscle during contraction. *Am. J. Physiol.-Legacy Content*, **213**, 1025-1030.
- Baum, B.S. and Li, L.** (2003). Lower extremity muscle activities during cycling are influenced by load and frequency. *J. Electromyogr. Kinesiol.*, **13**, 181-190.

- Benninghoff, A. and Rollhäuser, H.** (1952). Zur inneren Mechanik des gefiederten Muskels. *Pflugers Arch.* **254**, 527-548.
- Biewener, A.A.** (1989). Scaling body support in mammals: limb posture and muscle mechanics. *Science*, **245**, 45-48.
- Biewener, A. A.** (1998a). Muscle function in vivo: a comparison of muscles used for elastic energy savings versus muscles used to generate mechanical power. *Amer. Zool.*, **38**, 703-717
- Biewener, A. A.** (1998b). Muscle-tendon stresses and elastic energy storage during locomotion in the horse. *Comp. Biochem. Physiol. B Biochem. Mol. Biol.*, **120**, 73-87.
- Biewener, A. A., Corning, W. R. and Tobalske, B. W.** (1998a). In vivo pectoralis muscle force-length behavior during level flight in pigeons (*Columba livia*). *J. Exp. Biol.*, **201**, 3293-3307.
- Biewener, A. A., Konieczynski, D. D. and Baudinette, R. V.** (1998b). In vivo muscle force-length behavior during steady-speed hopping in tammar wallabies. *J. Exp. Biol.*, **201**, 1681-1694.
- Biewener, A. A. and Roberts, T. J.** (2000). Muscle and tendon contributions to force, work, and elastic energy savings: a comparative perspective. *Exerc. Sport Sci. Rev.*, **28**, 99-107.
- Biewener, A. A.** (2003). *Animal locomotion*. Oxford: Oxford University Press.
- Blake, O. M. and Wakeling, J. M.** (2014). Early deactivation of slower muscle fibres at high movement frequencies. *J. Exp. Biol.*, **217**, 3528-3534.
- Blix, M.** (1894). Die Länge und die Spannung des Muskels. *Skandinavisches Archiv Fur Physiologie*, **5**, 173-206.
- Blok, J.H., Stegeman, D.F. and van Oosterom, A.** (2002). Three-layer volume conductor model and software package for applications in surface electromyography. *Ann. Biomed. Eng.*, **30**, 566-77.
- Booth, C. M., Cortina-Borja, M. J. and Theologis, T. N.** (2001). Collagen accumulation in muscles of children with cerebral palsy and correlation with severity of spasticity. *Dev. Med. Child Neurol.*, **43**, 314-320.
- Bottinelli, R., Pellegrino, M. A., Canepari, M., Rossi, R. and Reggiani, C.** (1999). Specific contributions of various muscle fibre types to human muscle performance: an in vitro study. *J. Electromyogr. Kinesiol.*, **9**, 87-95.

- Brown, I. E., Liinamaa, T. L. and Loeb, G. E.** (1996). Relationships between range of motion, Lo, and passive force in five strap-like muscles of the feline hind limb. *J. Morphol.*, **230**, 69-77.
- Buchthal, F. and Schmalbruch, H.** (1980). Motor unit of mammalian muscle. *Physiol. Rev.*, **60**, 90-142.
- Burke, R. E., Levine, D. N., Tsairis, P. and Zajac, F. E.** (1973). Physiological types and histochemical profiles in motor units of the cat gastrocnemius. *J. Physiol.*, **234**, 723-748.
- Citterio, G. and Agostoni, E.** (1984). Selective activation of quadriceps muscle fibers according to bicycling rate. *J. Appl. Physiol.* **57**, 371-379.
- Close, R.I.** (1964). Dynamic properties of fast and slow skeletal muscles of the rat during development. *J. Physiol.*, **173**, 74-95.
- Close, R.I.** (1965). Force: velocity properties of mouse muscles. *Nature*, **206**, 718-719.
- Cobb, M.** (2002). Exorcizing the animal spirits: Jan Swammerdam on nerve function. *Nat. Rev. Neurosci.*, **3**, 395-400.
- Crowninshield, R.D. and Brand, R.A.** (1981). A physiologically based criterion of muscle force prediction in locomotion. *J. Biomech.*, **14**, 793–801.
- Daley, M.A. and Biewener, A.A.** (2003). Muscle force-length dynamics during level versus incline locomotion: a comparison of in vivo performance of two guinea fowl ankle extensors. *J. Exp. Biol.*, **206**, 2941–58.
- Daniel, T. L., George, N. T., Williams, C. D., and Irving, T. C.** (2013). In Vivo Time Resolved X-Ray Diffraction Reveals Radial Motions of Myofilaments in Insect Flight Muscle. *Biophys. J.*, **104**, 485a-486a.
- De Luca, C. J.** (1997). The use of surface electromyography in biomechanics. *J. Appl. Biomech.*, **13**, 135-163.
- Delp, S.L., Loan, J.P., Hoy, M.G., Zajac, F.E., Topp, E.L. and Rosen, J.M.** (1990). An interactive graphics-based model of the lower extremity to study orthopaedic surgical procedures. *IEEE Trans. Biomed. Eng.*, **37**, 757-767.
- Delp, S.L. anderson, F.C., Arnold, A.S., Loan, P., Habib, A., John, C.T. and Thelen, D.G.** (2007). OpenSim: open-source software to create and analyze dynamic simulations of movement. *IEEE Trans. Biomed. Eng.*, **54**, 1940-1950.
- Dick, T.J.M., Arnold, A.S. and Wakeling, J.M.** (2016). Quantifying Achilles Tendon Force *In Vivo* from Ultrasound Images. *J. Biomech.*  
doi:10.1016/j.jbiomech.2016.07.036

- Dorn, T. W., Schache, A. G. and Pandy, M. G.** (2012). Muscular strategy shift in human running: Dependence of running speed on hip and ankle muscle performance. *J. Exp. Biol.*, **215**,1944-1956.
- Doud, J. R. and Walsh, J. M.** (1995). Muscle fatigue and muscle length interaction: effect on the EMG frequency components. *Electromyogr. Clin. Neurophysiol.*, **35**, 331-339.
- Ebashi, S. and Endo, M.** (1968). Calcium and muscle contraction. *Prog. Biophys. Mol. Biol.*, **18**, 123IN9167-166IN12183.
- Elliott, G. F., Lowy, J. and Worthington, C. R.** (1963). An X-ray and light-diffraction study of the filament lattice of striated muscle in the living state and in rigor. *J. Molec. Biol.*, **6**, 295IN8-305IN9.
- Epstein, M. and Herzog, W.** (1998). *Theoretical Models of Skeletal Muscles: Biological and Mathematical Considerations*. New York: John Wiley and Sons.
- Ericson, M.O., Nisell, R., Arborelius, U.P. and Ekholm, J.** (1984). Muscular activity during ergometer cycling. *Scand. J. Rehab. Med.*, **17**, 53-61.
- Ettema, G.J.C. and Huijing, P.A.** (1989). Properties of the tendinous structures and series elastic component of EDL muscle tendon complex of the rat. *J. Biomech.*, **22**, 1209–1215.
- Farina, D.** (2008). Counterpoint: spectral properties of the surface EMG do not provide information about motor unit recruitment and muscle fiber type. *J. Appl. Physiol.*, **105**, 1673-1674.
- Farris, D. J. and Sawicki, G. S.** (2012). Human medial gastrocnemius force–velocity behavior shifts with locomotion speed and gait. *PNAS*, **109**, 977-982.
- Farris, D. J., Robertson, B. D. and Sawicki, G. S.** (2013). Elastic ankle exoskeletons reduce soleus muscle force but not work in human hopping. *J. Appl. Physiol.*, **115**, 579-585.
- Faulkner, J. A., Claflin, D. R. and McCully, K. K.** (1986). Power output of fast and slow fibers from human skeletal muscles. *Human Muscle Power*, 81-94.
- Finni, T., Komi, P. V. and Lukkariniemi, J.** (1998). Achilles tendon loading during walking: application of a novel optic fiber technique. *Eur. J. Appl. Physiol. O.*, **77**, 289-291.
- Finni, T., Hodgson, J. A., Lai, A. M., Edgerton, V. R. and Sinha, S.** (2003). Nonuniform strain of human soleus aponeurosis-tendon complex during submaximal voluntary contractions in vivo. *J. Appl. Physiol.*, **95**, 829-837.

- Franz, J.R., Slane, L.C., Rasse, K. and Thelen, D.G.** (2015). Non-uniform in vivo deformations of the human Achilles tendon during walking. *Gait Posture*, **41**, 192-197.
- Fregly, B. J., Boninger, M. L. and Reinkensmeyer, D. J.** (2012). Personalized neuromusculoskeletal modeling to improve treatment of mobility impairments: a perspective from European research sites. *J. Neuroeng. Rehabil.*, **9**, 1.
- Fukashiro, S., Rob, M., Ichinose, Y., Kawakami, Y. and Fukunaga, T.** (1995). Ultrasonography gives directly but noninvasively elastic characteristic of human tendon in vivo. *Eur. J. Appl. Physiol. Occup. Physiol.*, **71**, 555-557.
- Fukunaga, T., Ichinose, Y., Ito, M., Kawakami, Y. and Fukashiro, S.** (1997). Determination of fascicle length and pennation in a contracting human muscle in vivo. *J. Appl. Physiol.* **82**, 354-358.
- Fukunaga, T., Kubo, K., Kawakami, Y., Fukashiro, S., Kanehisa, H. and Maganaris, C. N.** (2001). In vivo behaviour of human muscle tendon during walking. *Proc. R. Soc. B*, **268**, 229-233.
- Gans, C. and Bock, W. J.** (1965). The functional significance of muscle architecture – a theoretical analysis. *Ergeb. Anat. Entwicklungsgesch.*, **38**, 115-142.
- Gareis, H., Moshe, S., Baratta, R., Best, R. and D'Ambrosia, R.** (1992). The isometric length-force models of nine different skeletal muscles. *J. Biomech.*, **25**, 903-916.
- Gerus, P., Rao, G. and Berton, E.** (2012). Subject-Specific Tendon-Aponeurosis Definition in Hill-Type Model Predicts Higher Muscle Forces in Dynamic Tasks. *PLoS One*, **7**, e44406.
- Gerus, P., Rao, G. and Berton, E.** (2013). Ultrasound-based subject-specific parameters 14 improve fascicle behaviour estimation in Hill-type muscle model. *Comput. Methods Biomed. Engin.*, **18**, 116-123.
- Gillespie, C.A., Simpson, D.R. and Edgerton, V.R.** (1974). Motor unit recruitment as reflected by muscle fibre glycogen loss in a prosimian (bushbaby) after running and jumping. *J. Neurol. Neurosurg. Psychiatry*, **37**, 817–824.
- Gollapudi, S. K. and Lin, D. C.** (2009). Experimental determination of sarcomere force–length relationship in type-I human skeletal muscle fibers. *J. Biomech.*, **42**, 2011-2016.
- Gordon, A. M., Huxley, A. F. and Julian, F. J.** (1966). The variation in isometric tension with sarcomere length in vertebrate muscle fibres. *J. Physiol.*, **184**, 170.

- Gregor, R.J., Cavanagh, P.R. and LaFortune, M.** (1985). Knee flexor moments during propulsion in cycling—A creative solution to Lombard's Paradox. *J. Biomech.*, **18**, 307-316.
- Gregor, R. J., Komi, P. V. and Järvinen, M.** (1987). Achilles tendon forces during cycling. *Int. J. Sports Med.*, **8**, 9-14.
- Gregor, R.J., Komi, P.V., Browning, R.C. and Järvinen, M.** (1991). A comparison of the triceps surae and residual muscle moments at the ankle during cycling. *J. Biomech.*, **24**, 287-297.
- Hafer-Macko, C. E., Ryan, A. S., Ivey, F. M. and Macko, R. F.** (2008). Skeletal muscle changes after hemiparetic stroke and potential beneficial effects of exercise intervention strategies. *J. Rehabil. Res. Dev.*, **45**, 261.
- Hamner, S. R., Seth, A. and Delp, S. L.** (2010). Muscle contributions to propulsion and support during running. *J. Biomech.*, **43**, 2709-2716.
- Hamner, S. R. and Delp, S. L.** (2013). Muscle contributions to fore-aft and vertical body mass center accelerations over a range of running speeds. *J. Biomech.*, **46**, 780-787.
- Handsfield, G. G., Meyer, C. H., Hart, J. M., Abel, M. F. and Blemker, S. S.** (2014). Relationships of 35 lower limb muscles to height and body mass quantified using MRI. *J. Biomech.*, **47**, 631-638.
- Hashizume, S., Iwanuma, S., Akagi, R., Kanehisa, H., Kawakami, Y. and Yanai, T.** (2012). In vivo determination of the Achilles tendon moment arm in three-dimensions. *J. Biomech.*, **45**, 409-413.
- He, Z. H., Bottinelli, R., Pellegrino, M. A., Ferenczi, M. A. and Reggiani, C.** (2000). ATP consumption and efficiency of human single muscle fibers with different myosin isoform composition. *Biophys. J.*, **79**, 945-961.
- Henneman E.** (1957). Relation between size of neurons and their susceptibility to discharge. *Science*, **126**, 1345–1347.
- Henneman, E., Somjen, G. and Carpenter, D. O.** (1965a). Excitability and inhibitability of motoneurons of different sizes. *J. Neurophysiol.*, **28**, 599-620.
- Henneman, E., Somjen, G. and Carpenter, D. O.** (1965b). Functional significance of cell size in spinal motoneurons. *J. Neurophysiol.*, **28**, 560-580.
- Herbert, R. D. and Gandevia, S. C.** (1995). Changes in pennation with joint angle and muscle torque: in vivo measurements in human brachialis muscle. *J. Physiol.*, **484**, 523-532.

- Hernandez, A., Lenz, A.L. and Thelen, D.G.** (2010). Electrical stimulation of the rectus femoris during pre-swing diminishes hip and knee flexion during the swing phase of normal gait. *IEEE Trans, Neural Syst. Rehabil, Eng.*, **18**, 523-30.
- Hicks, J.L., Uchida, T.K., Seth, A., Rajagopal, A. and Delp, S.L.** (2015). Is my model good enough? Best practices for verification and validation of musculoskeletal models and simulations of movement. *J. Biomech. Eng.*, **137**, 020905.
- Hill, A. V.** (1938). The heat of shortening and the dynamic constants of muscle. *Proc. R. Soc. B*, **126**, 136–195.
- Hodson-Tole, E.F. and Wakeling, J.M.** (2007). Variations in motor unit recruitment patterns occur within and between muscles in the running rat (*Rattus norvegicus*). *J. Exp. Biol.*, **210**, 2333–2345.
- Hodson-Tole, E. F., Wakeling, J. M., and Dick, T. J.** (2016). Passive Muscle-Tendon Unit Gearing Is Joint Dependent in Human Medial Gastrocnemius. *Front. Physiol.*, **7**.
- Hof, A.L.** (1984). EMG and Muscle Force - an introduction. *Hum. Mov. Sci.*, **3**, 119–153.
- Holt, N. C. and Azizi, E.** (2014). What drives activation-dependent shifts in the force–length curve?. *Biol. Lett.*, **10**, 20140651.
- Holt, N. C., Wakeling, J. M. and Biewener, A. A.** (2014). The effect of fast and slow motor unit activation on whole-muscle mechanical performance: the size principle may not pose a mechanical paradox. *Proc. R. Soc. B.*, **281**, 20140002.
- Holt, N. C. and Azizi, E.** (2016). The effect of activation level on muscle function during locomotion: are optimal lengths and velocities always used?. *Proc. R. Soc. B.*, **283**, 20152832.
- Huijing, P. A. and Woittiez, R. D.** (1983). The effect of architecture on skeletal muscle performance: a simple planimetric model. *Neth. J. Zool.*, **34**, 21-32.
- Huijing, P.A. and Ettema, G.J.C.** (1988). Length – force characteristics of aponeurosis in passive muscle and during isometric and slow dynamic contractions of rat gastrocnemius muscle. *Acta Morphol Neerlando-Scand.*, **26**, 51–62.
- Huijing, P. A., Bénard, M. R., Harlaar, J., Jaspers, R. T. and Becher, J. G.** (2013). Movement within foot and ankle joint in children with spastic cerebral palsy: a 3-dimensional ultrasound analysis of medial gastrocnemius length with correction for effects of foot deformation. *BMC Musculoskelet. Disord.*, **14**, 365.
- Hull, M.L. and Jorge, M.** (1985). A method for biomechanical analysis of bicycle pedalling. *J. Biomech.*, **18**, 631-644.

- Hutchinson, J. R. and Garcia, M.** (2002). Tyrannosaurus was not a fast runner. *Nature*, **415**, 1018-1021.
- Hutchinson, J. R., Rankin, J. W., Rubenson, J., Rosenbluth, K. H., Siston, R. A. and Delp, S. L.** (2015). Musculoskeletal modeling of an ostrich (*Struthio camelus*) pelvic limb: influence of limb orientation on muscular capacity during locomotion *PeerJ*, **3**, 31001.
- Huxley, H. E.** (1969). The mechanism of muscular contraction. *Science*, **164**, 1356-1365.
- Huxley, A. F.** (1974). Muscular contraction. *J. Physiol.*, **243**, 1.
- Johnson, M.A., Polgar, J., Weightman, D. and Appleton, D.** (1973). Data on the distribution of fibre types in thirty-six human muscles. An autopsy study. *J. Neurolog. Sci.*, **18**, 111– 129.
- Josephson, R. K. and Edman, K. A. P.** (1988). The consequences of fibre heterogeneity on the force-velocity relation of skeletal muscle. *Acta Physiol. Scand.*, **132**, 341-352.
- Joumaa, V., Rassier, D. E., Leonard, T. R. and Herzog, W.** (2008). The origin of passive force enhancement in skeletal muscle. *Am. J. Physiol. Cell*, **294**, C74-C78.
- Kautz, S.A. and Neptune, R.R.** (2002). Biomechanical determinants of pedalling energetics: internal and external work are not independent. *Exer. Sport Sci. Rev.* **3**, 159-65.
- Kawakami, Y., Abe, T. and Fukunaga, T.** (1993). Muscle-fiber pennation angles are greater in hypertrophied than in normal muscles. *J. Appl. Physiol.*, **74**, 2740–2744.
- Kawakami, Y., Ichinose, Y. and Fukunaga, T.** (1998). Architectural and functional features of human triceps surae muscles during contraction. *J. Appl. Physiol.*, **85**, 398-404.
- Ker, R. F.** (1981). Dynamic tensile properties of the plantaris tendon of sheep (*Ovis aries*). *J. Exp. Biol.*, **93**, 283-302.
- Ker, R. F., Bennett, M. B., Bibby, S. R., Kester, R. C. and Alexander, R. M.** (1987). The spring in the arch of the human foot. *Nature*, **325**, 147 -149
- Kernell, D., Eerbeek, O. and Verhey, B. A.** (1983). Relation between isometric force and stimulus rate in cat's hindlimb motor units of different twitch contraction time. *Exp. Brain Res.*, **50**, 220-227.

- Kim, H., Sandercock, T. G. and Heckman, C. J.** (2015). An action potential-driven model of soleus muscle activation dynamics for locomotor-like movements. *J. Neural. Eng.*, **12**, 046025.
- Komi, P. V.** (1990). Relevance of in vivo force measurements to human biomechanics. *J. Biomech.*, **23**, 23-34.
- Komi, P. V., Belli, A., Huttunen, V., Bonnefoy, R., Geysant, A. and Lacour, J. R.** (1996). Optic fibre as a transducer of tendomuscular forces. *Eur. J. Appl. Physiol. Occup. Physiol.*, **72**, 278-280.
- Kongsgaard, M., Nielsen, C. H., Hegnsvad, S., Aagaard, P. and Magnusson, S. P.** (2011). Mechanical properties of the human Achilles tendon, in vivo. *Clin. Biomech.*, **26**, 772-777.
- Kubo, K., Kanehisa, H. and Fukunaga, T.** (2003). Gender differences in the viscoelastic properties of tendon structures. *Eur. J. Appl. Physiol.*, **88**, 520-526.
- Kupa, E.J, Roy, S.H, Kandarian, S.C. and de Luca, C.J.** (1995). Effects of muscle fibre type and size on EMG median frequency and conduction velocity. *J. Appl. Physiol.*, **79**, 23–32.
- Kurokawa, S., Fukunaga, T. and Fukashiro, S.** (2001). Behaviour of fascicles and tendinous structures of human gastrocnemius during vertical jumping. *J. Appl. Physiol.*, **90**, 1349-1358.
- Kushermick, M.J. and Davies R.E.** (1969).The chemical energetics of muscle contraction. II. The chemistry, efficiency and power of maximally working sartorius muscles. *Proc. R. Soc. B.*, **174**, 315–353.
- Lai, A., Schache, A. G., Lin, Y. C. and Pandy, M. G.** (2014). Tendon elastic strain energy in the human ankle plantar-flexors and its role with increased running speed. *J. Exp. Biol.*, **217**, 3159-3168.
- Lai, A., Lichtwark, G. A., Schache, A. G., Lin, Y. C., Brown, N. A. and Pandy, M. G.** (2015). In vivo behavior of the human soleus muscle with increasing walking and running speeds. *J. Appl. Physiol.*, **118**, 1266-1275.
- Laracca, E., Stewart, C., Postans, N., and Roberts, A.** (2014). The effects of surgical lengthening of hamstring muscles in children with cerebral palsy–The consequences of pre-operative muscle length measurement. *Gait Posture*, **39**, 847-851.
- Lee, S.S. and Piazza, S.J.** (2009). Built for speed: musculoskeletal structure and sprinting ability. *J. Exp. Biol.*, **212**, 3700-3707.

- Lee, S. S., Arnold, A. S., de Boef Miara, M., Biewener, A. A. and Wakeling, J. M.** (2011). EMG analysis tuned for determining the timing and level of activation in different motor units. *J. Electromyogr. Kinesiol.*, **21**, 557–565.
- Lee, S. S., Arnold, A. S., de Boef Miara, M., Biewener, A. A. and Wakeling, J. M.** (2013). Accuracy of gastrocnemius muscles forces in walking and running goats predicted by one-element and two-element Hill-type models. *J. Biomech.*, **46**, 2288-2295.
- Levin, O., Mizrahi, J. and Isakov, E.** (1999). Transcutaneous FES of paralyzed quadriceps: is knee torque affected by unintended activation of the hamstrings. *J. Electromyogr. Kinesiol.*, **10**, 47–58
- Li, L., Tong, K. Y., Hu, X. L., Hung, L. K. and Koo, T. K. K.** (2009). Incorporating ultrasound-measured musculotendon parameters to subject-specific EMG-driven model to simulate voluntary elbow flexion for persons after stroke. *Clin. Biomech.*, **24**, 101-109.
- Lichtwark, G. A. and Wilson, A. M.** (2005a). In vivo mechanical properties of the human Achilles tendon during one-legged hopping. *J. Exp. Biol.*, **208**, 4715-4725.
- Lichtwark, G. A. and Wilson, A. M.** (2005b). A modified Hill muscle model that predicts muscle power output and efficiency during sinusoidal length changes. *J. Exp. Biol.*, **208**, 2831-2843.
- Lichtwark, G. A. and Wilson, A. M.** (2006). Interactions between the human gastrocnemius muscle and the Achilles tendon during incline, level and decline locomotion. *J. Exp. Biol.*, **209**, 4379-4388.
- Lichtwark, G. A., Bougoulias, K. and Wilson, A. M.** (2007). Muscle fascicle and series elastic element length changes along the length of the human gastrocnemius during walking and running. *J. Biomech.*, **40**, 157-164.
- Lieber, R.L., Leonard, M.E., Brown, C.G. and Trestik, C.L.** (1991). Frog semitendinosus tendon load-strain and stress-strain properties during passive loading. *Am. J. Physiol. Cell. Physiol.*, **261**, C86–C92.
- Lieber, R. L. and Ward, S. R.** (2011). Skeletal muscle design to meet functional demands. *Phil. Trans. R. Soc. B*, **366**, 1466-1476.
- Lindström, L. H. and Magnusson, R. I.** (1977). Interpretation of myoelectric power spectra: a model and its applications. *Proc. IEEE*, **65**, 653-662.
- Luff, A.R.** (1975). Dynamic properties of fast and slow skeletal muscles in the cat and rat following cross-reinnervation. *J. Physiol.*, **248**, 83-96.

- Maganaris, C.N., Baltzopoulos, V. and Sargeant, A.J.** (1998a). In vivo measurements of the triceps surae complex architecture in man: implications for muscle function. *J. Physiol.*, **512**, 603–614.
- Maganaris, C.N., Baltzopoulos, V. and Sargeant, A.J.** (1998b). Changes in Achilles tendon moment arm from rest to maximum isometric plantarflexion: in vivo observations in man. *J. Physiol.-London*, **510**, 977-85.
- Maganaris, C. N., Kawakami, Y. and Fukunaga, T.** (2001). Changes in aponeurotic dimensions upon muscle shortening: in vivo observations in man. *J. Anat.*, **199**, 449-456.
- Maganaris, C. N. and Paul, J. P.** (2002). Tensile properties of the in vivo human gastrocnemius tendon. *J. Biomech.*, **35**, 1639-1646.
- Maganaris, C.N.** (2003). Force-length characteristics of the in vivo human gastrocnemius muscle. *Clin. Anat.*, **16**, 215-223.
- Magnusson, S.P., Aagaard, P., Rosager, S., Dyhre-Poulsen, P. and Kjaer, M.** (2001). Load-displacement properties of the human triceps surae aponeurosis in vivo. *J. Physiol.*, **531**, 277–288.
- Malaiya, R., McNee, A. E., Fry, N. R., Eve, L. C., Gough, M. and Shortland, A. P.** (2007). The morphology of the medial gastrocnemius in typically developing children and children with spastic hemiplegic cerebral palsy. *J. Electromyogr. Kinesiol.*, **17**, 657-663.
- Matson, A., Konow, N., Miller, S., Konow, P. P. and Roberts, T. J.** (2012). Tendon material properties vary and are interdependent among turkey hindlimb muscles. *J. Exp. Biol.*, **215**, 3552-3558.
- McGeer, T.** (1990). Passive dynamic walking. *Int. J. Robot. Res.*, **9**, 62-82.
- McMahon, T. A.** (1984). *Muscles, reflexes, and locomotion*. New Jersey: Princeton University Press.
- Millard, M., Uchida, T., Seth, A. and Delp, S. L.** (2013). Flexing computational muscle: modeling and simulation of musculotendon dynamics. *J. Biomed. Eng.*, **135**, 021005.
- Milner-Brown, H. S., Stein, R. B. and Yemm, R.** (1973). The orderly recruitment of human motor units during voluntary isometric contractions. *J. Physiol.*, **230**, 359.
- Milner-Brown, H. S. and Stein, R. B.** (1975). The relation between the surface electromyogram and muscular force. *J. Physiol.*, **246**, 549.

- Monti, R.J., Roy, R.R., Zhong, H. and Edgerton, V.R.** (2003). Mechanical properties of rat soleus aponeurosis and tendon during variable recruitment in situ. *J. Exp. Biol.*, **206**, 3437–3445.
- Morris, C. A., Tobacman, L. S. and Homsher, E.** (2001). Modulation of contractile activation in skeletal muscle by a calcium-insensitive troponin C mutant. *J. Biol. Chem.*, **276**, 20245-20251.
- Morrison, S. M., Dick, T. J. and Wakeling, J. M.** (2015). Structural and mechanical properties of the human Achilles tendon: Sex and strength effects. *J. Biomech.*, **48**, 3530-3.
- Muramatsu, T., Muraoka, T., Takeshita, D., Kawakami, Y., Hirano, Y. and Fukunaga, T.** (2001). Mechanical properties of tendon and aponeurosis of human gastrocnemius muscle in vivo. *J. Appl. Physiol.*, **90**, 1671-1678.
- Muramatsu, T., Muraoka, T., Kawakami, Y. and Fukunaga, T.** (2002a). Superficial aponeurosis of human gastrocnemius is elongated during contraction: implications for modeling muscle-tendon unit. *J. Biomech.*, **35**, 217–223.
- Muramatsu, T., Muraoka, T., Kawakami, Y., Shibayama, A. and Fukunaga, T.** (2002b). In vivo determination of fascicle curvature in contracting human skeletal muscles. *J. Appl. Physiol.*, **92**, 129-134.
- Muraoka, T., Muramatsu, T., Fukunaga, T. and Kanehisa, H.** (2005). Elastic properties of human Achilles tendon are correlated to muscle strength. *J. Appl. Physiol.*, **99**, 665-669.
- Namburete, A. I., Rana, M. and Wakeling, J. M.** (2011). Computational methods for quantifying in vivo muscle fascicle curvature from ultrasound images. *J. Biomech.*, **44**, 2538-2543.
- Narici, M. V., Binzoni, T., Hiltbrand, E., Fasel, J., Terrier, F. and Cerretelli, P.** (1996). In vivo human gastrocnemius architecture with changing joint angle at rest and during graded isometric contraction. *J. Physiol.*, **496**, 287.
- Neptune, R. R., Kautz, S. A. and Zajac, F. E.** (2001). Contributions of the individual ankle plantarflexors to support, forward progression and swing initiation during walking. *J. Biomech.*, **34**, 1387-1398.
- Olson, C. B., Carpenter, D. O. and Henneman, E.** (1968). Orderly recruitment of muscle action potentials: motor unit threshold and EMG amplitude. *Arch. Neurol.*, **19**, 591.
- O'Neill, M. C., Lee, L. F., Larson, S. G., Demes, B., Stern, J. T. and Umberger, B. R.** (2013). A three-dimensional musculoskeletal model of the chimpanzee (*Pan troglodytes*) pelvis and hind limb. *J. Exp. Biol.*, **216**, 3709-3723.

- Otten, E.** (1987). A myocybernetic model of the jaw system of the rat. *J. Neurosci. Methods*, **21**, 287-302.
- Passmore, E., Lai, A., Sangeux, M., Schache, A. G., and Pandy, M. G.** Application of ultrasound imaging to subject-specific modelling of the human musculoskeletal system. *Meccanica*, 1-12.
- Perreault, E.J., Heckman, C.J. and Sandercock, T.G.** (2003). Hill muscle model errors during movement are greatest within the physiologically relevant range of motor unit firing rates. *J. Biomech.*, **36**, 211–218.
- Peterson, C. L., Hall, A. L., Kautz, S. A., and Neptune, R. R.** (2010). Pre-swing deficits in forward propulsion, swing initiation and power generation by individual muscles during hemiparetic walking. *J. Biomech.*, **43**, 2348-2355.
- Prado, L. G., Makarenko, I., Andresen, C., Krüger, M., Opitz, C. A. and Linke, W. A.** (2005). Isoform diversity of giant proteins in relation to passive and active contractile properties of rabbit skeletal muscles. *J. Gen. Physiol.*, **126**, 461-480.
- Prager, R.W., Rohling, R.N., Gee, A.H. and Berman, L.** (1998). Rapid calibration for 3-D freehand ultrasound. *Ultrasound Med. Biol.*, **24**, 855-869.
- Proske, U. and Morgan, D. L.** (2001). Muscle damage from eccentric exercise: mechanism, mechanical signs, adaptation and clinical applications. *J. Physiol.*, **537**, 333-345.
- Purslow, P. P.** (2002). The structure and functional significance of variations in the connective tissue within muscle. *Physiol. A Mol. Integr. Physiol.*, **133**, 947-966.
- Rack, P. M. H. and Westbury, D. R.** (1969). The effects of length and stimulus rate on tension in the isometric cat soleus muscle. *J. Physiol.*, **204**, 443–460.
- Rahemi, H.** (2015). *Structural mechanics of skeletal muscle contractions: mechanistic findings using a finite element model*, PhD thesis, Simon Fraser University.
- Rahemi, H., Nigam, N., and Wakeling, J. M.** (2014). Regionalizing muscle activity causes changes to the magnitude and direction of the force from whole muscles—a modeling study. *Front. Physiol.*, **5**.
- Rahemi, H., Nigam, N., and Wakeling, J. M.** (2015). The effect of intramuscular fat on skeletal muscle mechanics: implications for the elderly and obese. *Interface*, **12**, 20150365.
- Rana, M. and Wakeling, J. M.** (2011). In-vivo determination of 3D muscle architecture of human muscle using free hand ultrasound. *J. Biomech.*, **44**, 2129-2135.

- Rana, M., Hamarneh, G. and Wakeling, J. M.** (2013). 3D fascicle orientations in triceps surae. *J. Appl. Physiol.*, **115**, 116-125.
- Randhawa, A., Jackman, M. E. and Wakeling, J. M.** (2013). Muscle gearing during isotonic and isokinetic movements in the ankle plantarflexors. *Eur. J. Appl. Physiol.*, **113**, 437-447.
- Randhawa, A. and Wakeling, J. M.** (2015). Multidimensional models for predicting muscle structure and fascicle pennation. *J. Theoret. Biol.*, **382**, 57-63.
- Rassier, D.E., MacIntosh, B.R. and Herzog, W.** (1999). Length dependence of active force production in skeletal muscle. *J. Appl. Physiol.*, **86**, 1445–1457
- Reaz, M. B. I., Hussain, M. S. and Mohd-Yasin, F.** (2006). Techniques of EMG signal analysis: detection, processing, classification and applications. *Biol. Proced. Online*, **8**, 11-35.
- Roberts, T. J., Marsh, R. L., Weyand, P. G. and Taylor, C. R.** (1997). Muscular force in running turkeys: the economy of minimizing work. *Science*, **275**, 1113-1115.
- Roberts, T. J.** (2002). The integrated function of muscles and tendons during locomotion. *Comp. Biochem. Physiol. A Mol. Integr. Physiol.*, **133**, 1087-1099.
- Robinson, D. A.** (1977). Vestibular and optokinetic symbiosis: an example of explaining by modelling. Control of gaze by brain stem neurons. *Dev. Neurosci.*, 49-58.
- Roeleveld, K., Blok, J.H., Stegeman, D.F. and van Oosterom, A.** (1997). Volume conduction models for surface EMG; confrontation with measurements. *J. Electromyogr. Kinesiol.*, **7**, 221-232.
- Rome, L.C., Funke, R.P., Alexander, R., Lutz G., Aldridge H., Scott, F. and Freadman, M.** (1988). Why animals have different muscle fibre types. *Nature*, **335**, 824–827.
- Rouffet, D.M. and Hautier, C.A.** (2008). EMG normalization to study muscle activation in cycling. *J. Electromyogr. Kinesiol.*, **18**, 866-878.
- Roy, R. R., Meadows, I. D., Baldwin, K. M. and Edgerton, V. R.** (1982). Functional significance of compensatory overloaded rat fast muscle. *J. Appl. Physiol.*, **52**, 473-478.
- Rugg, S.G., Gregor, R.J., Mandelbaum, B.R. and Chiu, L.** (1990). In vivo moment arm calculations at the ankle using magnetic resonance imaging (MRI). *J. Biomech.*, **23**, 495499-497501.

- Sandercock, T.G. and Heckman, C.J.** (1997). Force from cat soleus muscle during imposed locomotor-like movements: experimental data versus Hill-type model predictions. *J. Neurophysiol.*, **77**, 1538–1552.
- Sandow, A.** (1952). Excitation-contraction coupling in muscular response. *Yale J. Biol. Med.*, **25**, 176.
- Schiaffino, S. and Reggiani, C.** (1996). Molecular diversity of myofibrillar proteins: gene regulation and functional significance. *Physiol. Rev.*, **76**, 371–423.
- Schiaffino, S. and Reggiani, C.** (2011). Fiber types in mammalian skeletal muscles. *Physiol. Rev.*, **91**, 1447-1531.
- Scott, S. H. and Loeb, G. E.** (1995). Mechanical properties of aponeurosis and tendon of the cat soleus muscle during whole-muscle isometric contractions. *J. Morphol.*, **224**, 73-86.
- Semciw, A. I., Neate, R. and Pizzari, T.** (2014). A comparison of surface and fine wire EMG recordings of gluteus medius during selected maximum isometric voluntary contractions of the hip. *J. Electromyogr. Kinesiol.*, **24**, 835-840.
- Shadwick, R. E., Katz, S. L., Korsmeyer, K. E., Knower T. and Covell, J. W.** (1999). Muscle dynamics in skipjack tuna: timing of red muscle shortening in relation to activation and body curvature during steady swimming. *J. Exp. Biol.*, **202**, 2139-2150.
- Sheehan, F.T.** (2012). The 3D *in vivo* Achilles' tendon moment arm, quantified during active muscle control and compared across sexes. *J. Biomech.*, **45**, 225-230.
- Shue, G., Crago, E. and Chizeck, H.J.** (1995). Muscle-joint models incorporating activation dynamics, moment-angle, and moment-velocity properties. *IEEE Trans. Biomed. Eng.*, **42**, 212–223.
- Siston, R.A. and Delp, S.L.** (2006). Evaluation of a new algorithm to determine the hip joint center. *J. Biomech.*, **39**, 125-130.
- Smak, W., Neptune, R.R. and Hull, M.L.** (1999). The influence of pedaling rate on bilateral asymmetry in cycling. *J. Biomech.*, **32**, 899-906.
- Smith, J. L., Edgerton, V. R., Betts, B. and Collatos, T. C.** (1977). EMG of slow and fast ankle extensors of cat during posture, locomotion, and jumping. *J. Neurophysiol.*, **40**, 503-513.
- Smith, J. L., Betts, B., Edgerton, V. R. and Zernicke, R. F.** (1980). Rapid ankle extension during paw shakes: selective recruitment of fast ankle extensors. *J. Neurophysiol.*, **43**, 612-620.

- Smith, L. R., Gerace-Fowler, L. and Lieber, R. L.** (2011). Muscle extracellular matrix applies a transverse stress on fibers with axial strain. *J. Biomech.*, **44**, 1618-1620.
- Spägle, T., Kistner, A. and Gollhofer, A.** (1999). Modelling, simulation and optimisation of a human vertical jump. *J. Biomech.*, **32**, 521-530.
- Spector, S. A., Gardiner, P. F., Zernicke, R. F., Roy, R. R. and Edgerton, V. R.** (1980) Muscle architecture and force-velocity characteristics of cat soleus and medial gastrocnemius: implications for motor control. *J. Neurophysiol.*, **44**, 951-960.
- Steele, K. M., Seth, A., Hicks, J. L., Schwartz, M. S. and Delp, S. L.** (2010). Muscle contributions to support and progression during single-limb stance in crouch gait. *J. Biomech.*, **43**, 2099-2105.
- Steele, K. M., Rozumalski, A. and Schwartz, M. H.** (2015). Muscle synergies and complexity of neuromuscular control during gait in cerebral palsy. *Dev. Med. Child Neurol.*, **57**, 1176-1182.
- Stotz, P. J. and Bawa, P.** (2001). Motor unit recruitment during lengthening contractions of human wrist flexors. *Muscle Nerve*, **24**, 1535-1541.
- Swoap, S.J, Caiozzo V.J. and Baldwin K.M.** (1997). Optimal shortening velocities for *in situ* power production of rat soleus and plantaris muscles. *Am. J. Physiol.*, **273**, 1057–1063.
- Umberger, B. R., Gerritsen, K. G. and Martin, P. E.** (2003). A model of human muscle energy expenditure. *Comput. Methods Biomech. Biomed. Engin.*, **6**, 99-111.
- van den Bogert, A. J., Blana, D. and Heinrich, D.** (2011). Implicit methods for efficient musculoskeletal simulation and optimal control. *Procedia IUTAM*, **2**, 297-316.
- Van der Krogt, M., Seth, A., Steele, K., Bar-On, L., Desloovere, K., Harlaar, J. and Delp, S.** (2013). A model of muscle spasticity in Opensim. *Gait Posture*, **38**, S16.
- Van Donkelaar, C.C., Willems, P.J.B., Muijtjens, A.M.M. and Drost, M.R.** (1999). Skeletal muscle transverse strain during isometric contraction at different lengths. *J. Biomech.*, **32**, 755-762.
- Van Leeuwen, J. L.** (1992). Muscle function in locomotion. In: Alexander, R. McN. (Ed.), *Mechanics of animal locomotion*, pp. 191-249. London: Springer.
- Van Leeuwen, J. L. and Spoor, C. W.** (1992). Modelling mechanically stable muscle architectures. *Proc. R. Soc. B*, **336**, 275-292.

- Vandervoort, A.A. and McComas, A.J.** (1983). A comparison of the contractile properties of the human gastrocnemius and soleus muscles. *Eur. J. Appl. Physiol.*, **51**, 435–440.
- Vogel, S.** (2003). *Prime mover: a natural history of muscle*. New York: W.W. Norton and Company.
- von Tscherner V.** (2000). Intensity analysis in time-frequency space of surface myoelectric signals by wavelets of specified resolution. *J. Electromyogr. Kinesiol.*, **10**, 433–445.
- von Tscherner, V. and Barandun, M.** (2010). Wavelet based correlation and coherence analysis reveals frequency dependent motor unit conduction velocity of the abductor pollicis brevis muscle. *J. Electromyogr. Kinesiol.*, **20**, 1088-1096.
- von Tscherner, V. and Nigg, B. M.** (2008). Point: Counterpoint: Spectral properties of the surface EMG can characterize/do not provide information about motor unit recruitment strategies and muscle fiber type. *J. Appl. Physiol.*, **105**, 1671-1673.
- Wakeling, J.M. and Rozitis, A.I.** (2004). Spectral properties of myoelectric signals from different motor units in the leg extensor muscles. *J. Exp. Biol.*, **207**, 2519-2528.
- Wakeling, J. M., Uehli, K. and Rozitis, A. I.** (2006). Muscle fibre recruitment can respond to the mechanics of the muscle contraction. *J. R. Soc. Interface*, **3**, 533-544.
- Wakeling, J., Delaney, R. and Dudkiewicz, I.** (2007). A method for quantifying dynamic muscle dysfunction in children and young adults with cerebral palsy. *Gait Posture*, **25**, 580-589.
- Wakeling, J.M.** (2009). Patterns of motor recruitment can be determined using surface EMG. *J. Electromyogr. Kinesiol.*, **19**, 199–207
- Wakeling, J.M. and Horn, T.** (2009). Neuromechanics of muscle synergies during cycling. *J. Neurophysiol.*, **101**, 843-854.
- Wakeling, J.M., Blake, O.M. and Chan, H.K.** (2010). Muscle coordination is key to the power output and mechanical efficiency of limb movements. *J. Exp. Biol.*, **213**, 487-492.
- Wakeling, J. M., and Lee, S. S.** (2011). Modelling muscle forces: from scaled fibres to physiological task-groups. *Procedia IUTAM*, **2**, 317-326.
- Wakeling, J.M., Blake, O.M., Wong, I., Rana, M. and Lee, S.S.** (2011). Movement mechanics as a determinate of muscle structure, recruitment and coordination. *Proc. R. Soc. B*, **366**, 1554-1564.

- Wakeling, J.M., Lee, S.S., de Boef Miara, M., Arnold, A.S. and Biewener, A.A.** (2012). A muscle's force depends on the recruitment patterns of its fibers. *Ann. Biomed. Eng.*, **40**, 1708–1720.
- Wakeling, J. M., Jackman, M., & Namburete, A. I.** (2013). The Effect of External Compression on the Mechanics of Muscle Contraction. *J. App. Biomech.*, **29**, 360-364.
- Wakeling, J. M. and Randhawa, A.** (2014). Transverse strains in muscle fascicles during voluntary contraction: a 2D frequency decomposition of B-mode ultrasound images. *J. Biomed. Imag.*, **4**.
- Ward, S.R., Eng, C.M., Smallwood, L.H. and Lieber, R.L.** (2009). Are current measurements of lower extremity muscle architecture accurate?. *Clin. Orthop. Relat. Res.*, **467**, 1074-1082.
- Williams, P. E. and Goldspink, G.** (1984). Connective tissue changes in immobilised muscle. *J. Anat.*, **138**, 343.
- Williams, C. D., Salcedo, M. K., Irving, T. C., Regnier, M., and Daniel, T. L.** (2013). The length–tension curve in muscle depends on lattice spacing. *Proc. R. Soc. B*, **280**, 20130697.
- Winter, D.A., Patla, A.E., Ishac, M. and Gage, W.H.** (2003). Motor mechanisms of balance during quiet standing. *J. Electromyogr. Kinesiol.*, **13**, 49-56.
- Winter, D.A.** (2009). *Biomechanics and motor control of human movement*. New York: John Wiley and Sons.
- Winters, J. M.** (1990). Hill-based muscle models: a systems engineering perspective. In *Multiple muscle systems*. pp. 69-93. New York: Springer.
- Winters, T. M., Takahashi, M., Lieber, R. L., and Ward, S. R.** (2011). Whole Muscle Length-Tension Relationships Are Accurately Modeled as Scaled Sarcomeres in Rabbit Hindlimb Muscles. *J. Biomech.*, **44**, 109–115.
- Wolf, S.L., Ammerman, J. and Jann, B.** (1998). Organization of responses in human lateral gastrocnemius muscle to specified body perturbations. *J. Electromyogr. Kinesiol.*, **8**, 11-21.
- Xiao, M., and Higginson, J.** (2010). Sensitivity of estimated muscle force in forward simulation of normal walking. *J. Appl. Biomech.*, **26**, 142.
- Yeargin-Allsopp, M., Van Naarden Braun, K., Doernberg, N.S., Benedict, R.E., Kirby, R.S. and Durkin, M.S.** (2008). Prevalence of cerebral palsy in 8-year-old children in three areas of the United States in 2002: a multisite collaboration. *Pediatrics*, **121**, 547–54.

- Zajac, F. E.** (1989). Muscle and tendon: properties, models, scaling, and application to biomechanics and motor control. *Crit. Rev. Biomed. Eng.*, **17**, 359-411.
- Zajac, F.E.** (1993). Muscle coordination of movement: a perspective. *J. Biomech.* 1993, **26**, 109–124.
- Zajac, F. E., Neptune, R. R. and Kautz, S. A.** (2002). Biomechanics and muscle coordination of human walking: Part I: Introduction to concepts, power transfer, dynamics and simulations. *Gait Posture*, **16**, 215-232.
- Zatsiorsky, V. and Prilutsky, B.** (2012). *Biomechanics of skeletal muscles*. Champaign: Human Kinetics.
- Zhao, H., Ren, Y., Wu, Y. N., Liu, S. Q. and Zhang, L. Q.** (2009). Ultrasonic evaluations of Achilles tendon mechanical properties poststroke. *J. Appl. Physiol.*, **106**, 843-849.
- Zuurbier, C. J. and Huijing, P. A.** (1992). Influence of muscle geometry on shortening speed of fibre, aponeurosis and muscle. *J. Biomech.*, **25**, 1017-1026.
- Zuurbier, C. J. and Huijing, P. A.** (1993). Changes in geometry of actively shortening unipennate rat gastrocnemius muscle. *J. Morph.*, **218**, 167-180.